Stabilizing Lattice Boltzmann Simulation of Flows Past Bluff Bodies by Introduction of Ehrenfests' Limiters

A Thesis submitted for the degree of
Doctor of Philosophy
at the University of Leicester

by

Tahir Saeed Khan
Department of Mathematics,
University of Leicester,
United Kingdom.

January 2011

To

my father,

Muhammad Saeed Khan

and

in memory of

my mother

(1958-2005)

Abstract

The lattice Boltzmann method (LBM) have emerged as an alternative computational approach to the conventional computational fluid dynamics (CFD). Despite being computationally efficient and popular numerical method for simulation of complex fluid flow, the LBM exhibits severe instabilities in near-grid scale hydrodynamics where sharp gradients are present. Further, since the LBM often uses uniform cartesian lattices in space, the curved boundaries are usually approximated by a series of stairs that also causes computational inaccuracy in the method. An interpolation-based treatment is introduced for the curved boundaries by Mei et al. One of the recipe to stabilize the LBM is the introduction of Ehrenfests' step. The objective of this work is to investigate the efficiency of the LBM with Ehrenfests' steps for the flows around curved bluff bodies. For this purpose, we have combined the curved boundary treatment of Mei et al. and the LBM with Ehrenfests' steps and developed an efficient numerical scheme. To test the validity of our numerical scheme we have simulated the two-dimensional flow around a circular cylinder and an airfoil for a wide range of low to high Reynolds numbers ($Re \leq 30,000$). We will show that the LBM with Ehrenfests' steps can quantitatively capture the Strouhal-Reynolds number relationship and the drag coefficient without any need for explicit sub-grid scale modeling. Comparisons with the experimental and numerical results show that this model is a good candidate for the turbulence modeling of fluids around bluff bodies.

Acknoledgements

All praise is for Allah Who is the most merciful, Knowledgeable and Worthy of all praises. He Knowth what before or after or behind us. And may His blessings, peace and favours descend in perpetuity on our beloved Prophet Muhammad al-Mustafa, Sallallahu 'alaihi wa Sallam who is mercy for all the worlds.

I would like to thank my supervisor Prof. Jeremy Levesley for giving me a precious opportunity to join him and for his support, time and guidance during my PhD studies. His sincere support, approachability and valuable suggestions had been of great help to complete my studies. I also really appreciate all the help and guidance provided by Dr. Rob Brownlee which he provided me in programming. I would like to express my humble gratitude to all the people in the Department of Mathematics who helped me at some point during my work and whose company has been a great source of happiness, amusement and enlightenment. It is a pleasure to thank my friends from Pakistan whose company and support made my life at Leicester full of enjoyment and fulfilment. Words are lacking to express my gratefulness to my parents, brothers and sisters for their love, support and prayers which has been and will be a source of happiness and accomplishment. I am also thankful to the University of Peshawar and Higher Education Commission of Pakistan for providing financial support to perceive my PhD studies.

Table of Contents

Nomenclature

Roman symbols

A_{ij}	the collision matrix
$\mathbf{e}_i$	discrete velocity of a particle along ith lattice direction
c	lattice velocity
c_s	speed of sound
C_D	drag coefficient
C_L	lift coefficient
D	diameter of the cylinder
E	macroscopic energy density
f	particle distribution function
f_i	particle distribution function along ith lattice direction
$\tilde{f}_i$	post-collision particle distribution function
$f^{(eq)}$	particle equilibrium distribution function
f^*	fictitious equilibrium distribution function
$f_i^{(eq)}$	particle equilibrium distribution function along ith lattice direction
f_s	vortex shedding frequency
F_x	drag force

F_y	lift force
k	number of lattice sites for Ehrenfests' steps
K	body force acting on each particle
L	characteristic length
m	linear transformation from microscopic to macroscopic description
M	macroscopic moments vector
n_i	the occupational number of a particle along ith lattice direction
n_r	reference density
N	total number of lattice sites
p	fluid pressure
P	kinematic pressure of fluid
P^*	non-dimensional pressure
$Q(f,f)$	collision integral describing interaction between the particles
R	Boltzmann constant
Re	Reynolds number
St	Strouhal number
$S(f)$	microscopic entropy
$S(f^{(eq)})$	macroscopic entropy
t_c	collision time
T	macroscopic temperature
$\mathbf{u}$	macroscopic fluid velocity
$\mathbf{u}^*$	non-dimensional fluid velocity
$\mathbf{u}_w$	wall velocity
$\mathbf{u}_f$	macroscopic velocity at fluid nodes
$\mathbf{u}_{sf}$	fictitious fluid velocity at physical boundary

U	upstream flow velocity
U_∞	inlet fluid velocity in a channel flow around bluff bodies
$\mathbf{v}$	microscopic fluid velocity
w_i	weight function of the quadrature

Greek symbols

$\delta\mathbf{x}, \delta t$	lattice space step size and lattice time step respectively
δ	tolerance value for entropy deviation
∇	spacial differential operator
∇^*	non-dimensional spacial differential operator
ν	kinematic viscosity of fluid
ρ	fluid density
Δ_i	the collision operator representing rate of change of particle collisions
$\triangle$	fraction of the intersected link of physical boundary in the fluid region
Ω_i	the local averaged collision operator representing rate of change of distribution functions
ω	relaxation frequency towards local equilibrium
τ	relaxation time towards local equilibrium
ϵ	Knudson number
ε	coarse-graining time
$\xi(\mathbf{v})$	polynomial of $\mathbf{v}$
χ	weighting factor for the curved boundary link
Ψ_M	macroscopic field

Φ_ε	phase flow transformation
Θ_ε	phase flow transformation of the conservative dynamics

List of Figures

Chapter 1

Introduction

1.1 Motivations

Flow around bluff bodies occurs in numerous fields of science and engineering. Examples of these are flows past vehicles, cables, towers, bridge-deck sections etc. These flows have been studied both experimentally and numerically for the last several decades. With the advent of computer technology, computational fluid dynamics (CFD) has emerged as an advantageous numerical approach over the experimental approach which is more expensive in many situations. In one variant of CFD known as macro-fluid dynamics, various numerical algorithms are developed to solve the Navier-Stokes equations. The molecular dynamics (MD) is another variant of CFD in which the individual motion of fluid molecules are simulated on a computer. Then once their inter-molecular interactions have been summed and averaged, the system behaves as a fluid.

During last two decades the lattice Boltzmann method (LBM) [83, 92] has emerged as an alternative and efficient numerical algorithm for the modeling and simulation

of fluid dynamics problems. Unlike the traditional CFD tools (finite difference, finite volume, finite elements and spectral methods) which are based on the discretization of continuous partial differential equations (Navier-Stokes equations for fluid dynamics), the LBM is based on evolution equations for the mesoscopic Boltzmann densities. The basic philosophy of the LBM is the construction of such simplified kinetic models which incorporate the essential physical properties of the microscopic processes so that macroscopic quantities can be calculated from the averaged mesoscopic densities. Among the different variants of the LBM in use, are the multiple relaxation lattice Boltzmann method, the finite volume lattice Boltzmann method, the interpolation-supplemented lattice Boltzmann method, the entropic lattice Boltzmann method [6, 47, 49, 50, 85] and the recently introduced lattice Boltzmann method with Ehrenfests' step [17, 18, 19, 20].

The main advantages of the LBM are:

- Because of its explicit nature of governing equations, this model is optimally suited for vectorization and parallelization which results into short and fast numerical codes;

- Particle interpretation of this method allows very simple boundary conditions for complex flow geometries;

- Linearity of the streaming operator and locality of the non-linear collision operations help making the access of contiguous memory much faster. It means that memory can be deallocated after each time step and it is available for the next iteration.

1.2 Background to Present Study

Despite successful LBM simulations of various fluid flows of engineering interests, it has been observed that the LBM exhibits both linear and non-linear numerical instabilities in low viscosity regimes, for example in case of high Reynolds number flows. Linear stability analysis might be sufficient where hydrodynamic gradients are weak but non-linear stability analysis is needed in the near-grid scale hydrodynamics where large gradients are present. The reasons for these instabilities are lack of positivity and deviations of the probability distribution functions from the quasi-equilibrium states.

Sterling and Chen [81] were amongst the first who investigated the stability problem in the LBM. In their work, the lattice Bhatnagar-Gross-Krook (LBGK) collision operator was linearized for the fluctuating quantities of the particle distribution functions with respect to the equilibrium distribution functions and then the most unstable directions and wave numbers, and their relationship with the mean flow field, relaxation time and mass distribution parameters were identified through the Von Neumann stability analysis. Worthing et. al [93] extended this analysis to non-uniform flows and found some stability boundaries particularly in case of a shear background flow.

D'Humieres [26] proposed the multiple-relaxation-time (MRT) LBE method which has also shown improvement in the stability of LBM [55, 64]. The MRT model attempts to relax different particle distribution functions to the equilibrium state with different relaxation times.

The standard LBM faces severe non-linear instabilities in the near-grid scale dynamics which arise mostly due to the violation of the second law of thermodynamics. The stability of the LBM has been improved in entropic lattice Boltzmann method

(ELBM) [2, 3, 4, 5, 13, 48] through compliance with the H-theorem [84] which ensures the positive entropy production of the distribution function. Although the ELBM is more stable than the LBGK method and allows high Reynolds number flow simulation [2], yet it suffers from spurious oscillations in regions with strong hydrodynamic gradients, such as in the vicinity of shocks [13]. However, a great reduction of the spurious oscillations in the ELBM has been achieved by constructing complete Galilean invariance models [21].

Lie et. al [56] proposed a FIX-UP method which has shown improvement on the stability by enforcing non-negativity of the particle distribution function. A good stability analysis on the comparison of the FIX-UP and the ELBM methods has been carried out by Tosi et. al [86]. The FIX-UP method has computational cost half the computational cost of the ELBM in one single time step. But the ELBM is more stable than the FIX-UP method for high Reynolds number flows.

Brownlee et. al [17] introduced an alternative and versatile approach, the LBM with Ehrenfests' steps. The deviation of the populations from the quasi-equilibrium states has been controlled by first fixing a tolerance value for the difference in microscopic and macroscopic entropy and when this tolerance value is exceeded the populations are returned to their quasi-equilibrium states. Following this idea some non-equilibrium entropy limiters [19] were constructed for the LBM which help erase spurious oscillations in the sharp gradient regions and stabilize the LBM simulation.

The LBM often uses uniform regular cartesian lattices in space, so curved boundaries are often approximated by a series of stairs that leads to reduction in computational accuracy. On the curved body geometries, the interpolation-based schemes play an important role to improve the numerical stability of the LBM [28, 51, 66, 96].

Mei et al. [66, 68] made an improvement in the Fillipova Hännel boundary treatment [28] and proposed a second-order accurate boundary condition treatment for the lattice Boltzmann equation.

1.3 Aims and objectives

Both models the ELBM and the LBM with Ehrenfests' steps have efficiently simulated turbulent flow past a square cylinder for high Reynolds numbers [6, 19]. In the present study, we have constructed a numerical scheme for the stable simulation of flows past curved bluff bodies by taking the curved boundary treatment of Mei et al. [66] and applying the Ehrenfests' steps after collision in the LBM proposed by Brownlee [17].

The main goal of this work is to investigate the laminar and turbulent unsteady flow fields around the bluff bodies of curved cross-sections for various Reynolds numbers. To achieve the aims of this research, the following three objectives are set:

- Investigation of the two-dimensional vortex shedding phenomenon in a circular cylinder wake for Reynolds numbers up to $Re = 20,000$. Global flow parameters such as Strouhal numbers, drag and lift coefficients are computed for the verification and validation. Numerical results presented here, are compared with other experimental and numerical results [39, 40, 71, 72, 75, 77, 78, 79, 91, 97]. For the validation of turbulent simulation of the flow around a circular cylinder, the Reynolds number selected is $Re = 3,900$ due to the availability of numerical and experimental data at this number.

- Simulation of the flow around elliptical cylinders of different aspect ratios for different Reynolds numbers. This work aims to investigate the changes of the shedding frequency, drag and lift coefficients with the increase of aspect ratio.

- Simulation of the flow around a NASA 0015 airfoil for high Reynolds number. The study includes the simulation of vortex shedding phenomenon, and drag and lift coefficients of the flow.

1.4 Thesis Structure

This chapter discusses the aims, the objectives and the methodology of the research work. The main content of the thesis are introduced in the following chapters.

Chapter Two contains an introduction to the lattice Boltzmann model. First a historical background of the method is given which starts from its ancestor, named the lattice gas cellular automata (LGCA). Then by introducing the lattice Bhatnagar-Gross-krook (BGK) approximation to the collision integral in the lattice Boltzmann equation, the lattice Bhatnagar-Gross-Krook (LBGK) scheme is obtained. Our focus would be on the two-dimensional BGK lattice Boltzmann model and on the numerical instabilities faced by it. At the end of Chapter Two, different boundary conditions for the lattice Boltzmann method are discussed. Specifically, the curved boundary treatment proposed by O. Filippova and D. H*ä*nel [28] and improved by R. Mei, L.S. Luo and W. Shyy [66] is presented.

Chapter Three discusses the idea of Ehrenfests' coarse-graining introduced by A. Gorban [34] and then explains how the second order Navier -Stokes equations are recovered from the Boltzmann equation in the Ehrenfests' chain. In this chapter we give the construction of the Ehrenfests' entropy limiter proposed by R. Brownlee, A. N. Gorban and J. Levesley [17, 18, 19, 20]. Thus a numerical scheme is evolved which stabilizes the LBGK model.

In Chapter Four the flow around a circular cylinder is selected as a first validation

example for the numerical scheme described in chapter three. This flow simulation is stabilized for high Reynolds numbers and flow characteristics like Strouhal number, drag and lift coefficients are compared with the previous experimental and numerical data. The chapter then focuses on the detailed comparisons of the velocity profiles and Reynolds stress components at various locations in the wake region of the flow with experimental data at a Reynolds number of $Re = 3900$.

In Chapter Five we discuss the verification and validation of our turbulence models for the flow around elliptic cylinders of different aspect ratios at various Reynolds number. Similar to the flow around a circular cylinder, current validation involves direct comparison of the Strouhal number, drag and lift coefficients of the flow with experimental findings. As a third example we perform the simulation of the flow around the NASA0015 airfoil. These simulations focusses on the changes of the drag and lift coefficients for different Reynolds number.

Chapter Six draws conclusions on the work done on the research. This focuses on the objectives of the work and how they are achieved throughout the thesis. The second part of the chapter seven provides suggestions and recommendations on further work for the simulation of the flow around bluff bodies. The references in the chapters are then listed following chapter seven. In the thesis, the figures are shown at the end of each chapter.

The following paper has been published during the work:

- T.S. Khan and J. Levesley, Stabilizing lattice Boltzmann simulation of fluid flow past a circular cylinder with Ehrenfests limiter, Approximation Algorithms for Complex Systems 3(2), 2011, $227 - 239$.

Chapter 2

Lattice Boltzmann Method

This chapter introduces the background theories of the lattice Boltzmann method (LBM) and it's evolution to become an alternative and promising numerical scheme for the simulation of fluid flows.

There are at least two approaches to derive the lattice Boltzmann equation (LBE), either historically from the lattice gas cellular automata (LGCA) [32] which is based on the discrete particle kinetics using a discrete lattice and discrete time or directly from a special discretized form of the Boltzmann kinettic equation [42]. In this chapter, we present an overview of the different stages of development of the LBM.

2.1 Basic theoretical concepts

In this section, definitions of some basic theoretical concepts are recalled.

2.1.1 The Navier-Stokes Equations

The *Navier-Stokes* equations for an incompressible fluid flow [1, 29] in the absence of external forces can be written as:

Momentum:

$$\frac{\partial \mathbf{u}}{\partial t} + (\mathbf{u} \cdot \nabla)\,\mathbf{u} = -\nabla P + \nu\,\nabla^2 \mathbf{u}, \tag{2.1.1}$$

Continuity:

$$\nabla \cdot \mathbf{u} = 0, \tag{2.1.2}$$

where ∇ is the nabla operator, $\mathbf{u}$ is the fluid velocity, $P = p/\rho$ the kinematic pressure, p the pressure, ρ the constant density and ν the kinematic viscosity of the fluid.

These are the nonlinear partial differential equations and except for a few cases their analytical solutions are very hard to find. Numerical methods are required to simulate the time evolution of the flows. The most important nonlinear advection term $(\mathbf{u} \cdot \nabla)\,\mathbf{u}$ is responsible for many physical processes like von Karman vortex streets or turbulence.

2.1.2 The importance of Reynolds number

Flows with small velocities are smooth and are called *laminar*. At very high velocities they become *turbulent*. From the following discussion we shall find that the transition from laminar to turbulence does not depend only on the velocity.

Consider the fluid past an obstacle(such as a sphere, a cylinder or a plate) with

upstream speed U. If L is the linear size (for example the diameter in case of a cylinder or a sphere) of the obstacle then the three parameters, U, L and ν having dimensions $[length\ time^{-1}]$, $[length]$ and $[length^2\ time^{-1}]$ respectively, form a dimensionless number, namely, the *Reynolds number*

$$Re = \frac{UL}{\nu}. \tag{2.1.3}$$

Introducing the following non-dimensional quantities:

$\mathbf{u}^* = \mathbf{u}/U$, $\mathbf{x}^* = \mathbf{x}/L$, $\nabla^* = L.\nabla^*$, $\nabla^{*2} = L^2.\nabla^{*2}$, $t^* = t.U/L$, $P^* = P/U^2$,

the above Navier-Stokes equations in non-dimensional form become:

Momentum:

$$\frac{\partial \mathbf{u}^*}{\partial t^*} + (\mathbf{u}^* \cdot \nabla^*)\,\mathbf{u}^* = -\nabla^* P^* + \frac{1}{Re}\,\nabla^{*2}\mathbf{u}^*, \tag{2.1.4}$$

Continuity:

$$\nabla^* \cdot \mathbf{u}^* = 0. \tag{2.1.5}$$

The non-dimensional Navier-Stokes equations (2.1.4) and (2.1.5) do not contain any scale and there is only one dimensionless quantity, namely, the Reynolds number. Thus for a given type of flow (say,the flow past a circular cylinder) the scaled velocity of a stationary flow will depend only on the scaled spatial coordinate and the Reynolds number. The value of the Reynolds number provides an estimate of the relative importance of the non-viscous and viscous forces. Thus flows can be characterized by the relative magnitudes of advection and viscous forces:

$$\frac{\mid (\mathbf{u} \cdot \nabla)\,\mathbf{u} \mid}{\mid \nu\,\nabla^2 \mathbf{u} \mid} \approx \frac{U^2/L}{\nu\,U/L^2} = \frac{UL}{\nu} = Re. \tag{2.1.6}$$

It has been observed that flows with small Reynolds numbers ($Re \ll 1$) are laminar, Von Karman streets are seen at intermediate values ($Re \approx 100$) and turbulent

flows occur at very high Reynolds numbers ($Re \gg 100$).

2.1.3 Law of dynamic similarity as a link between real flows and LGCA/LBM models

We can write

$$\mathbf{u}^* = \frac{\mathbf{u}}{U} = f_{\mathbf{u}}\left(\frac{\mathbf{x}}{L}, Re\right), \tag{2.1.7}$$

and

$$P^* = \frac{P}{U^2} = f_P\left(\frac{\mathbf{x}}{L}, Re\right), \tag{2.1.8}$$

where the functions $f_{\mathbf{u}}$ and f_P depend on the geometry of the flow. Thus all flows of the same type but with different values of U, L and ν are described by the one and the same nondimensional solution $(\mathbf{u}^*, P^*)$ if their Reynolds numbers are equal. All such flows are said to be *dynamically similar*.

The law of dynamic similarity provides the link between the real world flows where the length is measured in meters and the simulations of these flows with **LGCA** and **LBM** models over a lattice with unit grid length and unit lattice speed. In these models the viscosity is a dimensionless quantity because it is expressed in units of grid length and lattice speed. These dimensionless flows are similar to real flows on the lattice when their Reynolds numbers are equal.

2.1.4 The Boltzmann equation

The Boltzmann equation is an integro-differential equation for the single particle distribution function $f = f(\mathbf{x}, \mathbf{v}, t)$. The function $f(\mathbf{x}, \mathbf{v}, t)$ is defined as the probability of finding a particle moving with velocity $\mathbf{v}$ at the site $\mathbf{x}$ and at the time t, focussing

on two main processes, streaming and collision. This equation is defined as:

$$\frac{\partial f}{\partial t} + \mathbf{v} \cdot \nabla_{\mathbf{x}} f + \frac{\mathbf{K}}{m} \cdot \nabla_{\mathbf{v}} f = Q(f, f), \tag{2.1.9}$$

where

- $\mathbf{K}$ is the body force acting on each particle ;
- $\nabla_{\mathbf{x}} = (\frac{\partial}{\partial x}, \frac{\partial}{\partial y}, \frac{\partial}{\partial z})$;
- $\nabla_{\mathbf{v}} = (\frac{\partial}{\partial v_x}, \frac{\partial}{\partial v_y}, \frac{\partial}{\partial v_z})$;
- $Q(f, f)$ is the collision integral describing the interactions between the particles.

2.2 Historical developement of the LBM

Historically, the LBM was first based on the LGCA, where the fluid was modeled as an ensemble of many particles interacting locally at the nodes of a regular lattice by collisions, and obeying the hydrodynamic conservation laws. The first such discrete velocity model introduced by Hardy, de Pazzis and Pomeau [36] was the HPP model (named after their initials), where space and time were discretized on a square lattice. The HPP does not possess sufficient symmetry in order to ensure isotropy of a certain tensor of fourth rank formed from the lattice velocities and therefore the mean values do not obey the Navier-Stokes equations. After ten years of the HPP model, Frisch, Hasslacher and Pomeau [32] proposed the FHP model (again named after their initials) for two dimensional hydrodynamics, where the hexagonal symmetry of the lattice was found sufficient to recover the Navier-Stokes equations. For three dimensional hydrodynamics, d'Humières, Lallemand and Frisch [25] introduced the face-centered hyper-cube (FCHC) as a lattice with sufficient symmetry.

The LGCA were found to be insufficient for the fluid simulation of the Navier-Stokes equations. In fact, these models are plagued by several diseases [83, 92], for example, one of the major disadvantage is the statistical noise in the computed hydrodynamic simulations. To overcome this problem, McNamara and Zanetti [65] introduced the LBM by replacing the boolean operations with the continuous density distributions over the FHP and FCHC lattices. Another fault with the LGCA was the exponential complexity of the collision operator which leads to a huge amount of computational cost. By making the assumption that the particle distribution is close to the local equilibrium state, Higuera and Jiménez [44, 46] introduced the linearized collision operators. A further important development in the LBM was the approximation of the collision operator with the Bhatnagar-Gross-Krook [11] relaxation term. This single-time-relaxation (SRT) model known as lattice Bhatnagar-Gross-Krook (LBGK) model was proposed independently by Koelman [53], Qian [76] and others. These LBGK models have cured almost all the diseases faced by the earlier LGCA models and have become simple and efficient tools for hydrodynamic simulation problems.

2.3 Three ways to the Lattice Boltzmann Method

There are three different approaches [83] adopted by the researchers from the disciplines of Mathematics, Physics and Engineering respectively, for the lattice Boltzmann simulation of hydrodynamics.

2.3.1 Mathematics Approach

Mathematicians are always interested in solving partial differential equations by a numerical method. Usually, a partial differential equation is discretized and its solution is obtained on by a numerical scheme, such as finite difference, finite volume , finite element methods. Therefore, the approach adopted by the mathematicians would be in the following sequence

Boltzmann $\rightarrow$ **LBE** $\rightarrow$ *Navier-Stokes*

2.3.2 Physics Approach

Physicist are concerned about certain physical properties of the problem, so they have adopted the following approach to the LBM

Newton $\rightarrow$*Lattice-Gas* $\rightarrow$**LBE** $\rightarrow$ *Navier-Stokes*

2.3.3 Engineering Approach

Engineers like to use the Navier-Stokes solver for fluid simulation. They see the lattice Boltzmann equation as a Navier-Stokes solver. Their approach would be

Navier-Stokes $\rightarrow$ **LBE**

2.4 The lattice Boltzmann equations

The lattice Boltzmann equation (LBE) can be obtained either from the models of the lattice gas cellular automata (LGCA) or it can be directly derived from the continuous

Boltzmann equation. In this section we present an overview of these two approaches.

2.4.1 LBE as an extension of the LGCA

The evolution equation of the LGCA are described by the following kinetic equations:

$$n_i(\mathbf{x} + \mathbf{e}_i, t + 1) = n_i(\mathbf{x}, t) + \Delta_i(n(\mathbf{x}, t)), \tag{2.4.1}$$

where $n_i(\mathbf{x}, t)$ is the occupational number of a particle entering site $\mathbf{x}$ at time t with a velocity $\mathbf{e}_i$ along i lattice direction, Δ_i is the collision operator. The occupational number n_i is a boolean variable and can assume only two values 1 or 0 according to the presence or absence respectively, of a particle at site $\mathbf{x}$ at time t.

In order to get rid of the statistical noise in the LGCA, McNamara and Zanetti [65] replaced the boolean occupation numbers, n_i in equations (2.9) with the single particle velocity distribution function:

$$f_i = \langle n_i \rangle, \tag{2.4.2}$$

where $\langle . \rangle$ denotes an ensemble average. The individual particle motion and the particles correlations were neglected in the kinetic equations. In this way the statistical noise was eliminated in the LGCA. The discrete kinetic equations for the particle velocity distribution function become:

$$f_i(\mathbf{x} + \mathbf{e}_i \delta t, t + \delta t) = f_i(\mathbf{x}, t) + \Omega_i(f(\mathbf{x}, t)), \tag{2.4.3}$$

where $\Omega_i(f(\mathbf{x}, t)$ is the local averaged collision operator representing the rate of change of the distribution functions f_i resulting from the collision, defined as

$$\Omega_i(f(\mathbf{x}, t) = \langle \Delta_i(n(\mathbf{x}, t)) \rangle. \tag{2.4.4}$$

The macroscopic variables can be obtained from the averaged particle velocity distribution functions. The macroscopic density is defined as:

$$\rho = \sum_i f_i. \tag{2.4.5}$$

The macroscopic momentum density is defined as:

$$\rho \mathbf{u} = \sum_i f_i \mathbf{e}_i. \tag{2.4.6}$$

Further, the collision operators Ω_i must satisfy the following conservation equations:

$$\sum_i \Omega_i = 0, \tag{2.4.7}$$

and

$$\sum_i \Omega_j \mathbf{e}_i = 0. \tag{2.4.8}$$

To make the LBM practically viable for the three dimensional hydrodynamic simulations, Higuera and Jiménez [45] proposed the quasi linear collision operator:

$$\Omega_j(f) = A_{ij}(f_i - f_i^{eq}), \tag{2.4.9}$$

where A_{ij} is the collision matrix, which determines the scattering rate between directions i and j and it depends only on the angles between the directions i and j. It is a cyclic, symmetric and negative-definite matrix. The symmetry of the scattering matrix implies that it satisfies the following mass and momentum conservation collisions constraints [10]:

$$\sum_i A_{ij} = 0, \qquad \sum_i \mathbf{e}_i A_{ij} = 0. \tag{2.4.10}$$

The negative-definiteness property of the scattering matrix ensures the fulfilment of the second principle of thermodynamics through compliance with H-theorem. From

the properties mentioned above, the scattering matrix can be reconstructed once the eigenvalues and corresponding eigenvectors are known.

The discrete scattering version of the collision operator, defined in Equation (2.4.9), has minimized the complexity of the LBE collision process. The eigenvalues of the scattering matrix A_{ij} are associated with the slow non-conserved quantities like the momentum flux tensor [83]. The viscosity of the fluid is associated and controlled by a unique eigenvalue of the scattering matrix. The remaining eigenvalues are then set such that the interference of the non-hydrodynamic modes with the dynamics of macroscopic variables can be minimized. This observation [53, 76] leads to the idea of the simplification of the scattering matrix as a diagonal scattering matrix with the unique eigenvalue ω, on the diagonal, which controls the viscosity. The scattering matrix is replaced by the following diagonal form:

$$A_{ij} \to -\omega\delta_{ij}, \tag{2.4.11}$$

where the eigenvalue $\omega > 0$, is the relaxation frequency towards the local equilibrium. The inverse of ω is the relaxation time $\tau = 1/\omega$.

It means a multi-relaxation scheme has been changed to a single-time relaxation scheme. This new scheme is known as the lattice Bhatnagar-Gross-Krook (LBGK) model because of its direct link with the famous BGK method [11]. The BGK approximation of the collision operator becomes:

$$\Omega_i(f) = -\omega(f_i - f_i^{(eq)}). \tag{2.4.12}$$

The introduction of the above BGK approximation in equation (2.11) leads to the following complete LBGK equation:

$$f_i(\mathbf{x} + \mathbf{e}_i\delta t, t + \delta t) = f_i(\mathbf{x}, t) - \omega(f_i - f_i^{(eq)}). \tag{2.4.13}$$

2.4.2 From the Boltzmann equation to the LBE

In the absence of the body force, the Boltzmann equation (2.1.9) defined in Section 2.1 becomes:

$$\frac{\partial f}{\partial t} + \mathbf{v} \cdot \nabla f = Q(f), \tag{2.4.14}$$

where on the right hand side, Q is the local collision integral describing the interactions of the populations f.

Equation (2.23) is a kinetic transport equation describing the microdynamics of the model. The macroscopic variables, the fluid density, momentum density and energy density are the following moments of the distribution function f:

$$\rho(\mathbf{x}, t) = \int f(\mathbf{x}, \mathbf{v}, t) d\mathbf{v}, \tag{2.4.15}$$

$$\rho\mathbf{u}(\mathbf{x}, t) = \int \mathbf{v} f(\mathbf{x}, \mathbf{v}, t) d\mathbf{v}, \tag{2.4.16}$$

and

$$E(\mathbf{x}, t) = \frac{1}{2}\rho DT + \frac{1}{2}\rho\mathbf{u}^2 = \frac{1}{2}\int \mathbf{v}^2 f(\mathbf{x}, \mathbf{v}, t) d\mathbf{v}, \tag{2.4.17}$$

where D is the dimension of the space and T is the macroscopic temperature.

The Bhatnagar-Gross-Krook [11] or single-time-relaxation approximation of the collision operator Q is:

$$Q(f) = -\frac{1}{\tau}(f - f^{(eq)}), \tag{2.4.18}$$

where τ is the relaxation time after which the populations f relax towards the equilibrium values $f^{(eq)}$. It has been shown through Chapman-Enskog expansion [84] that the resulting macrodynamics are the Navier-Stokes equations to second-order in τ. The $f^{(eq)}$ is the Maxwell-Boltzmann equilibrium distribution function:

$$f_i^{(eq)} = \frac{\rho}{(2\pi RT)^{D/2}} \exp(-\frac{(\mathbf{v} - \mathbf{u})^2}{2RT}), \tag{2.4.19}$$

where R is the ideal gas constant (Boltzmann constant).

With this BGK approximation the Boltzmann equation becomes:

$$\frac{\partial f}{\partial t} + \mathbf{v} \cdot \nabla f = -\frac{1}{\tau}(f - f^{(eq)}). \tag{2.4.20}$$

Sterling and Chen [81] derived the LBE as a special discretization of the Boltzmann equation by making the following assumptions:

- The particle populations f can only move with a finite number of discrete velocities $\mathbf{e}_i$. The corresponding populations are denoted by f_i .

- A collision operator with a single relaxation time, τ, is used to redistribute populations f_i towards equilibrium values $f_i^{(eq)}$. This is also referred to as a BGK collision operator where τ is inversely proportional to density. For constant density flows τ is a constant.

- The equilibrium velocity distribution function is written as a truncated power series in the macroscopic flow velocity.

The discrete velocity Boltzmann equation then becomes:

$$\frac{\partial f_i}{\partial t} + \mathbf{e}_i \cdot \nabla f_i = -\frac{1}{\tau}(f_i - f_i^{(eq)}). \tag{2.4.21}$$

Equation (2.4.21) can be written in non-dimensional form by using the characteristic flow length scale L, the reference speed U, the reference density n_r and two reference time scales, t_c to represent the time between particle collisions and L/U to represent a characteristic flow time. The reference speed may be selected to be the magnitude of the minimum nonzero discrete velocity. If only one speed is used, then the velocity set for the non-dimensional equations is simply a set of unit vectors. The resulting non-dimensional equation is

$$\frac{\partial \hat{f}_i}{\partial \hat{t}} + \hat{\mathbf{e}}_i \cdot \hat{\nabla} \hat{f}_i = -\frac{1}{\epsilon \hat{\tau}} (\hat{f}_i - \hat{f}_i^{(eq)}), \tag{2.4.22}$$

where the caret symbol is used to denote non-dimensional quantities $\hat{\mathbf{e}}_i = \mathbf{e}_i/U$, $\hat{\nabla} = L\nabla$, $\hat{t} = tU/L$, $\hat{\tau} = \tau/t_c$ and $\hat{f}_i = f_i/n_r$. The parameter $\epsilon = t_c \frac{U}{L}$ and may be interpreted as either the ratio of collision time to flow time or as the ratio of mean free path to the characteristic flow length (i.e., Knudsen number). A discretization of Equation (2.4.22) in two dimensional space and time results in the equation:

$$\begin{aligned} &\frac{\hat{f}_i(\hat{\mathbf{x}}, \hat{t} + \delta\hat{t}) - \hat{f}_i(\hat{\mathbf{x}}, \hat{t})}{\delta\hat{t}} + e_{ix} \frac{\hat{f}_i(\hat{\mathbf{x}} + \delta\hat{x}, \hat{t} + \delta\hat{t}) - \hat{f}_i(\hat{\mathbf{x}}, \hat{t} + \delta\hat{t})}{\delta\hat{x}} \\ &+ e_{iy} \frac{\hat{f}_i(\hat{\mathbf{x}} + \delta\hat{y}, \hat{t} + \delta\hat{t}) - \hat{f}_i(\hat{\mathbf{x}}, \hat{t} + \delta\hat{t})}{\delta\hat{y}} \\ &= -\frac{1}{\epsilon\hat{\tau}} (\hat{f}_i - \hat{f}_i^{(eq)}), \end{aligned} \tag{2.4.23}$$

where $\mathbf{e}_i = (e_{ix}, e_{iy})$ and $\delta\hat{t} = \delta t.U/L$. A particular discretization of the non-dimensional discrete Boltzmann equation (2.4.23) would be made by choosing the lattice Boltzmann method which is an exact Lagrangian solution for the convective derivatives. For a given convection velocity, this type of scheme is typically obtained by using an Euler time step in conjunction with an upwind spatial discretization and then setting the grid spacing divided by the time step equal to the lattice velocity *i.e.*, $\delta\hat{\mathbf{x}}/\delta\hat{t} = \mathbf{e}_i$:

$$\begin{aligned} &\frac{\hat{f}_i(\hat{\mathbf{x}}, \hat{t} + \delta\hat{t}) - \hat{f}_i(\hat{\mathbf{x}}, \hat{t})}{\delta\hat{t}} + \frac{\hat{f}_i(\hat{\mathbf{x}} + \mathbf{e}_i\delta\hat{t}, \hat{t} + \delta\hat{t}) - \hat{f}_i(\hat{\mathbf{x}}, \hat{t} + \delta\hat{t})}{\delta\hat{t}} \\ &= \frac{\hat{f}_i(\hat{\mathbf{x}} + \mathbf{e}_i\delta\hat{t}, \hat{t} + \delta\hat{t}) - \hat{f}_i(\hat{\mathbf{x}}, \hat{t})}{\delta\hat{t}} = -\frac{1}{\hat{\tau}\epsilon} (\hat{f}_i - \hat{f}_i^{(eq)}). \end{aligned} \tag{2.4.24}$$

Multiplication of the above Equation (2.4.24) by $\delta\hat{t}$, results in

$$\hat{f}_i(\hat{\mathbf{x}} + \mathbf{e}_i\delta\hat{t}, \hat{t} + \delta\hat{t}) - \hat{f}_i(\hat{\mathbf{x}}, \hat{t}) = -\frac{\delta\hat{t}}{\hat{\tau}\epsilon} (\hat{f}_i - \hat{f}_i^{(eq)})$$

Substituting back the values: $\delta\hat{t} = \delta t.U/L$ and $\epsilon = t_c\frac{U}{L}$, we have

$$\hat{f}_i(\hat{\mathbf{x}} + \mathbf{e}_i\delta\hat{t}, \hat{t} + \delta\hat{t}) - \hat{f}_i(\hat{\mathbf{x}}, \hat{t}) = -\frac{\delta t}{\hat{\tau}t_c}(\hat{f}_i - \hat{f}_i^{(eq)})$$

The next characteristic of the lattice Boltzmann method is the selection of the time step to equal the reference collision time ($\delta t = t_c$). The result is the cancelation of the Knudsen number in the denominator of the collision term. Dropping all the carets leads to the following BGK lattice Boltzmann equation (LBE):

$$f_i(\mathbf{x} + \mathbf{e}_i\delta t, t + \delta t) - f_i(\mathbf{x}, t) = -\frac{1}{\tau}(f_i(\mathbf{x}, t) - f_i^{(eq)}(\mathbf{x}, t)). \tag{2.4.25}$$

Sterling and Chen [81] interpreted this equation in these words:

" This equation has a particularly simple physical interpretation in which the collision term is evaluated locally and there is only one streaming step or shift operation per lattice velocity. This stream-and-collide particle interpretation is a result of the fully Lagrangian character of the equation for which the lattice spacing is the distance travelled by the particles during a time step. Higher order discretizations of the discrete Boltzmann equation typically require several shift operations for the evaluation of each derivative and a particle interpretation is less obvious. In fact, the entire derivation of the LB method was originally based on the idea of generalizing LG models by the LG Boltzmann equation and relaxing the exclusion principle that particle populations be either zero or one for each velocity [65]. It did not originally occur to the authors that the LB method could be considered a particular discretization for the discrete Boltzmann equation [65]."

2.4.3 Hydrodynamic moments of the LBE

In order to numerically solve the discrete LBE (2.4.25) with respect to $\mathbf{x}$ and t, the equilibrium distribution function $f_i^{(eq)}$ in the right hand side of the equation must be evaluated. This can be done once the macroscopic variables ρ, $\rho\mathbf{u}$ and E are evaluated first. For the numerical evaluation of these hydrodynamic moments defined in Equations $(2.24 - 2.26)$, the velocity space $\mathbf{v}$ must be discretized in an appropriate manner such that the mass, momentum and energy conservation laws are satisfied. Once the velocity space $\mathbf{v}$ is discretized, integration in the momentum space with weight function, $f^{(eq)}$ can be approximated by the following quadrature up to certain degree of accuracy [38]

$$\int \xi(\mathbf{v}) f^{(eq)}(\mathbf{x}, \mathbf{v}, t) d\mathbf{v} = \sum_i w_i \xi(\mathbf{e}_i) f^{(eq)}(\mathbf{x}, \mathbf{e}_i, t),$$

where $\xi(\mathbf{v})$ is a polynomial of $\mathbf{v}$, w_i is the weight function of the quadrature and $\mathbf{e}_i$ is the discrete velocity set.

This requires the following conservation constraints on the local equilibrium distribution:

$$\rho = \sum_i f_i^{(eq)} = \sum_i f_i, \tag{2.4.26}$$

$$\rho\mathbf{u} = \sum_i f_i^{(eq)} \mathbf{e}_i = \sum_i f_i \mathbf{e}_i, \tag{2.4.27}$$

$$E = \sum_i f_i^{(eq)} \mathbf{e}_i^2 = \sum_i f_i \mathbf{e}_i^2. \tag{2.4.28}$$

2.5 Two-dimensional BGK Lattice Boltzmann Model

In the present work, we shall consider the two-dimensional lattice BGK model. The lattice Boltzmann equation in two-dimension has the following three main ingredients:

- the kinetic equation: BGK lattice Boltzmann equation (2.34) with discretized time and with the velocity space $\mathbf{v}$ drastically reduced to only a few discrete points by assuming that at each site the particles can move along a finite number of directions, described by discrete speeds $\mathbf{e}_i$.

- an appropriate equilibrium distribution functions $f_i^{(eq)}$: the Boltzmann-Maxwellian distribution function defined in equation (2.28).

- the lattice: D2Q9 lattice, a two-dimensional nine-velocity lattice which exhibits rotational symmetry to ensure the conservation constraints, as shown in Figure (2.1).

The discrete velocities for D2Q9 lattice are defined as:

$$\mathbf{e}_i = \begin{cases} (0,0), & i = 0, \\ (c\cos[(i-1)\pi/2], c\sin[(i-1)\pi/2]), & i = 1,2,3,4, \\ (\sqrt{2}c\cos[(i-5)\pi/2+\pi/4], \sqrt{2}c\sin[(i-5)\pi/2+\pi/4]), & i = 5,6,7,8. \end{cases} \tag{2.5.1}$$

where $c = \delta x/\delta t$, δx and δt are lattice constant and the time step size, respectively.

In order to recover the macroscopic fluid dynamic equations (the Navier-Stokes equations) from the LBE (2.34), the local equilibrium distribution function must be carefully chosen. The explicit expression of the local equilibrium distribution function [5] has the following form:

$$f_i^{(eq)} = w_i\rho\prod_{j=1}^{2}(2-\sqrt{1+3u_j^2})\left(\frac{2u_j+\sqrt{1+3u_j^2}}{1-u_j}\right)^{e_{i,j}/c}, \tag{2.5.2}$$

where j is the index of the spatial directions, so $e_{i,j}$ represents the jth component of $\mathbf{e}_i$, and w_i are the weighting factors defined below. The second order expansion gives

the following polynomial quasi-equilibria [42]:

$$f_i^{eq} = w_i \rho \left[1 + \frac{3}{c^2}(\mathbf{e}_i \cdot \mathbf{u}) + \frac{9}{2c^2}(\mathbf{e}_i \cdot \mathbf{u})^2 - \frac{3}{2c^2}(\mathbf{u} \cdot \mathbf{u}) \right], \tag{2.5.3}$$

where the weights w_i are given by:

$$w_i = \begin{cases} \frac{4}{9}, & i = 0 \\ \frac{1}{9}, & i = 1, 2, 3, 4 \\ \frac{1}{36}, & i = 5, 6, 7, 8. \end{cases} \tag{2.5.4}$$

The pressure can be calculated through the ideal gas equation of state:

$$P = c_s^2 \ \rho, \tag{2.5.5}$$

where c_s is the lattice sound speed, which depends on the discrete velocity set. It's value for D2Q9 model is $c_s = c/\sqrt{3}$.

The kinematic viscosity is related to the relaxation time τ by:

$$\nu = c_s^2(\tau - \frac{1}{2}). \tag{2.5.6}$$

For the viscosity to be positive, we must have $\tau > \frac{1}{2}$.

The two computational steps for the LBM are:

$$\textit{Collision}: \qquad \tilde{f}_i(\mathbf{x}, t) = f_i(\mathbf{x}, t) - \frac{1}{\tau}[f_i(\mathbf{x}, t) - f_i^{eq}(\mathbf{x}, t)], \tag{2.5.7}$$

$$\textit{Streaming}: \qquad f_i(\mathbf{x} + \mathbf{e}_i \delta t, t + \delta t) = \tilde{f}_i(\mathbf{x}, t), \tag{2.5.8}$$

where f_i and $\tilde{f}_i$ denote the pre-collision and post-collision distribution functions, respectively.

2.6 Lattice Boltzmann Methods versus Conventional CFD

As an alternative numerical method, the LBM differs from the conventional Navier-Stokes solvers in a number of different aspects. The main differences are shown in the following comparisons:

- In the conventional CFD methods, the fluid equations constructed are the second-order partial differential equations PDEs (Navier-Stokes equations). These PDEs are discretized by finite differences, finite volumes, finite elements or spectral methods. The resulting algebraic equations or system of ordinary differential equations are then solved on a given mesh by applying PDE boundary conditions through standard numerical methods. Although this 'top-down' approach [84] seems to be straightforward, it is not without difficulties. As mathematicians are worried about the truncation error which occurs due to the truncation of Taylor series when going from differential equation to finite difference equations whereas the physicists are concerned whether the certain quantities are conserve in the discretized form of equations. Numerical instabilities are another type of problem of this type of numerical methods.

  In the lattice based methods (LGCA and LBM), discrete formulation of kinetic theory results in the form of Lattice Boltzmann equations (LBEs) which by construction conserved the desired quantities (mass and momentum) for the Navier-Stokes equations. Since are already in discrete form therefore no further approximations are required. These equations are then solved on lattices and kinetic boundary conditions are applied. The derivation of the corresponding

macroscopic equations requires, however, lengthy calculations (multi-scale analysis). A major problem with this 'bottom-up' approach [84] is to detect and avoid spurious invariants which is by the way, also a problem for the models derived by the 'top-down' approach.

- The Navier-Stokes Equation (2.1.1) contains a non-linear convective term $\mathbf{u} \cdot \nabla \mathbf{u}$ whereas in the LBE method, the convection operator defined in Equation (2.4.21) is linear.

- In traditional CFD methods, the Poisson equation derived from the incompressible Navier-Stokes equations, is solved explicitly to obtain the pressure making it costly in terms of time, while in the LBE approach the pressure is obtained through the equation of state (2.5.5). But LBE only has $O(1)$ speed of sound.

- Time-dependent flows simulation is costly for the CFD, while it is easy and straightforward for the LBM. But direct access to steady-state not possible with LBE method.

- For the conventional CFD, complex physics (like multi-phase flows) requires complex physical models, while for the LBM these flows involve simple models.

- Because of their non-linearity and non-locality, the Navier-Stokes equations can not be parallelized easily, whereas because of it's explicit nature, the LBE (2.4.21) is natural to be parallelized.

- Boundary conditions involving complicated geometries require careful treatments in both NS and LBE solvers. In NS solvers, normal and shear stress components require appropriate handling of geometric estimates of normal and

tangent, as well as one-sided extrapolation. In LBE solvers, the boundary condition issue arises because the continuum framework, such as the no-slip condition at the wall, does not have a counterpart.

- The spatial discretization in the LBE method is dictated by the discretization of the particle velocity space. This coupling between discretized velocity space and configuration space leads to regular square grids. This is a limitation of the LBE method, especially for aerodynamic applications where both the far field boundary condition and the near wall boundary layer need to be carefully implemented.

2.7 Boundary Conditions

For any real fluid simulation problem, the boundary conditions play an important role in the solution so they must be defined. The two types of boundaries which are mostly encountered are open and solid wall boundaries.

The open boundaries occur in many physical problems. These include lines or planes of symmetry, periodic cross-sections, fluid inlets and outlets. The solid wall boundaries include walls of a channel flow and obstacles of different shapes submerged in a fluid. These can be regular as well as irregular as shown in Figures (2.2) and (2.3). Here some main boundary conditions are briefly discussed for the LBM.

2.7.1 Periodic boundary conditions

Periodic boundary conditions [83] are the simplest boundary conditions applied to such physical processes where the surface effects play an insignificant role. For the practical implementation, for example a two-dimensional physical domain (a channel

flow), a buffer zone of two extra layers of sites $w(west)$ and $e(east)$ is created as shown in Figure (2.4). Then populations on a D2Q9 lattice are replicated as:

$$f_{1,5,8}(w) = f_{1,5,8}(e), \tag{2.7.1}$$

$$f_{3,6,7}(e) = f_{3,6,7}(w). \tag{2.7.2}$$

2.7.2 No-slip boundary conditions

No-slip boundary conditions, also known as the $bounce - back$ boundary conditions [33, 38, 98], are applied in the fluid-solid interactions where the particles are assumed to have zero velocity at the solid wall. For the practical implementation of the bounce-back boundary conditions, the solid surface is aligned with the grid, for example in case of a two-dimensional channel flow the north and south walls are aligned with the grid. There are two types of bounce back boundary conditions $on - grid$ and $mid - grid\ bounce - back$ boundary conditions.

In on-grid boundary conditions, the solid boundary is placed exactly on the grid line and the populations sitting on a boundary node are simply reversed in the opposite directions as shown in Figure (2.5). For example in case of a two-dimensional channel flow, the populations on the north and south walls can respectively be obtained as follows:

$$f_{4,7,8}(north) = f_{2,5,6}(north), \tag{2.7.3}$$

$$f_{2,5,6}(south) = f_{4,7,8}(south). \tag{2.7.4}$$

In terms of the boundary matrix, the boundary conditions on the north wall is:

$$\begin{bmatrix} f_4(x,y) \\ f_7(x,y) \\ f_8(x,y) \end{bmatrix} = \begin{bmatrix} 1 & 0 & 0 \\ 0 & 1 & 0 \\ 0 & 0 & 1 \end{bmatrix} \begin{bmatrix} f_2(x,y) \\ f_5(x,y) \\ f_6(x,y) \end{bmatrix}. \tag{2.7.5}$$

A similar matrix can be obtained for the south wall.

In mid-grid boundary conditions where the wall lies midway between two lattice sites, the population with velocity $\mathbf{e}_i.\mathbf{u}$, assume the velocity $-\mathbf{e}_i.\mathbf{u}$ after the collision at each boundary site as shown in Figure (2.6). The explicit scheme for these boundary conditions is the following 3×3 matrix [83]:

$$\begin{bmatrix} f_4(x,y) \\ f_7(x,y) \\ f_8(x,y) \end{bmatrix} = \begin{bmatrix} 1 & 0 & 0 \\ 0 & 1 & 0 \\ 0 & 0 & 1 \end{bmatrix} \begin{bmatrix} f_2(x,y-1) \\ f_5(x-1,y-1) \\ f_6(x+1,y-1) \end{bmatrix}, \tag{2.7.6}$$

where (x, y) is the generic site on the north wall. Similar boundary treatment can be done for the south wall.

It may be noted that mid-grid bounce-back boundary condition is $O(1.5)$ accurate and on-grid bounce-back boundary condition id $O(1)$ accurate. Also location of $(v) = 0$ depends on τ. It means there is no general theory of bounce-back boundary conditions.

2.7.3 Free-slip boundary conditions

The free slip boundary condition [83] can be employed to the case of smooth boundaries where the normal component of the population velocity $\mathbf{u}_n$ and normal derivative of its tangential component $\partial \mathbf{u}_t / \partial n$ both vanish. The on-site specular reflection of the population on the north wall in a two-dimensional rectangular channel is shown in Figure (2.7). These boundary conditions on the north wall can be expressed in terms of the following boundary matrix:

$$\begin{bmatrix} f_4(x,y) \\ f_7(x,y) \\ f_8(x,y) \end{bmatrix} = \begin{bmatrix} 0 & 0 & 1 \\ 0 & 1 & 0 \\ 1 & 0 & 0 \end{bmatrix} \begin{bmatrix} f_5(x,y) \\ f_6(x,y) \\ f_2(x,y) \end{bmatrix}. \tag{2.7.7}$$

The boundary conditions on the south wall can be obtained by similar arguments.

For the mid-site specular reflection of the populations on the north wall, as shown in Figure (2.8), the boundary matrix is:

$$\begin{bmatrix} f_4(x,y) \\ f_7(x,y) \\ f_8(x,y) \end{bmatrix} = \begin{bmatrix} 0 & 0 & 1 \\ 0 & 1 & 0 \\ 1 & 0 & 0 \end{bmatrix} \begin{bmatrix} f_5(x-1,y-1) \\ f_6(x+1,y-1) \\ f_2(x,y-1) \end{bmatrix}. \tag{2.7.8}$$

Again through symmetrical arguments, the boundary matrix can be formed for the south wall.

2.7.4 Inlet/Outlet boundary conditions

At the inlet, velocity is specified in the macroscopic description of flow and at the outlet, either a given pressure value or no-flux condition normal to the wall, $\partial_n \mathbf{u}$ is employed.

At the inlet, the particle distribution functions f_i are replaced with the quasi-equilibrium values $f_i^{(eq)}$ that correspond to the free-stream velocity and density. As the simulation result is not very sensitive to the exact condition specified at the inlet boundary, this lower order approximation is sufficient there. For the D2Q9 model, the velocity distribution function on all the inlet nodes reads in form of the following

boundary matrix:

$$\begin{bmatrix} f_1(x_{in}, y) \\ f_5(x_{in}, y) \\ f_8(x_{in}, y) \end{bmatrix} = \begin{bmatrix} 1 & 0 & 0 \\ 0 & 1 & 0 \\ 0 & 0 & 1 \end{bmatrix} \begin{bmatrix} f_1^{(eq)}(\rho(x_{in}+1, y), U_{in}) \\ f_5^{(eq)}(\rho(x_{in}+1, y), U_{in}) \\ f_8^{(eq)}(\rho(x_{in}+1, y), U_{in}) \end{bmatrix}, \tag{2.7.9}$$

where (x_{in}, y) is the site for the inlet boundary.

The outlet boundary condition is more sensitive to the physical domain. This sensitivity has been known in [83]. A simple recipe suggested is to replace the populations at the outlet pointing towards the flow domain by the equilibrium values that correspond to the velocity and density of the penultimate row of the lattice. The boundary matrix becomes:

$$\begin{bmatrix} f_3(x_{out}, y) \\ f_6(x_{out}, y) \\ f_7(x_{out}, y) \end{bmatrix} = \begin{bmatrix} 1 & 0 & 0 \\ 0 & 1 & 0 \\ 0 & 0 & 1 \end{bmatrix} \begin{bmatrix} f_3^{(eq)}(\rho_0, u(x_{out}-1, y)) \\ f_6^{(eq)}(\rho_0, u(x_{out}-1, y)) \\ f_7^{(eq)}(\rho_0, u(x_{out}-1, y)) \end{bmatrix}, \tag{2.7.10}$$

where (x_{out}, y) is the lattice site for the outlet boundary and the equilibrium matrix on right hand side is computed by considering the velocity and density of the penultimate row of the lattice.

2.7.5 Curved boundary treatment

The boundary conditions described above have been used for simple geometrical domains where the boundaries are aligned with the lattice nodes as shown in Figure (2.2). But in case of complex boundaries, where the domains are not regular as shown in Figure (2.3), the boundary conditions must be more delicate. For example in case of curved geometries (such as an obstacle), the approximation of the obstacle with a *staircased* boundary may reduce the computational accuracy.

Unlike other Navier-Stokes solvers where the non-slip boundary conditions for the velocity $\mathbf{u}$ on a solid wall is usually specified in the macroscopic description of fluid flows, the LBM faces difficulties where the non-slip boundary conditions for the particle distribution functions f_i's are not known at the mesoscopic level. Usually, the most frequent boundary conditions used for the solid wall is the $bounce - back$ scheme defined in section (2.7.2). In the bounce-back scheme, the particle distribution function f_i streaming from a fluid node $\mathbf{r}_f$ towards a boundary node $\mathbf{r}_b$ along the direction $\mathbf{e}_i$ is reversed back to the node $\mathbf{r}_f$ along the direction $\mathbf{e}_{-i}$ as $\tilde{f}_{-i}$ as shown in the figure. Because the wall position $\mathbf{r}_w$ was forced to be located at $\mathbf{r}_b$, this scheme is known as bounce-back on the node (BBN). Since a finite slip velocity exists at the stationary wall [38, 61], this results in the degradation of the computational accuracy. Another bounce-back scheme, where the solid wall was placed in the middle between lattice nodes, is known as the bounce-back on the link (BBL). The BBL scheme provided second-order accurate results for the straight walls [38]. However for curved walls, the BBL scheme requires an approximation of the curved solid boundary by a series of stair steps. This results in the deterioration of the geometrical integrity which is very important for high Reynolds number flows where the vorticity and stress distributions are very sensitive to the geometry resolution. For the curved boundary, the interpolation based scheme of Fillipova and Hänel (FH) model [28] with first-order and second-order improvements made by Renwei Mei [66, 67, 68] is described here.

In Figure 2.9, a curved wall separates the solid region from the fluid region. The lattice nodes on the fluid and solid sides are denoted by $\mathbf{r}_f$ and $\mathbf{r}_s$ respectively. The filled small circles on the boundary $\mathbf{r}_w$, denote the intersections of the wall with

different lattice links. The fraction of the intersected link in the fluid region is,

$$\triangle = \frac{|\mathbf{r}_f - \mathbf{r}_w|}{|\mathbf{r}_f - \mathbf{r}_s|}, \qquad where \qquad 0 < \triangle \leq 1. \tag{2.7.11}$$

The horizontal and vertical distance between $\mathbf{r}_f$ and $\mathbf{r}_w$ is $\triangle\delta x$ on the square lattice. After the collision step, $\tilde{f}_i(\mathbf{r}_f, t)$ on the fluid side is known and $\tilde{f}_{-i}(\mathbf{r}_s, t)$ on the solid side is to be determined. To find the unknown value $\tilde{f}_{-i}(\mathbf{r}_s, t) = f_{-i}(\mathbf{r}_f = \mathbf{r}_s + \mathbf{e}_{-i}\delta t, t + \delta t)$, based on information in the surrounding fluid nodes like $\tilde{f}_i(\mathbf{r}_f, t)$, $\tilde{f}_i(\mathbf{r}_{ff}, t)$ etc., FH [28] constructed the following linear interpolation:

$$\tilde{f}_{-i}(\mathbf{r}_s, t) = (1 - \chi)\tilde{f}_i(\mathbf{r}_f, t) + \chi f_i^*(\mathbf{r}_s, t) - 2w_i\rho\frac{3}{c^2}(\mathbf{e}_{-i} \cdot \mathbf{u}_w), \tag{2.7.12}$$

where $\mathbf{u}_w = \mathbf{u}(\mathbf{r}_w, t)$ is the velocity at wall, χ is the weighting factor, and $f_i^*(\mathbf{r}_s, t)$ is a fictitious equilibrium distribution function defined as:

$$f_i^*(\mathbf{r}_s, t) = w_i\rho(\mathbf{r}_f, t)\left[1 + \frac{3}{c^2}(\mathbf{e}_i \cdot \mathbf{u}_{sf}) + \frac{9}{2c^2}(\mathbf{e}_i \cdot \mathbf{u}_f)^2 - \frac{3}{2c^2}(\mathbf{u}_f \cdot \mathbf{u}_f)\right], \tag{2.7.13}$$

where $\mathbf{u}_f = \mathbf{u}(\mathbf{r}_f, t)$ and $\mathbf{u}_{sf}$ is the fictitious velocity which is to be chosen. For FH model, the relevant equations for χ and $\mathbf{u}_{sf}$ are:

$$\begin{aligned} \triangle < \frac{1}{2}: \quad & \mathbf{u}_{sf} = \mathbf{u}_f, && \chi = \frac{2\triangle - 1}{\tau - 1}, \\ \triangle \geq \frac{1}{2}: \quad & \mathbf{u}_{sf} = \frac{1}{\triangle}(\triangle - 1)\mathbf{u}_f + \frac{1}{\triangle}\mathbf{u}_w, && \chi = \frac{(2\triangle - 1)}{\tau}. \end{aligned} \tag{2.7.14}$$

To improve the numerical stability, Renwei Mei et al. [66] suggested the following first-order modified equations for χ and $\mathbf{u}_{sf}$:

$$\begin{aligned} \triangle < \frac{1}{2}: \quad & \mathbf{u}_{sf} = \mathbf{u}_{ff}, && \chi = \frac{2\triangle - 1}{\tau - 2}, \\ \triangle \geq \frac{1}{2}: \quad & \mathbf{u}_{sf} = \frac{1}{\triangle}(\triangle - 1)\mathbf{u}_f + \frac{1}{\triangle}\mathbf{u}_w, && \chi = \frac{(2\triangle - 1)}{\tau}, \end{aligned} \tag{2.7.15}$$

and the second-order improvements in the curved boundary give the following modified equations for χ and $\mathbf{u}_{sf}$:

$$\begin{aligned} \triangle < \frac{1}{2}: \qquad & \mathbf{u}_{sf} = \mathbf{u}_{ff}, && \chi = \frac{2\triangle - 1}{\tau - 2}, \\ \triangle \geq \frac{1}{2}: \qquad & \mathbf{u}_{sf} = \frac{1}{2\triangle}(2\triangle - 3)\mathbf{u}_f + \frac{3}{2\triangle}\mathbf{u}_w, && \chi = \frac{(2\triangle - 1)}{\tau + 1/2}. \end{aligned} \tag{2.7.16}$$

In current simulations, Eqs. (2.7.15) and Eqs. (2.7.16) are used to obtain the values χ and $\mathbf{u}_{sf}$ and these values are then substituted into Eq. (2.7.13) to find $f_i^*(\mathbf{r}_s, t)$ and finally the unknown values $\tilde{f}_{-i}(\mathbf{r}_s, t)$ are found from Eq. (2.7.12).

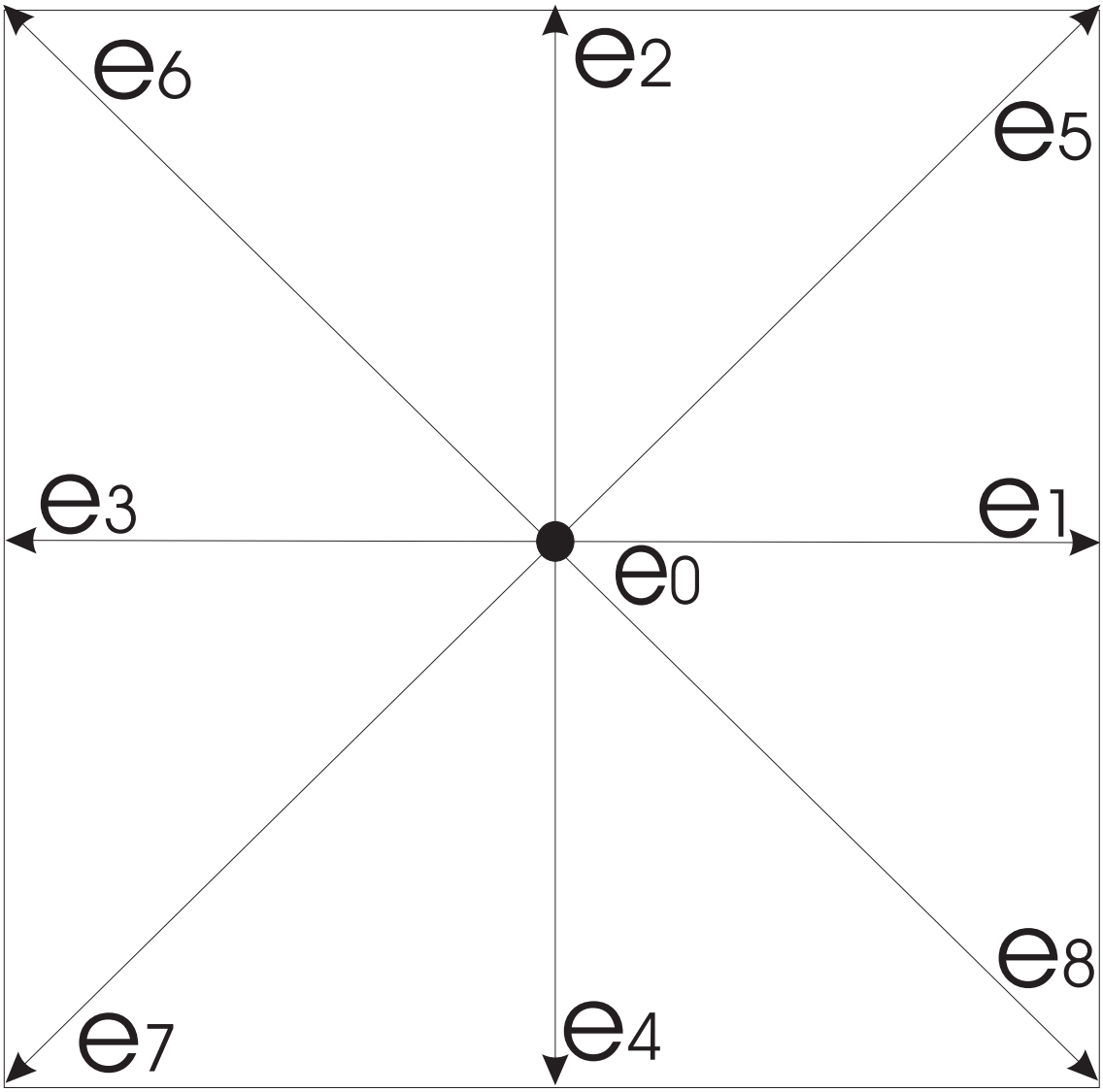

Figure 2.1: Two-dimensional D2Q9 lattice

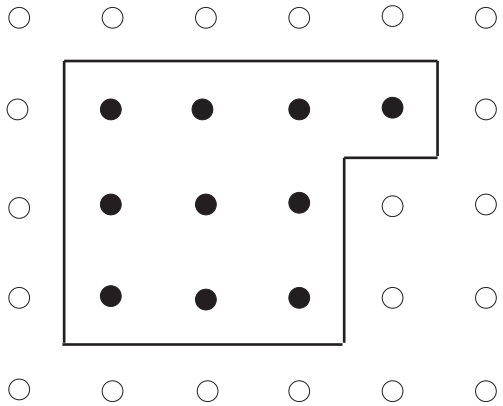

Figure 2.2: Layout for the staircased regular boundaries on the lattice. The straight lines represents the boundary wall, the empty circles denote the fluid nodes and the solid circles denote the wall nodes, respectively.

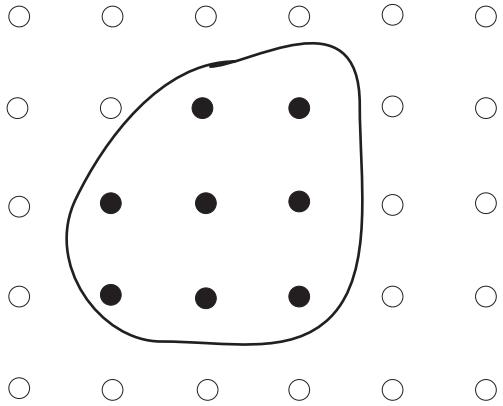

Figure 2.3: Layout for the irregular boundaries on the lattice. The thick curve represents the boundary wall, the empty circles denote the fluid nodes and the solid circles denote the wall nodes, respectively.

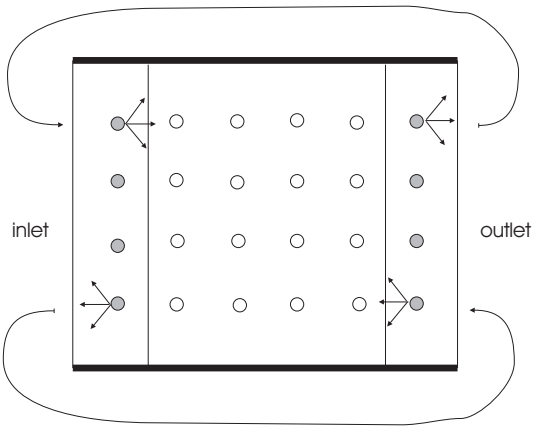

Figure 2.4: Layout for the periodic boundary conditions for a rectangular channel. The shaded solid circles are in the buffer zone and the empty circles are in the internal sites of the channel, respectively.

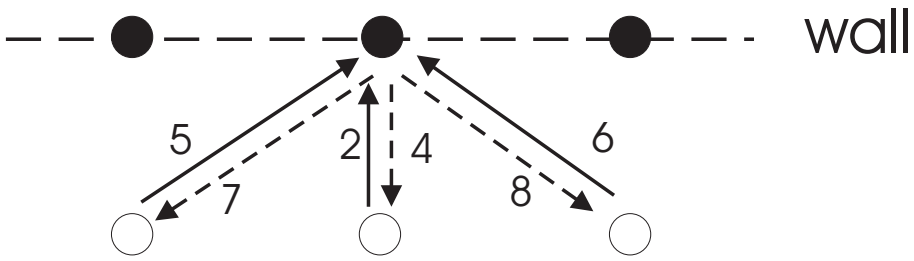

Figure 2.5: Layout for the on-grid bounce-back boundary conditions. The thick arrows represent in-states, the dashed arrows represent the out-states, the empty circles denote the fluid nodes and solid circles denote the wall nodes, respectively.

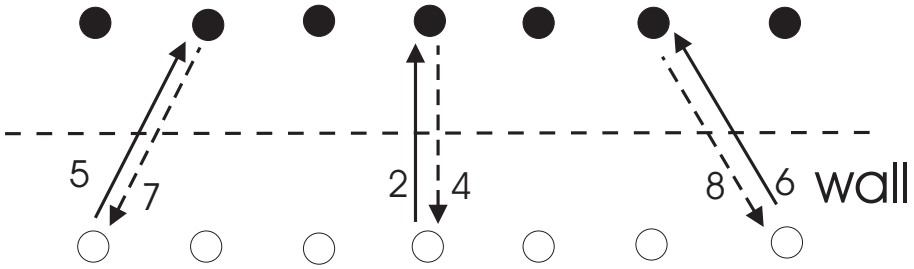

Figure 2.6: Layout for the mid-grid bounce-back boundary conditions. The thick arrows represent in-states, the dashed arrows represent the out-states, the empty circles denote the fluid nodes and solid circles denote the wall nodes, respectively.

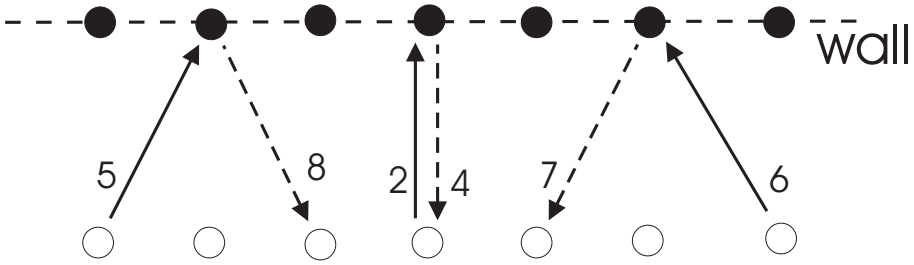

Figure 2.7: Layout for the on-site free-slip boundary conditions. The thick arrows represent in-states, the dashed arrows represent the out-states, the empty circles denote the fluid nodes and solid circles denote the wall nodes, respectively.

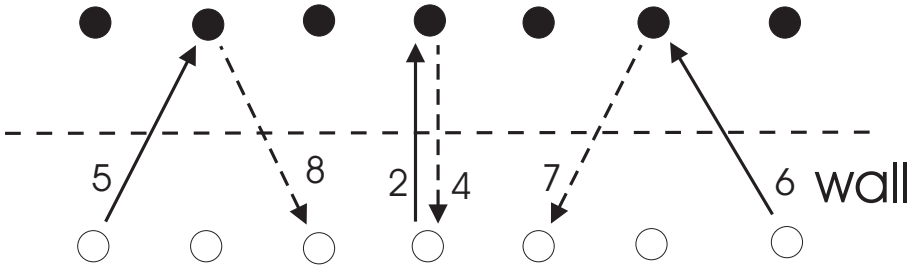

Figure 2.8: Layout for the mid-site free-slip boundary conditions. The thick arrows represent in-states, the dashed arrows represent the out-states, the empty circles denote the fluid nodes and solid circles denote the wall nodes, respectively.

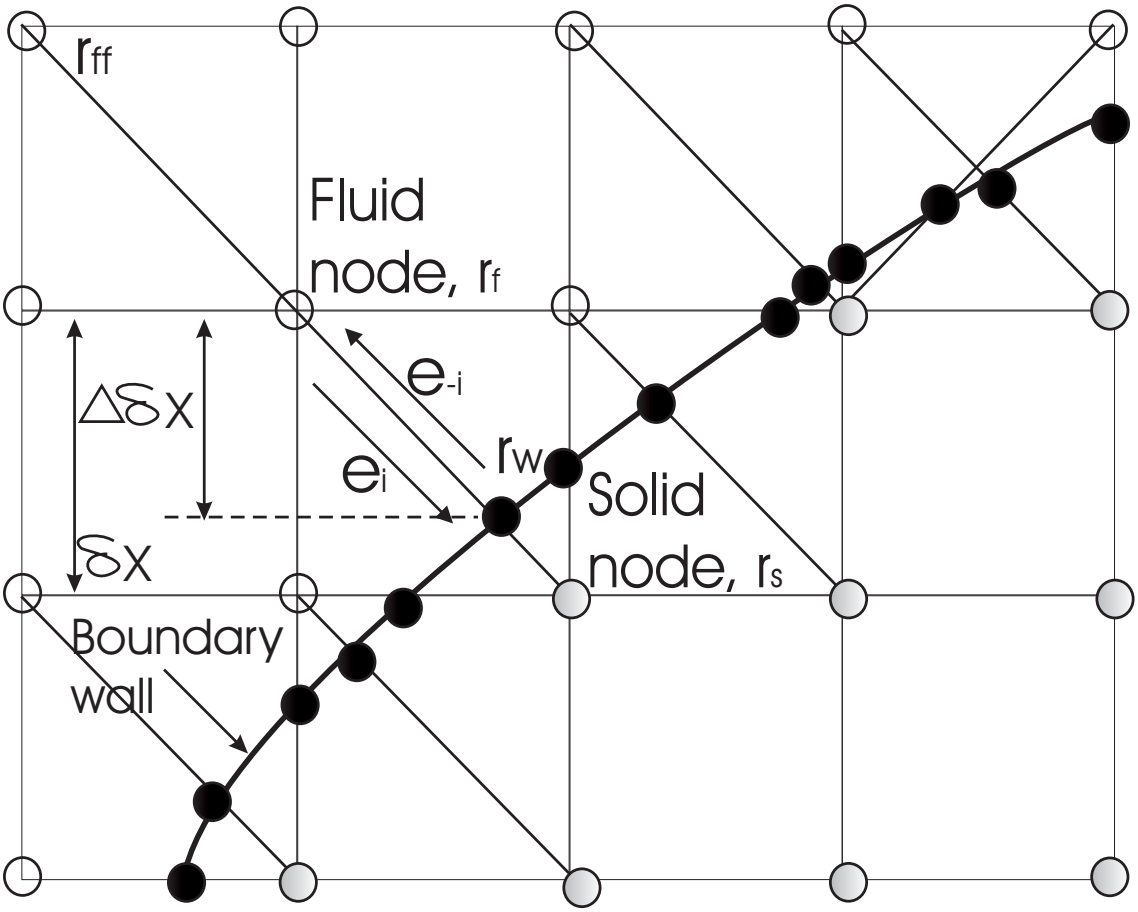

Figure 2.9: Layout for the curved boundary on the lattice. The thick curve represents the boundary wall, the empty circles denote the fluid nodes, solid circles denote the wall nodes and the shaded solid circles denote the solid nodes, respectively.

Chapter 3

Stabilizing the LBM using the Ehrenfests' limiter

The LBM has been successful in simulating various flows of engineering interest for the last few years. However, it is found that it exhibits numerical instabilities in some cases where large gradients are present, such as in the vicinity of shocks and the low viscosity regimes for the boundary layer regions of flows around bluff bodies. These instabilities are mostly due to the negativity of the distribution functions and large deviations of the distribution functions from their equilibrium values. To overcome this problem, Brownlee et. al [17, 18, 19, 20] proposed a versatile approach, the LBM with Ehrenfests' steps. In this approach, the deviations of the population distribution functions f from their equilibrium values $f^{(eq)}$ are controlled by monitoring the microscopic entropy $S(f)$ and the macroscopic entropy $S(f^{(eq)})$ in the simulation. A threshold value is set for the difference of the two entropies and the populations are returned to their equilibrium states by performing a single Ehrenfests' step, if this threshold value is exceeded.

In this chapter, we describe the main idea behind the above mentioned approach, the Ehrenfests' coarse-graining. We show that the Ehrenfests' chain provides an approximation of the Euler equation to the first order and the Navier-Stokes to the second order. Further, we will see that the Ehrenfests' stabilization, described above, can be applied for both entropic and non-entropic quasiequilibria.

3.1 The Ehenfests' coarse-graining

To describe the idea of Ehrenfests' coarse-graining [27], we recall the Boltzmann kinetic transport Equation (2.4.14):

$$\frac{\partial f}{\partial t} + \mathbf{v} \cdot \nabla f = Q(f), \tag{3.1.1}$$

with a strictly concave entropy functional $S(f)$.

In the Ehrenfests' method [27], the phase space was divided into cells and then after providing the mechanical motion from Equation (3.1.1) with periodical averaging in cells, the piecewise constant, or coarse-grained densities were produced. This operation gives rise to an entropy increase. A generalization of this coarse-graining [34] was introduced for the LBM where averaging in cells is replaced by some other partial equilibration procedure.

3.1.1 The quasiequilibrium manifod

Let m be a linear operator which transforms the microscopic variables f to the vector of the macroscopic variables $M = m(f)$:

$$M = \begin{pmatrix} \rho \\ \rho u_1 \\ \rho u_2 \\ 2E \end{pmatrix}, \tag{3.1.2}$$

where ρ, ρu_i and E are the moments of the distribution function f defined by Equations (2.4.15), (2.4.16) and (2.4.17).

An infinite number of distribution functions can provide any particular macroscopic configuration M. For any fixed macroscopic description, M, there will be a unique solution, $f^{(eq)}$ of the following optimization problem

$$S(f) \to max, \qquad m(f) = M, \tag{3.1.3}$$

where $S(f)$ is an entropy functional.

The state $f^{(eq)}$ is called the *quasiequilibrium* as it is not a proper thermodynamic equilibrium. The manifold of the quasiequilibria, parameterized by the macroscopic moments M, as shown in the Figure (3.1), is called the *quasiequilibrium* (QE) manifold.

For the Boltzmann entropy,

$$S = -\int\int f \log f d\mathbf{v}d\mathbf{x}, \tag{3.1.4}$$

the associated quasiequilibrium is the Maxwellian distribution,

$$f^{(eq)} = \frac{\rho^2}{2\pi P} \exp\left(-\frac{\rho}{P}(\mathbf{v}-\mathbf{u})^2\right). \tag{3.1.5}$$

3.1.2 The Ehrenfests' chain

Let $\Theta_\varepsilon : f(\mathbf{x}, t) \longmapsto f(\mathbf{x}, t+\varepsilon)$ be the phase flow transformation of the conservative dynamics for the kinetic eqution (3.1.1). If the collision integral is omitted then the free-flight conservative dynamics: $\Theta_\varepsilon : f(\mathbf{x}, \mathbf{v}, t) \longmapsto f(\mathbf{x} - \varepsilon\mathbf{v}, \mathbf{v}, t)$ means:

$$f(\mathbf{x}, \mathbf{v}, t+\varepsilon) = f(\mathbf{x} - \varepsilon\mathbf{v}, \mathbf{v}, t). \tag{3.1.6}$$

Equation (3.1.6) represents the exact evolution of the population function f at a point and can be interpreted physically as the motion of particles moving freely under their own momentum without any interaction between themselves.

Let ε be a fixed coarse-graining time, $M = m(f)$ be a given macroscopic description and suppose we have an initial quasiequilibrium distribution f_0. The Ehrenfests' chain, as shown in the Figure (3.2), is the following chain of quasiequilibrium distributions $f_0, f_1, ... :$

$$f_j = f^{(eq)}_{m(\Theta_\varepsilon f_{j-1})}, \qquad j = 1, 2, ... \tag{3.1.7}$$

To obtain the next point of the chain, f_j, we take f_{j-1}, move it by the time shift Θ_ε, evaluate the corresponding macroscopic variables $M_j = m(\Theta_\varepsilon(f_{j-1}))$, and find the quasiequilibrium distribution $f^{(eq)}_{M_j} = f_j$.

We can see that entropy increases in the Ehrenfests' chain. If the distribution function $\Theta_\varepsilon(f_j)$ is not a quasi-equilibrium distribution, then $S(\Theta_\varepsilon(f_j)) < S(f^{(eq)}_{m(\Theta_\varepsilon(f_j))})$ because of quasi-equilibrium definition (3.1.3) and strict concavity of the entropy $S(f)$. It means that if the motion between f_j and $\Theta_\varepsilon(f_j)$ does not belong to the quasi-equilibrium manifold, then $S(f_{j+1}) > S(f_j)$, so entropy in the Ehrenfests' chain increases. This entropy growth in the chain consists of two parts: the entropy gain from the mechanical motion (from f_j to $\Theta_\varepsilon(f_j)$) and the gain from the equilibration

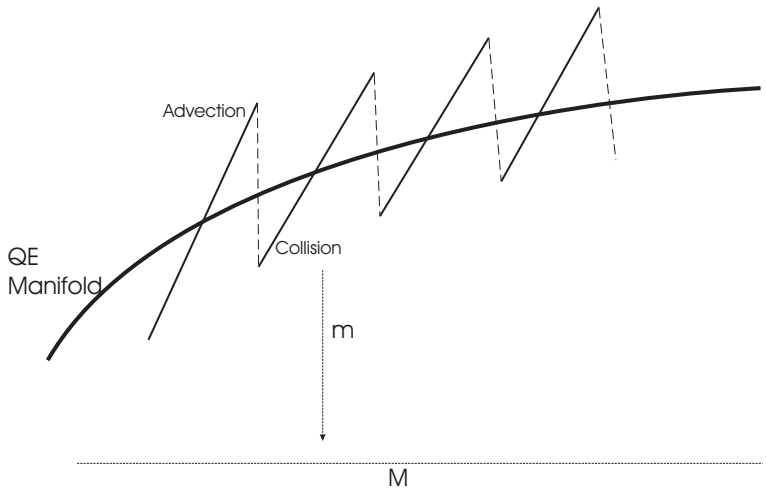

Figure 3.1: Showing the alternating operations of free-flight and collision chain in time near the quasi-equilibrium manifold and the linear map m from the microscopic populations to the macroscopic moments M.

(from $\Theta_\varepsilon(f_j)$ to f_{j+1}). For conservative dynamics, there is zero entropy gain from the first part which implies that entropy gain follows from the second equilibration process. As a result, otherwise conservative systems become dissipative.

3.1.3 Derivation of Navier-Stokes equations

In this section we show that the macroscopic Navier-Stokes equations can be derived in the Ehrenfests' chain after a period of free-flight dynamics. The derivation process done in [19] is presented with some detail here.

The two-dimensional Navier-Stokes continuity and momentum equations (2.1.1)

and (2.1.2) and the energy equation can be written as:

$$\begin{aligned}
&\frac{\partial \rho}{\partial t} + \nabla \cdot (\rho \mathbf{u}) = 0, \\
\frac{\partial}{\partial t}(\rho u_1) &= -\sum_{k=1}^{2} \frac{\partial}{\partial x_k}(\rho u_1 u_k) - \frac{\partial P}{\partial x_1} \\
&\quad +\mu \left[\frac{\partial}{\partial x_1} P \left(\frac{\partial u_1}{\partial x_1} - \frac{\partial u_2}{\partial x_2} \right) + \frac{\partial}{\partial x_2} P \left(\frac{\partial u_2}{\partial x_1} + \frac{\partial u_1}{\partial x_2} \right) \right], \\
\frac{\partial}{\partial t}(\rho u_2) &= -\sum_{k=1}^{2} \frac{\partial}{\partial x_k}(\rho u_2 u_k) - \frac{\partial P}{\partial x_2} \\
&\quad +\mu \left[\frac{\partial}{\partial x_2} P \left(\frac{\partial u_2}{\partial x_2} - \frac{\partial u_1}{\partial x_1} \right) + \frac{\partial}{\partial x_1} P \left(\frac{\partial u_1}{\partial x_2} + \frac{\partial u_2}{\partial x_1} \right) \right], \\
\frac{\partial E}{\partial t} &= -\sum_{i=1}^{2} \frac{\partial}{\partial x_i} \left(u_i (E + P) \right) + \mu \sum_{i=1}^{2} \frac{\partial}{\partial x_i} \left(P \frac{\partial P}{\partial x_i} \right),
\end{aligned} \tag{3.1.8}$$

where the pressure P is given in terms of energy E as

$$P = E - \frac{1}{2}\rho \mathbf{u}^2,$$

where the Boltzmann constant has been set equal to 1.

We are looking to determine the macroscopic dynamics which is approximated by the Ehrenfests' chain. Let us seek for the macroscopic equation of the form:

$$\frac{\partial M}{\partial t} = \Psi(M), \tag{3.1.9}$$

with the phase flow $\Phi_t : M(t) = \Phi_t M(0)$. The transformation Φ_t with $t = \varepsilon$ should coincide with the transformation $M \longmapsto m(\Theta_\varepsilon(f_M^{(eq)}))$ up to second order in ε. The matching condition is

$$m(\Theta_\varepsilon(f_M^{(eq)})) = \Phi_\varepsilon(M), \tag{3.1.10}$$

for every M and given ε. This condition is the expression for the macroscopic field $\Psi(M)$ in Equation (3.1.9). The solution of this equation is a function of ε: $\Psi = \Psi(M, \varepsilon)$. For a sufficiently smooth microscopic field, like free-flight dynamics, and

entropy $S(f)$, it is easy to find the Taylor series expansion of $\Psi(M,\varepsilon)$ in powers of ε. Expanding this for small ε in a series:

$$\Psi(M,\varepsilon) = \Psi^{(0)}(M) + \varepsilon\Psi^{(1)}(M) + o(\varepsilon^2).$$

Let us find the first two terms $\Psi^{(0)}(M)$ and $\Psi^{(1)}(M)$ in the expansion.

In phase space the free-flight dynamics of the system is represented by

$$\frac{\partial f}{\partial t} + \mathbf{v}\cdot\nabla f = 0, \tag{3.1.11}$$

with exact solution given by

$$\Theta_\varepsilon(f_0(\mathbf{x},\mathbf{v})) = f_0(\mathbf{x}-\mathbf{v}t,\mathbf{v}). \tag{3.1.12}$$

Since f_0 is on the quasi-equilibrium manifold, it will be replaced with $f^{(eq)}$ hereafter.

The Taylor series expansion in time for the dynamics of the distribution f up to second order is

$$\begin{aligned}\Theta_\varepsilon(f^{(eq)}) &= \Theta_0(f^{(eq)}) + \varepsilon\left.\frac{\partial\Theta_t}{\partial t}\right|_{t=0} + \frac{\varepsilon^2}{2}\left.\frac{\partial^2\Theta_t}{\partial t^2}\right|_{t=0}\\ &= f^{(eq)} - \varepsilon\mathbf{v}\cdot\nabla f^{(eq)} + \frac{\varepsilon^2}{2}\mathbf{v}\cdot\nabla(\mathbf{v}\cdot\nabla f^{(eq)}).\end{aligned} \tag{3.1.13}$$

This implies, to second order,

$$m(\Theta_\varepsilon(f^{(eq)})) = m(\Theta_0(f^{(eq)})) - \varepsilon m(\mathbf{v}\cdot\nabla f^{(eq)}) + \frac{\varepsilon^2}{2}m(\mathbf{v}\cdot\nabla(\mathbf{v}\cdot\nabla f^{(eq)})). \tag{3.1.14}$$

A similar second-order expansion of M gives

$$\begin{aligned}M(\varepsilon) &= M(0) + \varepsilon\left.\frac{\partial M}{\partial t}\right|_{t=0} + \frac{\varepsilon^2}{2}\left.\frac{\partial^2 M}{\partial t^2}\right|_{t=0}\\ &= M(0) + \varepsilon(\Psi^{(0)}(M) + \varepsilon\Psi^{(1)}(M)) + \frac{\varepsilon^2}{2}\frac{\partial\Psi^{(0)}(M)}{\partial t}.\end{aligned} \tag{3.1.15}$$

Since $M(0) = m(\Theta_0(f^{(eq)}))$, after equating Equations (3.1.14) and (3.1.15) we have

$$-\varepsilon m(\mathbf{v}\cdot\nabla f^{(eq)}) + \frac{\varepsilon^2}{2}m(\mathbf{v}\cdot\nabla(\mathbf{v}\cdot\nabla f^{(eq)})) = \varepsilon(\Psi^{(0)}(M) + \varepsilon\Psi^{(1)}(M)) + \frac{\varepsilon^2}{2}\frac{\partial\Psi^{(0)}(M)}{\partial t}. \tag{3.1.16}$$

Comparing the first-order terms, we get

$$\Psi^{(0)}(M) = -m(\mathbf{v}\cdot\nabla f^{(eq)}). \tag{3.1.17}$$

Comparing second-order terms, we get

$$\Psi^{(1)}(M) + \frac{1}{2}\frac{\partial\Psi^{(0)}(M)}{\partial t} = \frac{1}{2}m(\mathbf{v}\cdot\nabla(\mathbf{v}\cdot\nabla f^{(eq)})),$$

which upon rearrangement becomes

$$\Psi^{(1)}(M) = \frac{1}{2}\left(m(\mathbf{v}\cdot\nabla(\mathbf{v}\cdot\nabla f^{(eq)})) - \frac{\partial\Psi^{(0)}(M)}{\partial t}\right). \tag{3.1.18}$$

Thus, to second-order, the macroscopic equations are

$$\frac{\partial}{\partial t}m(f^{(eq)}) = -m(\mathbf{v}\cdot\nabla f^{(eq)}) + \frac{\varepsilon}{2}\left(m(\mathbf{v}\cdot\nabla(\mathbf{v}\cdot\nabla f^{(eq)})) - \frac{\partial\Psi_0(M)}{\partial t}\right). \tag{3.1.19}$$

Now we calculate the moments of the distribution $f^{(eq)}$ which would help in determining the macroscopic dynamics. Firstly, from definition (2.4.15), we have

$$\begin{aligned} \int f^{(eq)}d\mathbf{v} &= \rho, \\ \int v_i f^{(eq)}d\mathbf{v} &= \rho u_i, \qquad\qquad i = 1,2, \\ \int \mathbf{v}^2 f^{(eq)}d\mathbf{v} &= 2E = 2P + \rho\mathbf{u}^2. \end{aligned} \tag{3.1.20}$$

Next we have

$$\begin{aligned} \int (v_i - u_i)(v_j - u_j)f^{(eq)}d\mathbf{v} &= \int v_i v_j f^{(eq)}d\mathbf{v} - u_i\int v_j f^{(eq)}d\mathbf{v} \\ &\quad -u_j\int v_i f^{(eq)}d\mathbf{v} + u_i u_j\int f^{(eq)}d\mathbf{v} \\ &= \int v_i v_j f^{(eq)}d\mathbf{v} - u_i\rho u_j - u_j\rho u_i + \rho u_i u_j \\ &= \int v_i v_j f^{(eq)}d\mathbf{v} - \rho u_i u_j, \end{aligned}$$

which implies

$$\int v_i v_j f^{(eq)} d\mathbf{v} = \int (v_i - u_i)(v_j - u_j) f^{(eq)} d\mathbf{v} + \rho u_i u_j. \tag{3.1.21}$$

Further, using the identity

$$\int \alpha\beta e^{-(\alpha^2+\beta^2)} d\alpha d\beta = 0,$$

it follows by a change of variables that, for $i \neq j$,

$$\int (v_i - u_i)(v_j - u_j) f^{(eq)} d\mathbf{v} = 0.$$

From the identity, we can see that

$$\int \alpha^2 e^{-(\alpha^2+\beta^2)} d\alpha d\beta = \int \beta^2 e^{-(\alpha^2+\beta^2)} d\alpha d\beta,$$

from which follows that

$$\begin{aligned}
\int (v_j - u_j)^2 f^{(eq)} d\mathbf{v} &= \frac{1}{2} \int (\mathbf{v} - \mathbf{u})^2 f^{(eq)} d\mathbf{v} \\
&= \frac{1}{2} \int (\mathbf{v}^2 + \mathbf{u}^2 - 2v_1 u_1 - 2v_2 u_2) f^{(eq)} d\mathbf{v} \\
&= \frac{1}{2}(2P + \rho\mathbf{u}^2 + \rho\mathbf{u}^2 - 2\rho u_1^2 - 2\rho u_2^2) \\
&= P.
\end{aligned}$$

Hence, from Equation (3.1.21), we have

$$\int v_i v_j f^{(eq)} d\mathbf{v} = \delta_{i,j} P + \rho u_i u_j, \tag{3.1.22}$$

where the Kronecker delta, $\delta_{i,j}$ is defined as

$$\delta_{i,j} = \begin{cases} 1, & i = j, \\ 0, & i \neq j. \end{cases} \tag{3.1.23}$$

Through similar calculations, we have

$$\int v_i v_j v_k f^{(eq)} d\mathbf{v} = (\delta_{i,j}u_k + \delta_{i,k}u_j + \delta_{j,k}u_i)P + \rho u_i u_j u_k. \tag{3.1.24}$$

Now we consider the first term $m(\mathbf{v}\cdot\nabla f^{(eq)})$ in the right hand side of Equation (3.1.19). Using Equation (3.1.20), the first component is

$$\begin{aligned} m_1(\mathbf{v}\cdot\nabla f^{(eq)}) &= \int \mathbf{v}\cdot\nabla f^{(eq)} d\mathbf{v} \\ &= \int v_1 \frac{\partial f^{(eq)}}{\partial x_1} + v_2 \frac{\partial f^{(eq)}}{\partial x_2} d\mathbf{v} \\ &= \frac{\partial}{\partial x_1}\int v_1 f^{(eq)} d\mathbf{v} + \frac{\partial}{\partial x_2}\int v_2 f^{(eq)} d\mathbf{v} \\ &= \frac{\partial}{\partial x_1}(\rho u_1) + \frac{\partial}{\partial x_2}(\rho u_2) \\ &= \nabla\cdot(\rho u). \end{aligned} \tag{3.1.25}$$

Using Equation (3.1.22), the second and third components are

$$\begin{aligned} m_2(v\cdot\nabla f^{(eq)}) &= \int v_1 \mathbf{v}\cdot\nabla f^{(eq)} d\mathbf{v} \\ &= \frac{\partial}{\partial x_1}\int v_1^2 f^{(eq)} d\mathbf{v} + \frac{\partial}{\partial x_2}\int v_1 v_2 f^{(eq)} d\mathbf{v} \\ &= \frac{\partial}{\partial x_1}(P + \rho u_1^2) + \frac{\partial}{\partial x_2}(\rho u_1 u_2), \end{aligned} \tag{3.1.26}$$

$$\begin{aligned} m_3(v\cdot\nabla f^{(eq)}) &= \int v_2 \mathbf{v}\cdot\nabla f^{(eq)} d\mathbf{v} \\ &= \frac{\partial}{\partial x_1}(\rho u_1 u_2) + \frac{\partial}{\partial x_2}(P + \rho u_2^2). \end{aligned} \tag{3.1.27}$$

Finally using Equation (3.1.24), we have

$$\begin{aligned} m_4(v\cdot\nabla f^{(eq)}) &= \int \mathbf{v}^2 v\cdot\nabla f^{(eq)} d\mathbf{v} \\ &= \frac{\partial}{\partial x_1}\int \mathbf{v}^2 v_1 f^{(eq)} d\mathbf{v} + \frac{\partial}{\partial x_2}\int \mathbf{v}^2 v_2 f^{(eq)} d\mathbf{v} \\ &= \frac{\partial}{\partial x_1}(4u_1 P + \rho u_1 \mathbf{u}^2) + \frac{\partial}{\partial x_2}(4u_2 P + \rho u_2 \mathbf{u}_2^2) \\ &= 2\left(\frac{\partial}{\partial x_1}\left(u_1(E+P)\right) + \frac{\partial}{\partial x_2}\left(u_2(E+P)\right)\right). \end{aligned} \tag{3.1.28}$$

Hence, from Equations (3.1.25) to (3.1.28), the first-order approximation of the macroscopic dynamics is Equation (3.1.8) with $\mu = 0$, which are the Euler equations. From these equations, we can write the components of $\Psi^0(M)$ in terms of the macroscopic variables M_i as defined by Equation (3.1.2)

$$\begin{aligned}
\Psi_0^{(0)}(M) &= -m_1(\mathbf{v}\cdot\nabla f^{(eq)}) \\
&= -\frac{\partial}{\partial x_1}\rho u_1 - \frac{\partial}{\partial x_2}\rho u_2 \\
&= -\frac{\partial}{\partial x_1}M_1 - \frac{\partial}{\partial x_2}M_2.
\end{aligned} \tag{3.1.29}$$

$$\begin{aligned}
\Psi_1^{(0)}(M) &= -m_2(\mathbf{v}\cdot\nabla f^{(eq)}) \\
&= -\frac{\partial}{\partial x_1}(P+\rho u_1^2) - \frac{\partial}{\partial x_2}(\rho u_1 u_2) \\
&= -\frac{1}{2}\frac{\partial}{\partial x_1}(2P+2\rho u_1^2) - \frac{\partial}{\partial x_2}\left(\frac{\rho u_1 \rho u_2}{\rho}\right) \\
&= -\frac{1}{2}\frac{\partial}{\partial x_1}(2E-\rho u^2) - \frac{\partial}{\partial x_1}(\rho u_1^2) - \frac{\partial}{\partial x_2}\left(\frac{M_1 M_2}{M_0}\right) \\
&= -\frac{1}{2}\frac{\partial}{\partial x_1}\left(2E - \frac{\rho^2 u_1^2 + \rho^2 u_2^2}{\rho}\right) - \frac{\partial}{\partial x_1}\left(\frac{\rho u_1 \rho u_1}{\rho}\right) - \frac{\partial}{\partial x_2}\left(\frac{M_1 M_2}{M_0}\right) \\
&= -\frac{1}{2}\frac{\partial}{\partial x_1}\left(2E - \frac{M_1^2 + M_2^2}{M_0}\right) - \frac{\partial}{\partial x_1}\left(\frac{M_1 M_1}{M_0}\right) - \frac{\partial}{\partial x_2}\left(\frac{M_1 M_2}{M_0}\right) \\
&= -\frac{1}{2}\frac{\partial}{\partial x_1}\left(M_3 - \frac{M_1^2 + M_2^2}{M_0}\right) - \sum_{i=1}^{2}\frac{\partial}{\partial x_i}\frac{M_1 M_i}{M_0}.
\end{aligned} \tag{3.1.30}$$

$$
\begin{aligned}
\Psi_2^{(0)}(M) &= -m_3(\mathbf{v}\cdot\nabla f^{(eq)}) \\
&= -\frac{\partial}{\partial x_2}(P+\rho u_2^2) - \frac{\partial}{\partial x_1}(\rho u_1 u_2) \\
&= -\frac{1}{2}\frac{\partial}{\partial x_2}(2P+2\rho u_2^2) - \frac{\partial}{\partial x_1}\left(\frac{\rho u_1 \rho u_2}{\rho}\right) \\
&= -\frac{1}{2}\frac{\partial}{\partial x_2}(2E-\rho\mathbf{u}^2) - \frac{\partial}{\partial x_2}(\rho u_2^2) - \frac{\partial}{\partial x_1}\left(\frac{M_1 M_2}{M_0}\right) \\
&= -\frac{1}{2}\frac{\partial}{\partial x_2}\left(2E - \frac{\rho^2 u_1^2+\rho^2 u_2^2}{\rho}\right) - \frac{\partial}{\partial x_2}\left(\frac{\rho u_2 \rho u_2}{\rho}\right) - \frac{\partial}{\partial x_1}\left(\frac{M_1 M_2}{M_0}\right) \\
&= -\frac{1}{2}\frac{\partial}{\partial x_2}\left(2E - \frac{M_1^2+M_2^2}{M_0}\right) - \frac{\partial}{\partial x_2}\left(\frac{M_2 M_2}{M_0}\right) - \frac{\partial}{\partial x_1}\left(\frac{M_1 M_2}{M_0}\right) \\
&= -\frac{1}{2}\frac{\partial}{\partial x_2}\left(M_3 - \frac{M_1^2+M_2^2}{M_0}\right) - \sum_{i=1}^{2}\frac{\partial}{\partial x_i}\frac{M_2 M_i}{M_0}.
\end{aligned}
\tag{3.1.31}
$$

$$
\begin{aligned}
\Psi_3^{(0)}(M) &= -m_4(\mathbf{v}\cdot\nabla f^{(eq)}) \\
&= -2\left(\frac{\partial}{\partial x_1}\left(u_1(E+P)\right) + \frac{\partial}{\partial x_2}\left(u_2(E+P)\right)\right) \\
&= -2\left(\frac{\partial}{\partial x_1}\left(u_1\left(E+E-\frac{1}{2}\rho\mathbf{u}^2\right)\right) + \frac{\partial}{\partial x_2}\left(u_2\left(E+E-\frac{1}{2}\rho\mathbf{u}^2\right)\right)\right) \\
&= -2\left(\frac{\partial}{\partial x_1}\left(\frac{\rho u_1}{\rho}\left(2E - \frac{\rho^2 u_1^2+\rho^2 u_2^2}{2\rho}\right)\right) + \frac{\partial}{\partial x_2}\left(u_2\left(2E - \frac{\rho^2 u_1^2+\rho^2 u_2^2}{2\rho}\right)\right)\right) \\
&= -2\left(\frac{\partial}{\partial x_1}\left(\frac{M_1 M_3}{M_0} - \frac{M_1(M_1^2+M_2^2)}{2M_0^2}\right) + \frac{\partial}{\partial x_2}\left(\frac{M_2 M_3}{M_0} - \frac{M_2(M_1^2+M_2^2)}{2M_0^2}\right)\right).
\end{aligned}
\tag{3.1.32}
$$

Next we seek for the second-order correction

$$
\frac{1}{2}\left(m(\mathbf{v}\cdot\nabla(\mathbf{v}\cdot\nabla f^{(eq)})) - \frac{\partial\Psi_0(M)}{\partial t}\right)
$$

The first component for the first term is

$$\begin{aligned} m_0(\mathbf{v}\cdot\nabla(\mathbf{v}\cdot\nabla f^{(eq)})) &= \int \mathbf{v}\cdot\nabla(\mathbf{v}\cdot\nabla f^{(eq)})d\mathbf{v} \\ &= \sum_{i=1}^{2}\sum_{i=1}^{2}\frac{\partial^2}{\partial x_i\partial x_j}\int v_i v_j f^{(eq)}d\mathbf{v} \\ &= \frac{\partial^2}{\partial x_1^2}\left(P+\rho u_1^2\right)+2\frac{\partial^2}{\partial x_1\partial x_2}\left(\rho u_1 u_2\right) \\ &\qquad +\frac{\partial^2}{\partial x_2^2}\left(P+\rho u_2^2\right). \end{aligned} \tag{3.1.33}$$

The first component, for the second term can be written as

$$\frac{\partial\Psi_0^{(0)}(M)}{\partial t} = \sum_{i=0}^{3}\frac{\partial\Psi_0^{(0)}}{\partial M_i}\left(\frac{\partial M_i}{\partial t}\right) = \sum_{i=0}^{3}\frac{\partial\Psi_0^{(0)}}{\partial M_i}\Psi_i^{(0)}, \tag{3.1.34}$$

where the operators $\frac{\partial\Psi^{(0)}}{\partial M_i}$ are defined as

$$\frac{\partial\Psi_0^{(0)}}{\partial M_0} = \frac{\partial\Psi_0^{(0)}}{\partial M_3} = 0, \qquad \frac{\partial\Psi_0^{(0)}}{\partial M_1} = -\frac{\partial}{\partial x_1}, \qquad \frac{\partial\Psi_0^{(0)}}{\partial M_2} = -\frac{\partial}{\partial x_2},$$

so that Equation (3.1.34) becomes

$$\begin{aligned} \frac{\partial\Psi_0^{(0)}(M)}{\partial t} &= -\frac{\partial}{\partial x_1}\left(\frac{\partial}{\partial x_1}\left(P+\rho u_1^2\right)+\frac{\partial}{\partial x_2}(\rho u_1 u_2)\right) \\ &\quad -\frac{\partial}{\partial x_2}\left(\frac{\partial}{\partial x_2}\left(P+\rho u_2^2\right)+\frac{\partial}{\partial x_1}(\rho u_1 u_2)\right) \\ &= \frac{\partial^2}{\partial x_1^2}\left(P+\rho u_1^2\right)+2\frac{\partial^2}{\partial x_1\partial x_2}\left(\rho u_1 u_2\right)+\frac{\partial^2}{\partial x_2^2}\left(P+\rho u_2^2\right). \end{aligned} \tag{3.1.35}$$

Hence from Equations (3.1.33) and (3.1.35), we see that the first component of the second-order correction is zero, which is true as this is the equation of mass conservation.

Next, we look at the second term in the second-order correction and will keep our focus on the pressure terms only. To determine the correction terms for the Navier-Stokes equations, we require the following terms

$$\frac{\partial\Psi_1^{(0)}}{\partial M_i}, \qquad i = 0,1,2,3.$$

From Equation (3.1.30), we have

$$\Psi_1^{(0)} = -\frac{1}{2}\frac{\partial}{\partial x_1}\left(M_3 - \frac{M_1^2 + M_2^2}{M_0}\right) - \frac{\partial}{\partial x_i}\frac{M_1 M_i}{M_0}.$$

Thus

$$\begin{aligned}\frac{\partial \Psi_1^{(0)}}{\partial M_0} &= -\frac{1}{2}\frac{\partial}{\partial x_1}\left(\frac{M_1^2 + M_2^2}{M_0^2}\right) + \frac{\partial}{\partial x_i}\left(\frac{M_1 M_i}{M_0^2}\right) \\ &= -\frac{1}{2}\frac{\partial}{\partial x_1}u^2 + \frac{\partial}{\partial x_i}u_1 u_i,\end{aligned}$$

$$\begin{aligned}\frac{\partial \Psi_1^{(0)}}{\partial M_1} &= -\frac{1}{2}\frac{\partial}{\partial x_1}\left(-2\frac{M_1}{M_0}\right) - \frac{\partial}{\partial x_1}\left(\frac{2M_1}{M_0}\right) - \frac{\partial}{\partial x_2}\left(\frac{M_1}{M_0}\right) \\ &= -\frac{\partial}{\partial x_1}u_1 - \frac{\partial}{\partial x_2}u_2,\end{aligned}$$

$$\begin{aligned}\frac{\partial \Psi_1^{(0)}}{\partial M_2} &= -\frac{1}{2}\frac{\partial}{\partial x_1}\left(-2\frac{M_1}{M_0}\right) - \frac{\partial}{\partial x_1}\left(\frac{2M_2}{M_0}\right) - \frac{\partial}{\partial x_2}\left(\frac{M_1}{M_0}\right) \\ &= \frac{\partial}{\partial x_1}u_2 - \frac{\partial}{\partial x_2}u_1,\end{aligned}$$

$$\frac{\partial \Psi_1^{(0)}}{\partial M_3} = -\frac{1}{2}\frac{\partial}{\partial x_1}.$$

Hence,

$$\frac{\partial \Psi_1^{(0)}}{\partial M_0}\Psi_0^{(0)} = \left(-\frac{\partial}{\partial x_1}u_2^2 + \frac{\partial}{\partial x_i}u_1 u_2\right)\left(-\frac{\partial}{\partial x_i}\rho u_i\right), \tag{3.1.36}$$

$$\frac{\partial \Psi_1^{(0)}}{\partial M_1}\Psi_1^{(0)} = -\left(\frac{\partial}{\partial x_1}u_1 + \frac{\partial}{\partial x_2}u_2\right)\left(-\frac{\partial}{\partial x_1}P - \frac{\partial}{\partial x_i}(\rho u_1 u_i)\right), \tag{3.1.37}$$

$$\frac{\partial \Psi_1^{(0)}}{\partial M_2}\Psi_2^{(0)} = \left(\frac{\partial}{\partial x_1}u_2 - \frac{\partial}{\partial x_2}u_1\right)\left(-\frac{\partial}{\partial x_2}P - \frac{\partial}{\partial x_i}(\rho u_2 u_i)\right), \tag{3.1.38}$$

$$\frac{\partial \Psi_1^{(0)}}{\partial M_3}\Psi_3^{(0)} = -\frac{1}{2}\frac{\partial}{\partial x_1}\left(-2\frac{\partial}{\partial x_i}u_i\left(2P + \frac{1}{2}\rho \mathbf{u}^2\right)\right). \tag{3.1.39}$$

The second component of the first term for the second-order correction can be found by using Equation (3.1.24)

$$\begin{aligned} m_1(\mathbf{v}\cdot\nabla(\mathbf{v}\cdot\nabla f^{(eq)})) &= \int v_1\mathbf{v}\cdot\nabla(\mathbf{v}\cdot\nabla f^{(eq)})d\mathbf{v} \\ &= \sum_{i=1}^{2}\sum_{i=1}^{2}\frac{\partial^2}{\partial x_i\partial x_j}\int v_1v_iv_jf^{(eq)}d\mathbf{v} \\ &= \sum_{i=1}^{2}\sum_{i=1}^{2}\frac{\partial^2}{\partial x_i\partial x_j}\left((u_i+u_j+\delta_{i,j}u_1)\,P+\rho u_1u_iu_j\right) \\ &= 3\frac{\partial^2}{\partial x_1^2}(u_1P)+\frac{\partial^2}{\partial x_1\partial x_2}(2u_2P) \\ &\quad+\frac{\partial^2}{\partial x_2^2}(u_1P)+\frac{\partial^2}{\partial x_i\partial x_j}(\rho u_1u_iu_j). \end{aligned} \tag{3.1.40}$$

Now if we subtract the pressure terms from Equations (3.1.36) to (3.1.39) from the pressure terms in Equation (3.1.40) and denote this difference by Δ, we have

$$\begin{aligned} \Delta &= 3\frac{\partial^2}{\partial x_1^2}(u_1P)+\frac{\partial^2}{\partial x_1\partial x_2}(2u_2P)+\frac{\partial^2}{\partial x_2^2}(u_1P) \\ &\quad-\frac{\partial}{\partial x_1}u_1\left(\frac{\partial}{\partial x_1}P\right)-\frac{\partial}{\partial x_2}u_2\left(\frac{\partial}{\partial x_1}P\right)+\frac{\partial}{\partial x_1}u_2\left(\frac{\partial}{\partial x_2}P\right) \\ &\quad-\frac{\partial}{\partial x_2}u_1\left(\frac{\partial}{\partial x_2}P\right)-2\left(\frac{\partial^2}{\partial x_1^2}u_1P+\frac{\partial^2}{\partial x_1\partial x_2}u_2P\right) \\ &= \frac{\partial^2}{\partial x_1^2}(u_1P)-\frac{\partial}{\partial x_1}u_1\left(\frac{\partial}{\partial x_1}P\right) \\ &\quad+\frac{\partial^2}{\partial x_2^2}(u_1P)-\frac{\partial}{\partial x_2}u_1\left(\frac{\partial}{\partial x_2}P\right) \\ &\quad+\frac{\partial}{\partial x_1}u_2\left(\frac{\partial}{\partial x_2}P\right)-\frac{\partial}{\partial x_2}u_2\left(\frac{\partial}{\partial x_1}P\right) \\ &= \frac{\partial}{\partial x_1}P\frac{\partial u_1}{\partial x_1}+\frac{\partial}{\partial x_2}P\frac{\partial u_1}{\partial x_2}-\frac{\partial}{\partial x_1}P\frac{\partial u_2}{\partial x_2}+\frac{\partial}{\partial x_2}P\frac{\partial u_2}{\partial x_1} \\ &= \frac{\partial}{\partial x_1}P\left(\frac{\partial u_1}{\partial x_1}-\frac{\partial u_2}{\partial x_2}\right)+\frac{\partial}{\partial x_2}P\left(\frac{\partial u_2}{\partial x_1}+\frac{\partial u_1}{\partial x_2}\right). \end{aligned}$$

Further simplifications of the derivative of terms of the form ρu_iu_j show that they

all cancel and thus we have

$$\begin{aligned}\frac{\partial}{\partial t}(\rho u_1) = &-\sum_{k=1}^{2}\frac{\partial}{\partial x_k}(\rho u_1 u_k) - \frac{\partial P}{\partial x_1} \\ &+\frac{\varepsilon}{2}\left[\frac{\partial}{\partial x_1}P\left(\frac{\partial u_1}{\partial x_1} - \frac{\partial u_2}{\partial x_2}\right) + \frac{\partial}{\partial x_2}P\left(\frac{\partial u_2}{\partial x_1} + \frac{\partial u_1}{\partial x_2}\right)\right],\end{aligned} \tag{3.1.41}$$

which is the second of the Navier-Stokes equations (3.1.8) with coefficient of viscosity $\mu = \varepsilon/2$. Similar computations can provide the other momentum and energy equations. Recently, Packwood et. al [74] has derived these equations from the discrete Boltzmann equation.

3.2 Numerical instabilities in the LBM

The LBM, like other high-order numerical schemes, exhibits numerical instabilities in the low viscosity regimes. These instabilities readily manifest themselves as local blow-ups and spurious oscillations. Below we describe some of the main issues concerning the stability of the LBM.

3.2.1 Negativity of distribution functions

If the probability distribution f is far from the quasiequilibrium, then the positivity of the distribution functions may be violated. Since f represents the whole state which includes the states of all lattice sites. Violation of positivity at one site makes the whole state nonphysical. Of course, violation of positivity of populations (a microscopic condition), does not affect the macroscopic condition immediately. This means, the microscopic positivity is a sufficient but not necessary condition for the macroscopic positivity. This sufficient condition is helpful for the control and for the

construction of limiters that guarantee macroscopic positivity and improve stability [17, 86].

3.2.2 Deviations from quasi-equilibrium manifold

The second issue is the nonlinearity. Since the quasiequilibrium distribution, $f_M^{(eq)}$, depends nonlinearly on M which may cause the distribution f to be far from the quasiequilibrium. Whereas we require the distribution function close to the quasiequilibrium for accuracy. So again deviations from the quasiequilibrium can cause instabilities.

3.2.3 Directional instability

The directional instability is due to the deviation of the vector $f - f^{(eq)}$ from the tangent to the trajectory of the quasiequilibrium manifold. This instability may change the structure of the dissipative terms and conceivably create nonreliable computational results even without blowups.

3.3 Stabilization through Ehrenfests' steps

The Ehrenfests' chain which corresponds to the free-flight and equilibration scheme described above, can be written in terms of the following governing equation

$$\begin{aligned} f_i(\mathbf{x} + \mathbf{v}_i\varepsilon, t + \varepsilon) &= f_i^{(eq)}(\mathbf{x}, t) \\ &= \frac{1}{2} f_i(\mathbf{x}, t) + \frac{1}{2} f_i^{mir}(\mathbf{x}, t), \end{aligned}$$

where the mirror point, $f_i^{mir} = 2f_i^{(eq)}(\mathbf{x}, t) - f_i(\mathbf{x}, t)$ is the reflection of f in the quasiequilibrium manifold. After free-flight dynamics, we move along a vector in the

direction of this mirror point with the BGK collision $Q = -(f - f^{(eq)})/\tau$, we move some part of the way along this direction. Therefore, we can write the above scheme in some general form as

$$f_i(\mathbf{x} + \mathbf{v}_i\varepsilon, t + \varepsilon) = (1 - \beta)f_i(\mathbf{x}, t) + \beta f_i^{mir}(\mathbf{x}, t), \tag{3.3.1}$$

where $\beta = \beta(\varepsilon)$ may be chosen to satisfy a physically relevant condition. A choice of $\beta = 1/2$ gives the Ehrenfests' step with viscosity proportional to the time step $\Delta t = \varepsilon$.

3.3.1 Entropic Involution

As we can see that the dissipative term introduced by the Ehrenfests' chain depends linearly on ε, there exists a symmetry between forward and backward motion in time starting from any quasiequilibrium initial condition [47, 48]. This principle helps to construct chains with zero macroscopic entropy production. One such development is the entropic LBM (ELBM) [47, 49, 50] in which instead of a linear mirror reflection $f \mapsto f^{mir}$ an entropic involution $f \mapsto \tilde{f}$ is used. This chain corresponds to the following governing equation

$$f_i(\mathbf{x} + \mathbf{v}_i\varepsilon, t + \varepsilon) = (1 - \beta)f_i(\mathbf{x}, t) + \beta \tilde{f}_i(\mathbf{x}, t), \tag{3.3.2}$$

where $\tilde{f} = (1 - \alpha)f + \alpha f^{(eq)}$. The number $\alpha = \alpha(f)$ is so chosen that the constant entropy estimate condition, $S(f) = S(\tilde{f})$ is satisfied. This provides a positivity constraint on the populations. For the approximation $\alpha = 2$, we have the corresponding LBM which is the LBGK (3.3.1).

The entropic involution though ensures the existence of positive solutions but affects dissipation because the free-flight dynamics sometimes takes us too far from the quasiequilibrium manifold.

3.3.2 Ehrenfests' steps

As we have described above most of the instabilities in the LBM are caused due to the large deviations of the populations from the quasiequilibrium manifold. In that case, a single Ehrenfests' step is applied and the populations are returned to the quasiequilibrium manifold. This technique is capable of stabilizing the method. In order to keep the method accuracy up to order ε^2, the Ehrenfests' steps are applied at a bounded number of sites.

Let $S(f)$ be the entropy defined for each population vector $f = (f_i)$. Assuming that the global entropy is a sum of local entropies for all sites, the local nonequilibrium entropy is

$$\Delta S(f) = S(f^{(eq)}) - S(f), \tag{3.3.3}$$

where $f^{(eq)}$ is the corresponding local quasiequilibrium at the same point. The Ehrenfests' regularization is intended to keep all states uniformly close to the quasiequilibrium manifold. We monitor the nonequilibrium entropy ΔS at every lattice site throughout the simulation. A pre-specified threshold value δ is set for this entropy deviation and an alarm is triggered if it is exceeded. The alarm simply signals that at the link from the Ehrenfests' chain, an Ehrefests' step is used in place of the regular link of the primary chain at that point. The links of the chain which are very far from the quasiequilibrium states are simply returned to their quasiequilibrium. The result is a chain with additional dissipation. In order to keep the accuracy of the LBGK it is pertinent to perform the Ehrenfests' steps at a bounded number of sites. So we select k sites with highest $\Delta S > \delta$. The a *posteriori* estimates of the added dissipation could easily be performed by analysis of the entropy production in Ehrenfests' steps. As we will show in our results, even a small number of such steps drastically improve stability.

Now the governing LBGK equations with Ehrenfests' step can be written as

$$f_i(\mathbf{x}+\mathbf{v}_i\varepsilon, t+\varepsilon) = \begin{cases} (1-2\beta)f_i(\mathbf{x},t) + 2\beta f_i^{(eq)}(\mathbf{x},t), & \Delta S \le \delta, \\ f_i^{(eq)}(\mathbf{x},t) & otherwise. \end{cases} \tag{3.3.4}$$

In order to keep the accuracy order "on average", the number of sites with Ehrenfests' step should be $O(N\delta_x/L)$, where N is the total number of sites, δ_x is the step of the space discretization and L is the macroscopic characteristic length. This rough estimate of accuracy on average might be destroyed by the concentration of the Ehrenfests' steps in the most nonequilibrium areas, such as in the boundary layer regions. For that case we should replace the total number of sites N in the estimate with the number of sites in that specified region.

3.3.3 Entropy control of non-entropic quasi-equilibria

The discrete quasiequilibria $f^{(eq)}$ can be defined in a number of ways. One of the approaches used to derive the polynomial quasiequilibria [83] is by the postulating of the moment condition: the moments $m(f)$ and their fluxes should coincide for the discrete quasiequilibrium and for the corresponding continuous one. Another way to define the discrete quasiequilibria is based on the entropy condition: the discrete system must have its own thermodynamics and H-theorem and the discrete quasiequilibrium should be the conditional maximum of the discrete entropy. There is not much difference in both types of quasiequilibria. But sometimes there appears a difference such as in case of polynomial equilibrium, the higher moments are considered explicitly and in case of the entropic equilibrium lower order moments are taken into account.

We would like to apply Ehrenfests' stabilization for both entropic as well as nonentropic quasiequilibria. Here we show how the entropic stabilizer can be used for

nonentropic quasiequilibria. If the approximate discrete quasiequilibrium $f^{(eq)}$ is nonentropic, we can use $\Delta S_K(f) = -S_K(f)$ instead of $\Delta S(f)$, where S_K is the Kullback entropy given by

$$S_K(f) = -\sum_i f_i \ln\left(\frac{f_i}{f_i^{(eq)}}\right). \tag{3.3.5}$$

Let the perfect discrete entropy have the standard form for an ideal mixture [48]:

$$S(f) = -\sum_i f_i \ln\left(\frac{f_i}{w_i}\right), \tag{3.3.6}$$

where w_i are the lattice weights defined in Equation (2.5.4). If we define $f^{(eq)}$ as the conditional entropy maximum for given $M_j = \sum_k m_{jk} f_k$, then

$$\ln f_k^{(eq)} = \sum_j \mu_j m_{jk},$$

where $\mu_j(M)$ are the Lagrange multipliers. For this entropy and conditional maximum, it is found [19]

$$\Delta S = S(f^{(eq)}) - S(f) = \sum_i f_i \ln\left(\frac{f_i}{f_i^{(eq)}}\right), \tag{3.3.7}$$

if f and $f^{(eq)}$ have same moments, that is, $m(f) = m(f^{(eq)})$.

The estimate of nonequilibrium entropy can be performed for both entropic and nonentropic quasiequilibria. Any quasiequilibrium is the conditional maximum of the Kullback entropy. The main difference between the Kullback entropy (3.3.7) and the perfect entropy (3.3.6) is dependence of the denominators $f_i^{(eq)}$ on $M = M(f)$.

3.4 Algorithm for our numerical scheme

Here we write a Pseudo code for the fluid simulation around a bluff body in a channel using LBM with Ehrenfests' step.

1. Set all the parameters.

2. Initialize the population distribution functions.

3. Time loop of fluid simulation.

    - Compute inlet and outlet boundary node distribution functions using Equations (2.7.9) and (2.7.10).
    - Compute inner node distribution functions by performing the LBGK collision operation (2.5.7).
    - Compute north and south channel walls nodes distribution functions by performing free slip boundary conditions (2.7.7) and (2.7.8).
    - Compute the bluff body nodes distribution functions by using the improved curved boundary conditions described in the Section (2.7.5).
    - Calculate the entropy S and the nonequilibrium entropy ΔS as described in the Section (3.3).
    - Apply the Ehrenfests' steps using Equation (3.3.4).
    - Compute population distributions for all nodes by performing the streaming operation (2.5.8).
    - Check and save simulation record, data and plot routines.

Chapter 4

Flow Around a Circular Cylinder

The laminar and turbulent unsteady viscous flow around the circular cylinder have been a fundamental fluid mechanics problem due to its wide variety of applications in engineering such as in submarines, bridge piers, towers, pipelines and off shore structures etc. Numerous experimental and numerical investigations [58, 71, 72, 75, 77, 78, 79, 91] have been carried out to understand the complex dynamics of the cylinder wake flow over the last century. This flow is very sensitive to the changes of Reynolds number, a dimensionless parameter representing the ratio of inertia force to viscous force in a flow. Early studies of the flow around a circular cylinder have been done at low Reynolds number. Researchers such as Bloor (1964), Roshko (1954) and Tritton (1959) [12, 77, 88] focused on the flow in the near wake region of the cylinder. With the advent of computer technology in mid 80s, computational fluid dynamics (CFD) started to influence the study of the flow around a circular cylinder. The rapid development of the CFD followed by a wide range of investigations. Results obtained from the CFD simulations [16, 31] between Reynolds numbers of 100 to 300 were found well satisfactory .

Work in this chapter aims to test and validate the efficiency of our model, described in Chapters 2 and 3, for the flow around a circular cylinder. The two-dimensional simulation of the flow around a static cylinder for a wide range of low to moderate Reynolds numbers ($250 < Re < 20,000$), is carried out. The basic flow parameters are simulated and the vortex shedding phenomenon is captured in the wake region of the flow. A detailed comparative study of the flow around a circular cylinder with experimental results at Reynolds number of $3,900$ is conducted. We will show that the LBM with Ehrenfests' steps can quantitatively capture the vortex shedding frequency as a function of Reynolds number and can provide other flow characteristics like drag and lift coefficients which are well in agreement with experimental results.

Starting with the basic overview of the flow around a circular cylinder, the flow characteristics such as the Strouhal number, vortex shedding, drag and lift coefficients are introduced. Then the work carried out by other researchers for the simulation of different turbulence models and its findings are brought into discussion. Following this, results from the current simulation are compared with the experimental works and conclusions on validating the turbulence model are drawn.

4.1 Basic overview of the flow around a circular cylinder

Flow around a circular cylinder tends to follow the shape of the body provided that the velocity of the flow is very slow, this is known as laminar flow. Flow at the inner part of the boundary layers travels more slowly than the flow near to the free stream. As the speed of the flow increases, separation of flow occurs at some point along the body due to the occurrence of the adverse pressure gradient region. Flow separation

tends to roll up the flow into swirling eddies, resulting in alternate shedding of vortices in the wake region of the body known as the von Karman vortex street.

4.1.1 Reynolds Number

The governing dimensionless parameter for the idealized disturbance-free flow around a nominally two-dimensional cylinder is the Reynolds number defined by

$$Re = U_\infty D/\nu, \tag{4.1.1}$$

where U_∞ is the free-stream velocity, D the cylinder diameter and ν the kinematic viscosity as defined in Equation (2.5.6). It has been observed both experimentally and numerically that as the Reynolds number increases, flow begins to separate behind the cylinder causing vortex shedding which leads to a periodic flow known as a Von Karman vortex street.

Roshko in his experimental study [77], has shown that significant patterns of flow occurs as the Reynolds number changes and identified the following regimes for the flow around a circular cylinder:

- Stable (laminar) range, $40 < Re < 150$.
- Transition (from laminar to turbulent) range, $150 < Re < 300$.
- Irregular (turbulent) range, $300 < Re < 10,000+$.

Similar regimes have been confirmed by other experimental and numerical investigations. Zdravkovich [97] has compiled almost all the experimental and numerical simulation data on the flow past circular cylinders and classified this phenomenon into different regimes based on the Reynolds numbers.

4.1.2 Strouhal number

The vortex-shedding frequency is characterized by a dimensionless number, known as the Strouhal number, which defined by

$$St = \frac{f_s D}{U_\infty}, \tag{4.1.2}$$

where D is the diameter of the cylinder, U_∞ is the free-stream inlet velocity and f_s is the vortex shedding frequency. The Strouhal number undergoes a sharp transition around a $Re \sim 49$ and tends to remain almost constant for $250 < Re < 20,000$.

4.1.3 Drag and lift coefficients

Roshko [77] showed a relation between the Strouhal number and the drag coefficient of the flow around a circular cylinder. For Reynolds number $100 < Re < 10,000$, an increase in the Strouhal number is usually followed by a decrease in the drag coefficient. The drag coefficient for a two-dimensional flow is defined as

$$C_D = \frac{2F_x}{\rho U_\infty^2 D}, \tag{4.1.3}$$

where F_x is the sum of pressure and viscous forces on the surface of the cylinder acting along the flow direction.

The lift coefficient is defined as

$$C_L = \frac{2F_y}{\rho U_\infty^2 D}, \tag{4.1.4}$$

where F_y is the force on the surface of the cylinder acting perpendicular to the along-wind direction of the flow.

We have computed the forces F_x and F_y using the momentum exchange method. In the momentum exchange method these forces are given by [68]

$$F_x = \sum_{all x_b} \sum_{\alpha \neq 0} \left[\tilde{f}_\alpha(\mathbf{x}_b, t) - \tilde{f}_{\bar{\alpha}}(\mathbf{x}_b + \mathbf{e}_{\bar{\alpha}} \Delta t) \right] e_{\alpha,x}, \tag{4.1.5}$$

and

$$F_y = \sum_{all x_b} \sum_{\alpha \neq 0} \left[\tilde{f}_\alpha(\mathbf{x}_b, t) - \tilde{f}_{\bar{\alpha}}(\mathbf{x}_b + \mathbf{e}_{\bar{\alpha}} \Delta t) \right] e_{\alpha,y}, \tag{4.1.6}$$

where $e_{\alpha,x}$ denote the x-component of the velocity vector $\mathbf{e}_\alpha$ and $e_{\alpha,y}$ denote the y-component of the velocity vector $\mathbf{e}_\alpha$.

For the analysis of the flows around the bluff bodies, any turbulence model should simulate all the above-mentioned flow parameters correctly.

4.2 Flow around a circular cylinder using LBM with Ehrenfests' steps

In this section flow around a circular cylinder is simulated using the LBM with Ehrenfests' steps. The computational details for the simulation are briefly discussed first. Then a detailed comparison of the current simulations with other numerical and experimental studies is presented.

4.2.1 Computational domain

The computational setup for the flow is as follows: The circular cylinder of diameter D is immersed in a rectangular channel with its axis perpendicular to the flow direction. The length and width of the channel are respectively, 30D and 25D. The cylinder is placed on the center line in the y-direction resulting in a blockage ratio of 4%. The computational domain consists of an upstream of 10.5D and a downstream of 19.5D to the center of the cylinder. The computational grid with these dimensions is shown in Fig. (4.1).

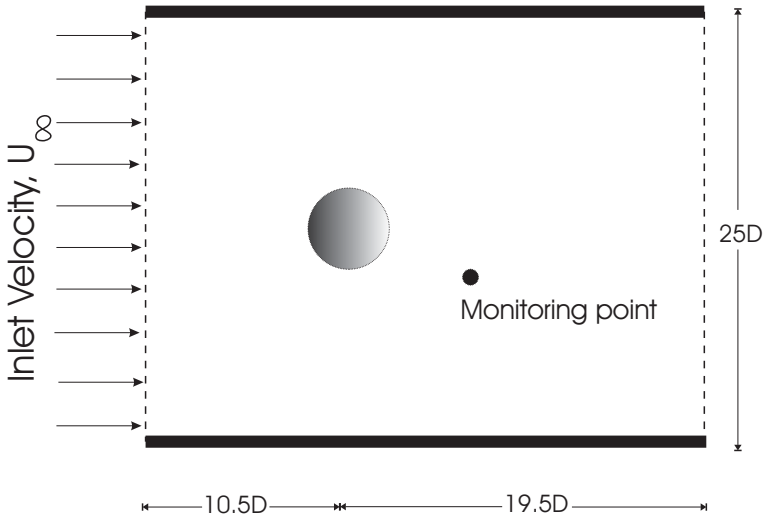

Figure 4.1: Computational setup for flow past a circular cylinder.

4.2.2 Boundary conditions

For all simulations, the inlet velocity is $(U_\infty, V_\infty) = (0.05, 0)$ (in lattice units) and the characteristic length, that is the diameter of the cylinder, is $D = 20$. The vortex shedding frequency f_s is obtained from the discrete Fourier transform of the x-component of the instantaneous velocity at a monitoring point which is located at coordinates $(4D, -2D)$ with center of the cylinder being assumed at the origin. The simulations are recorded over $t_{max} = 1250D/U_\infty$ time steps. The parameter (k, δ) which controls the Ehrenfests' steps tolerances, are fixed at $(16, 10^{-3})$.

The free slip boundary conditions described in Section (2.7.3), are imposed on the north and south channel walls. At the inlet, the populations are replaced with the quasi-equilibrium values that correspond to the free-stream velocity and density (see Section (2.7.4)). As the simulation result is not very sensitive to the exact condition specified at the inlet boundary, this lower order approximation is sufficient there.

The simulation is sensitive to the outlet boundary condition. The sensitivity for this problem has been known in [83]. We follow the prescription suggested in[6, 19]: at the outlet, the populations pointing towards the flow domain are replaced by the equilibrium values that correspond to the velocity and density of the penultimate row of the lattice (see Section (2.7.4)).

On the cylinder wall, the interpolation-based scheme of Fillipova and Hänel model [28] with first-order and second-order improvements made by Renwei Mei [66], are applied (see Section (2.7.5)).

4.2.3 Meshing

A uniform rectangular mesh of 601×501 nodes, is applied for this simulation as shown in Figure (4.2). The lattice nodes coincide with the cartesian coordinates of the mesh. The horizontal and vertical distances between the nodes of the lattice are both set equal to one, i.e. $\delta x = \delta y = 1$ (in lattice units). There is no grid refinement applied near the cylinder walls, as we expect the interpolation-based boundary conditions and the Ehrenfests' step would capture the changes of the velocity gradients and keep the simulation stable.

4.2.4 Computational cost

Computer power plays an important role in the accuracy of any numerical simulation. Present LBM simulations have been carried out on the high performance computing environment provided by the University of Leicester, named, ALICE. Each simulation is carried out on a 2.67GHz Intel Xeon X5550 CPU. For the current simulation, the computing time for a mesh of 0.3 million lattice nodes and 0.5 million iterations (time steps) requires 30 to 40 hours.

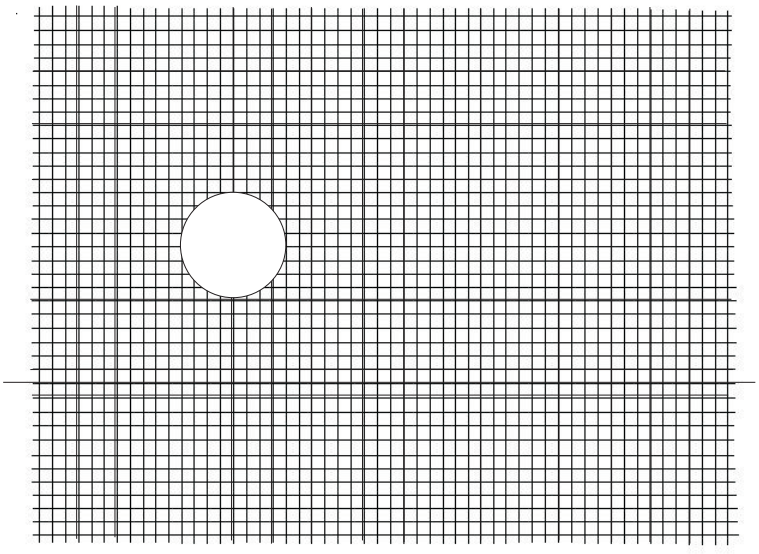

Figure 4.2: A rectangular mesh around a circular cylinder.

4.3 Results and discussion

4.3.1 Strouhal-Reynolds number relationship

The critical Reynolds number at which the vortex shedding behind circular cylinder started, is found to be around 49 [97]. Below this Reynolds number, the wake is in steady state and two symmetric vortices are formed behind the cylinder. As the Reynolds number increases beyond this critical value, the symmetry in the wake is broken and alternating eddies are formed and convected. This results in the alternate separation of vortices which are convected and diffused away from the cylinder and known as the Von Karman vortex streets. Norberg [72] has observed this critical number for the onset of vortex shedding as 47.4. In our simulations, we have found the onset of vortex shedding at $Re = 49$. In our simulations we have found the onset

of vortex shedding at $Re = 49$.

The Strouhal number for the unsteady laminar flow at $Re = 100$ is found to be 0.166 which is well in agreement with the experimental value $(0.164 - 0.165)$ reported by Tritton [88]. The stream function and vorticity snapshots for the unsteady laminar flow at Reynolds numbers $Re = 50, 100, 150$, are shown in Figures (4.5) to (4.10).

In his experimental work, Roshko [77] has reported the beginning of laminar to turbulent transition at Reynolds numbers $200 - 300$. Beyond this Reynolds number, the wake of the cylinder is fully turbulent.

For the stable regime, Roshko [77] found the Strouhal-Reynolds number relationship by the best-fit line

$$St = 0.212 - \frac{4.5}{Re}, \qquad 50 < Re < 150.$$

and for the irregular regime he found

$$St = 0.212 - \frac{2.7}{Re}, \qquad 300 < Re < 2000.$$

Norberg [71] found following best-fit lines for the same two regimes

$$St = 0.211 - \frac{4.6}{Re}, \qquad 50 < Re < 150,$$

$$St = 0.215 - \frac{3.4}{Re}, \qquad 300 < Re < 2000.$$

We have found good agreement for the stable regime with the experimental results of Roshko and Norberg as shown in Figure (4.3). But for the irregular range, the Strouhal number is found slightly overpredicted due to the three dimensional nature of the fluid motion in this range.

Henderson [43] has found , for his 2D computation a very good fit to the Strouhal-Reynolds number data up to $Re = 1,000$ given by

$$St = 0.2417 - 0.8328 Re^{-0.4808} exp(-0.001895 Re),$$

which shows that an asymptote of 0.2417 is reached at large Reynolds numbers. As can be seen from Figure (4.3), present simulations are perfectly matched with the Henderson's curve up to $Re = 1,000$. Rajani [78] simulated two dimensional laminar flow using RANS3D finite volume algorithm for $50 \leq Re \leq 5,000$. The Strouhal-Reynolds number data for the current simulation is closer to the experimental data as compared to that of Rajani as shown in Figure (4.3). An asymptote of 0.24 for Strouhal value is found for large Reynolds numbers.

Note that, we have simulated the flow around circular cylinder for Reynolds number up to $Re = 140,000$. The simulation is stable for about 500 vortex cycles up to $Re = 20,000$. It is stable for about 200 vortex cycles up to $Re = 30,000$ and beyond this Reynolds number the stable number of vortex cycles decreases with increasing Reynolds number. At $Re = 140,000$, only 10 vortex cycles are stable. For higher Reynolds number, the errors from the outer boundary corrupt the simulation. We have presented the flow parameters only for the stable cycles.

4.3.2 Prediction of drag and lift coefficients

The drag drag force is a result of the convective motion of the cylinder through the fluid. The mean drag coefficient computed in the current simulation is very close to the experimental curve [80] as shown in Figure (4.4). A comparison with the numerical results of Rajani [78] shows that current predicted values of mean drag coefficient are much better.

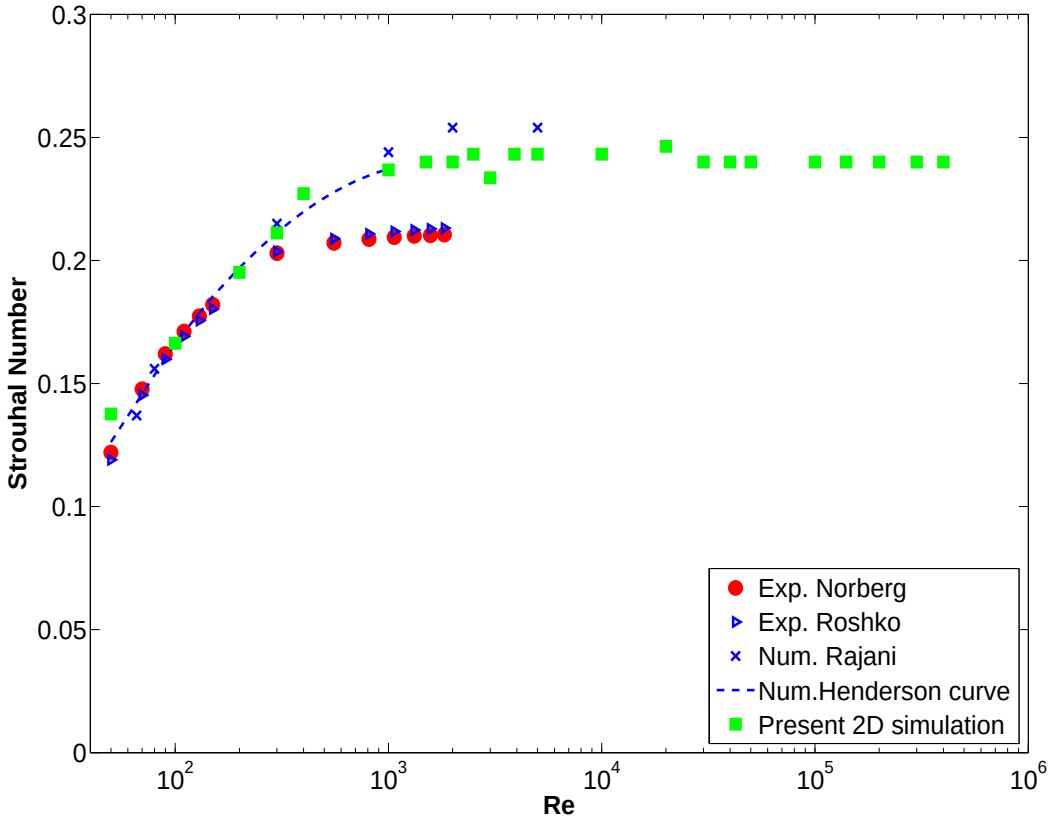

Figure 4.3: A Strouhal-Reynolds number relationship.

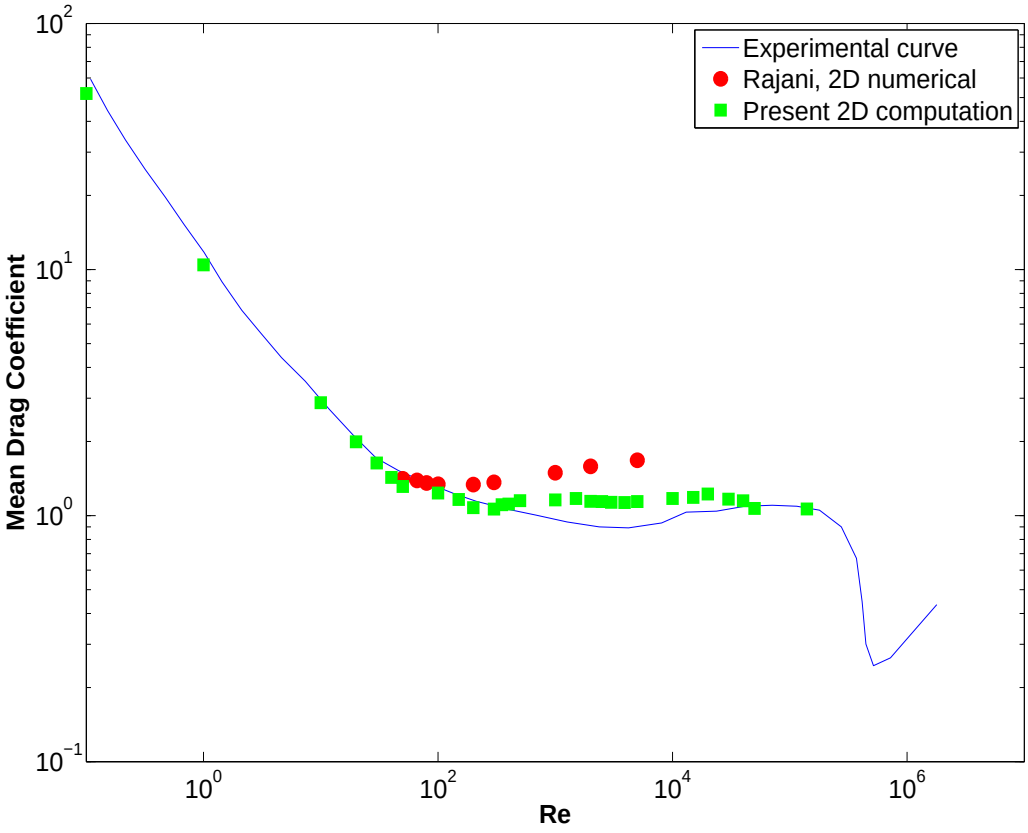

Figure 4.4: Comparison of the drag coefficient with experimental and numerical data.

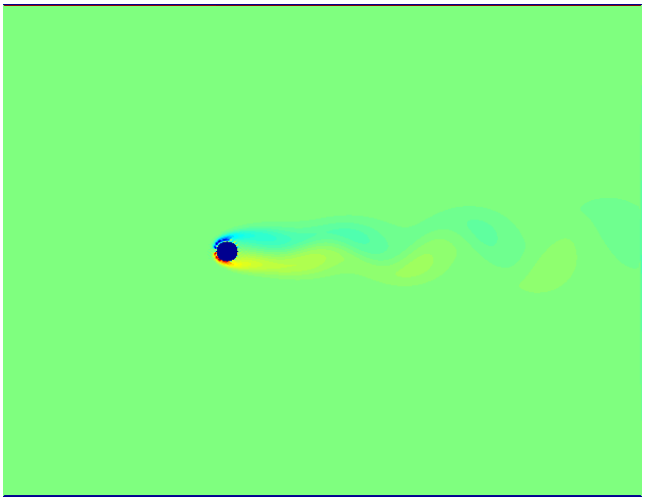

Figure 4.5: A snapshot of vorticity field at $Re = 50$ and $500th$ time step.

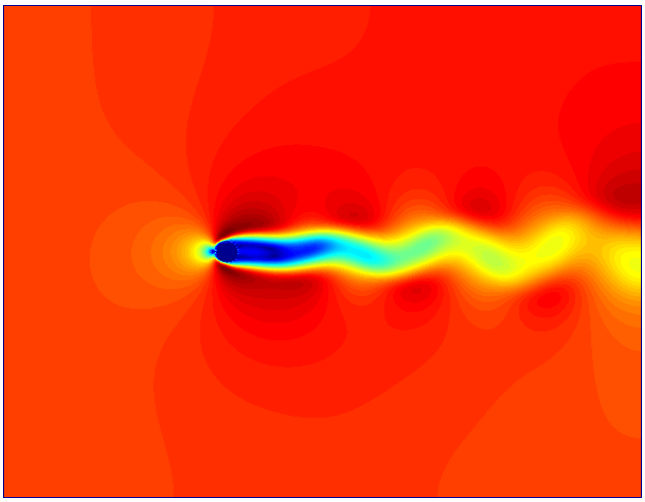

Figure 4.6: A snapshot of stream function at $Re = 50$ and $500th$ time step.

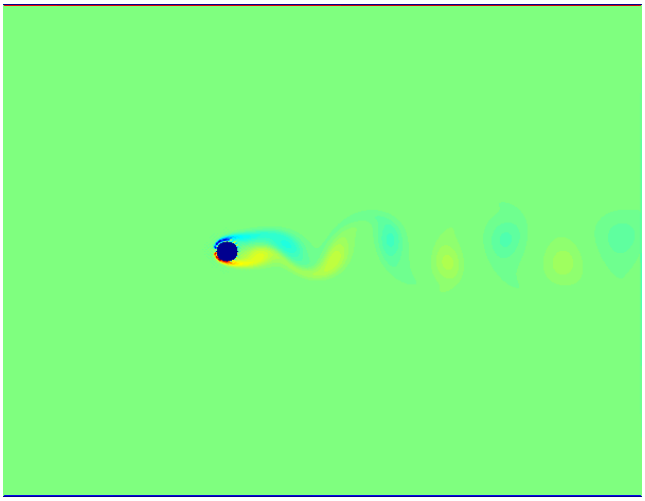

Figure 4.7: A snapshot of vorticity field at $Re = 100$ and $500th$ time step.

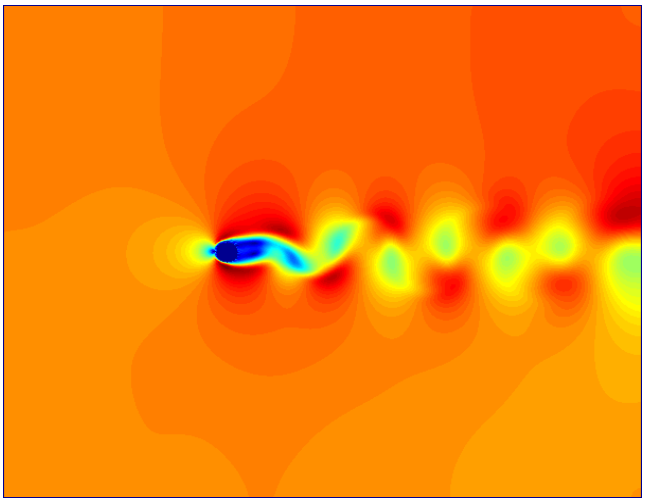

Figure 4.8: A snapshot of stream function at $Re = 100$ and $500th$ time step.

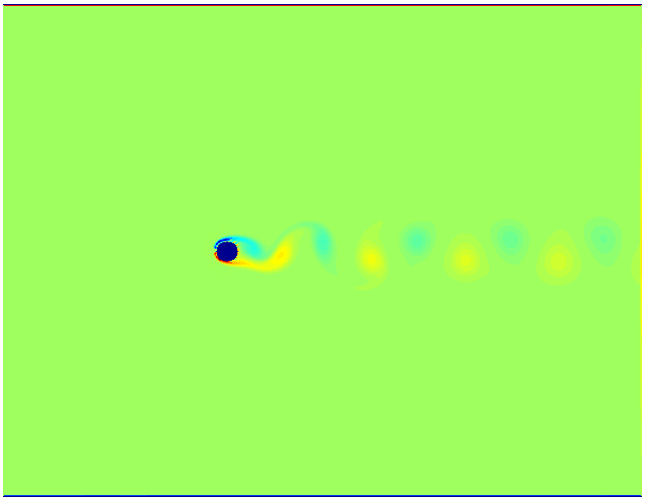

Figure 4.9: A snapshot of vorticity field at $Re = 150$ and $400th$ time step.

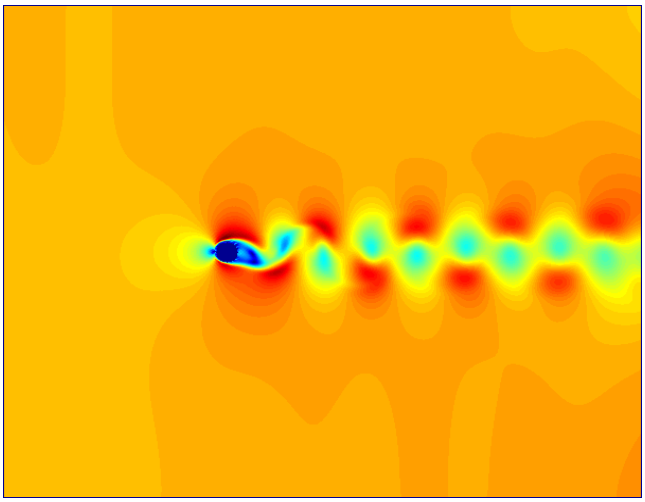

Figure 4.10: A snapshot of stream function at $Re = 150$ and $400th$ time step.

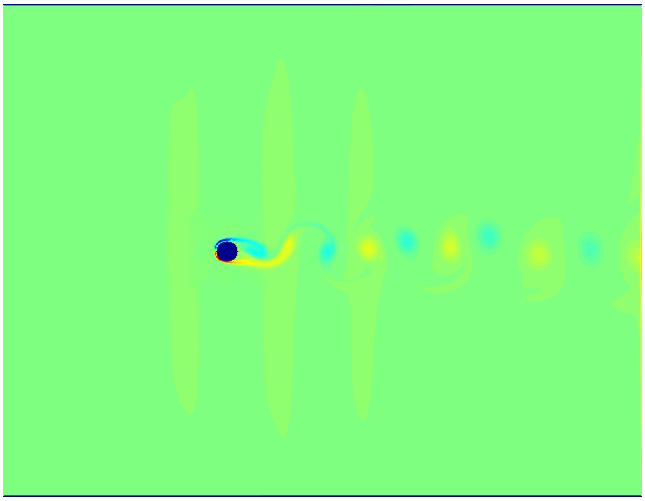

Figure 4.11: A snapshot of vorticity field at $Re = 300$ and $400th$ time step.

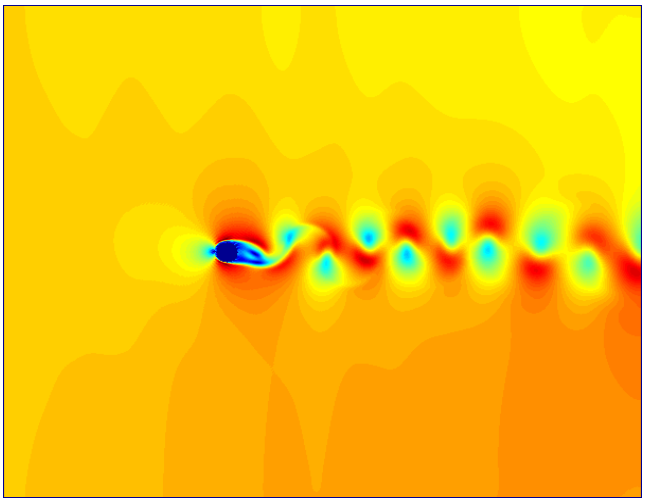

Figure 4.12: A snapshot of stream function at $Re = 300$ and $400th$ time step.

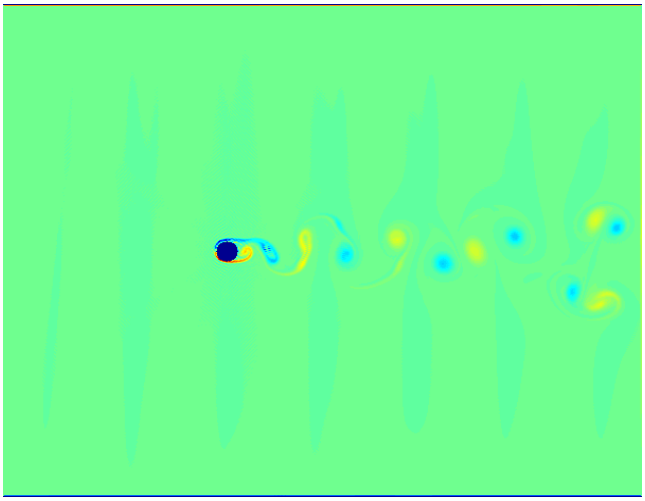

Figure 4.13: A snapshot of vorticity field at $Re = 1000$ and $400th$ time step.

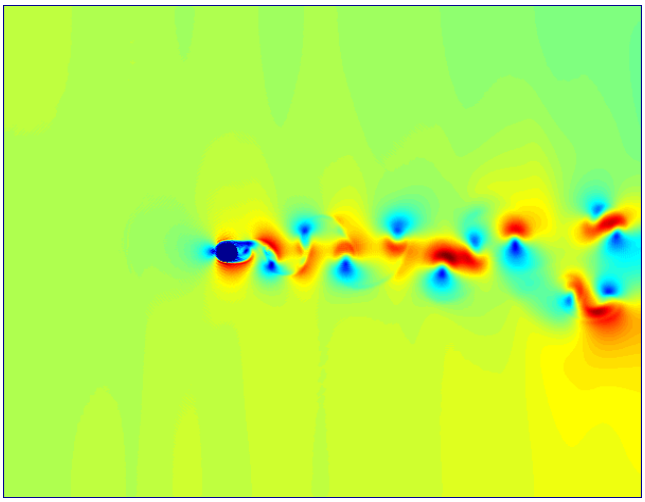

Figure 4.14: A snapshot of stream function at $Re = 1000$ and $400th$ time step.

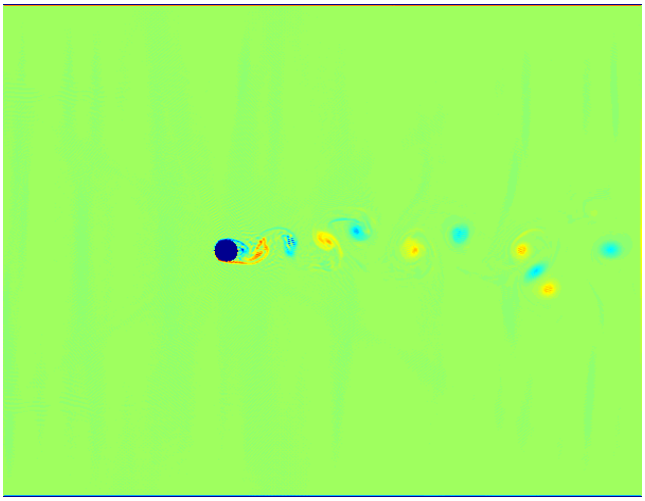

Figure 4.15: A snapshot of vorticity field at $Re = 3900$ and $400th$ time step.

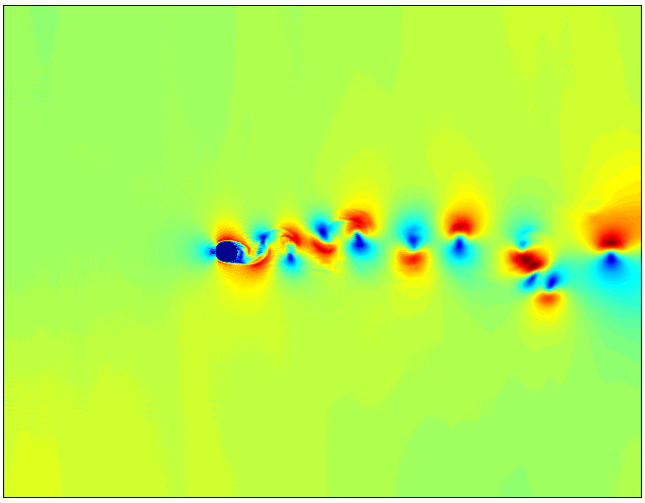

Figure 4.16: A snapshot of stream function at $Re = 3900$ and $400th$ time step.

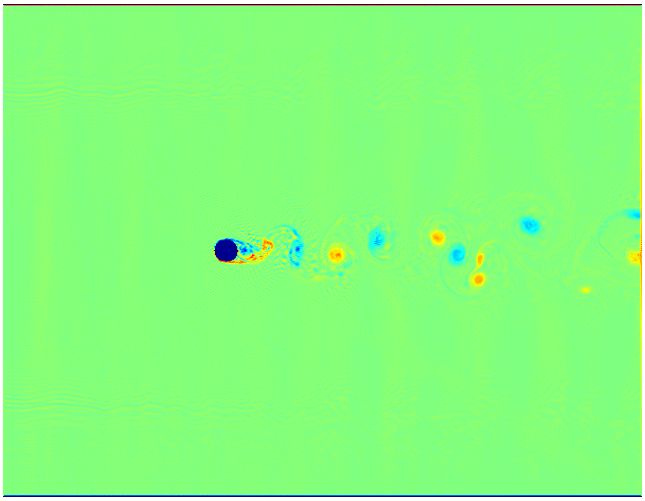

Figure 4.17: A snapshot of vorticity field at $Re = 10000$ and $400th$ time step.

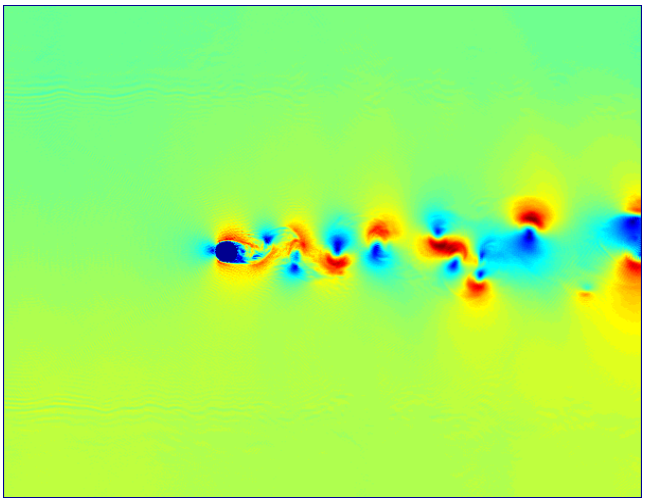

Figure 4.18: A snapshot of stream function at $Re = 10000$ and $400th$ time step.

4.4 Flow around a circular cylinder at Re = 3,900

Due to availability of experimental and numerical measurements of the mean flow fields in the wake of a circular cylinder at $Re = 3,900$, we have chosen this Reynolds number for the validation of our numerical model to capture turbulent phenomena behind cylinder wake.

Lourenco and Shih [60] performed experimental studies on the cylinder flow at $Re = 3,900$ using the Particle Image Velocimetry (PIV). In their studies, the velocity profiles were measured in the very near wake region ($x/D \leq 3$), i.e. within three diameter downstream in the wake region of the flow. Ong and Wallace [73] performed experimental studies for the same case using hot-wire probes. They measured the velocity profiles and the Reynolds stress distributions in the near wake region ($3 \leq Re \leq 10$). Both the experiments provide valuable data for the near-wake statistics.

First numerical study of the near wake region of the cylinder was conducted by Beaudan and Moin [8]. They performed the Large Eddy Simulations (LES) of flow past a circular cylinder at $Re = 3,900$. They solved the compressible Navier-Stokes equation on an O-grid with fifth order accurate and seventh order accurate upwind-biased schemes. Based on their calculations they concluded that the high order upwind scheme was highly dissipative in the wake and hence ill-suited for LES. Mittal and Moin [69] performed LES of the same case by solving the incompressible Navier Stokes equations on a C-grid using the central difference scheme of second order. They employed a Fourier-spectral method in the spanwise direction in conjunction with the periodic boundary conditions. Their results for the mean flow field did not differ much from the one of Beaudan and Moin, their power spectra in the near wake were in better agreement with the experiments.Kravchenko and Moin [54] found even better agreement for the spectra. They solved the incompressible equations with a

high order method based on B-splines on an O-grid with zonal refinement. Their simulations agreed well with the experimental data of Lourenco and Shih and Ong and Wallace [60, 73]. Also they emphasized on the influence of numerical resolution and the spanwise domain size of the three dimensional simulations. They found that inadequate grid resolution can cause early transition in the shear layers separating from the cylinder which leads to inaccurate predictions of the near-wake flow statistics.

Breuer [14] studied the numerical and modeling aspects of LES of the flow past a circular cylinder at $Re = 3,900$. He investigated five different discretization schemes and with dynamic and Smogorinsky subgrid-scale models. This work confirmed the earlier findings that central difference schemes are better suited than the higher order upwind schemes. In addition, he concluded that the dynamic model combined with central difference schemes yields the best results, which agree well with the experimental measurements. In each of the above case, the spanwise extent of the computational domain was πD.

Ma et al. [63] performed both DNS and LES calculations with a spectral finite element method, solving the incompressible equations in a box shaped domain. He showed the two converged states of the flow field in the very near wake exist, that are related to the shear layer transition and depend on the spanwise extent of the computational domain. Another DNS was carried out by Tremblay et al. [87] at Reynolds number of $3,900$. They also performed their simulations in a box shaped domain with spanwise extent of πD. They solved the incompressible equations with finite volume method and central difference on a cartesian grid. They also obtained a larger recirculation length than in the experiment of Lourenco and Shih [60], but nearly 20 percent shorter than that of Ma et al. [63] for the corresponding size. Hansen and Forsythe [35] performed DES simulations, using Cobalt, an unstructured

finite volume code to solve the problem of flow past a circular cylinder at $Re = 3,900$. They mainly studied the effects of grid resolution on the solution and the effects of using unstructured grids for turbulence resolving calculations. With sufficient grid resolution, grid independence was achieved in some of the variables examined and the global statistics of drag, recirculation zone length, and Strouhal number were well within the range of experimental uncertainty.

In present work, a comparison of the mean flowfield and the turbulence quantities in the wake region ($1.06 \leq x/D \leq 10$) with the experimental [60, 73] and numerical simulations [14, 87] have been carried out. Regarding our two dimensional simulations, we find excellent agreement with the experimental and numerical results in the wake region ($3 \leq x/D \leq 10$).

4.4.1 Mean flow statistics

The temporal mean of the streamwise and vertical velocity components are defined by

$$u = \langle U \rangle, \qquad v = \langle V \rangle, \tag{4.4.1}$$

where U and V are the instantaneous velocity components and $\langle . \rangle$ denote the time average of them. The streamwise and vertical velocities are normalized by the free-stream inlet velocity U_∞.

Figure (4.19) shows the mean centerline velocity of the flow compared with the experimental results [60, 73], LES [14] and the DNS [87]. Our data matches well with the experimental data of Ong and Wallace and numerical data of Tremblay in the region further downstream. In the recovery region ($2 \leq x/D \leq 4$), the discrepancies between experimental data and numerical data could be due to large scale phenomena in the spanwise direction. Vortex dislocations arise naturally in 3D wake at high

Reynolds numbers.

In Figures (4.20), (4.21) and (4.22), the vertical profiles of the streamwise velocity components at locations ranging from $x/D = 1.06$ TO $x/D = 10$ are plotted. There are deviations at the locations $1.54 \leq x/D \leq 3$. But at the remaining locations there is good agreement with the experimental and numerical data. This might be again due to the three dimensional effects.

Figures (4.23), (4.24) and (4.25) show the vertical profiles of the mean vertical velocity at the downstream locations. Our simulations agree well with the numerical data of Tremblay [87] except at few locations.

4.4.2 Turbulent flow statistics

The components of the Reynolds stress tensor are given by

$$u_i^* u_j^* = \langle U_i U_j \rangle - \langle U_i \rangle \langle U_j \rangle, \qquad i, j = 1, 2, \tag{4.4.2}$$

where subscripts 1 and 2 denote the x- and y-components respectively, i.e., $u_1^* = u^*$ and $u_2^* = v^*$. All the Reynolds stresses are normalized by the square of the inlet velocity.

Figures (4.26), (4.27) and (4.28) show the vertical profiles of the streamwise Reynolds stresses $(u^* u^*/U_\infty^2)$ at the downstream locations ranging from $x/D = 1.06$ to $x/D = 10$. Overall good agreement is found with both experimental and numerical data. A very good agreement with the experimental data of Ong and Wallace [73] is observed at location $x/D = 3$.

Figures (4.29), (4.30) and (4.31) present the vertical profiles of the vertical Reynolds stresses $(v^* v^*/U_\infty^2)$ at the locations described above. Again a good agreement is found with the experimental and numerical data. Surprisingly, our simulation is in very

good agreement with the experimental data of Lourenco and Shih [60] and Ong and Wallace [73] at locations $1.54 \leq x/D \leq 4$.

Figures (4.32), (4.33) and (4.34) show the vertical profiles of the Reynolds shear stresses (u^*v^*/U_∞^2) at the same locations as described above. Again, we find good agreement.

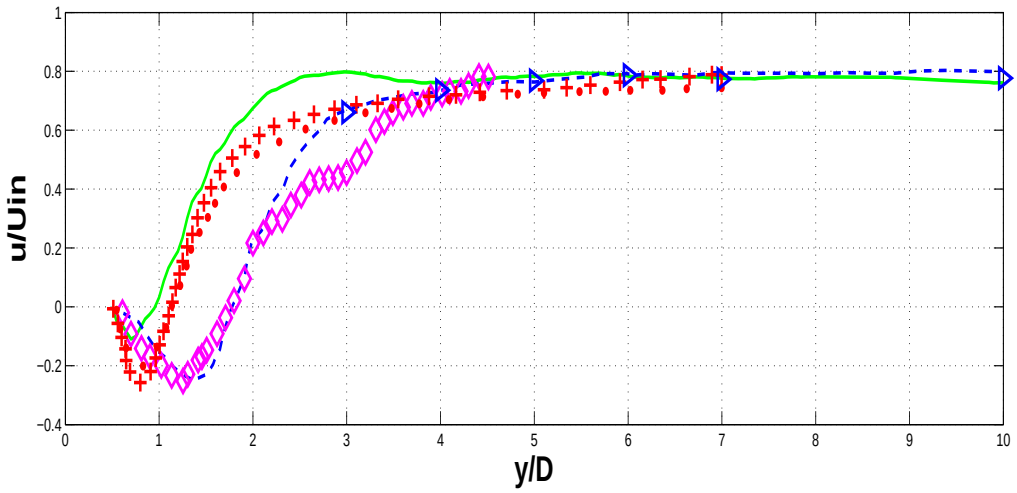

Figure 4.19: Mean streamwise velocity along the centerline of the cylinder. Present LBM with Ehrenfests' steps (green solid line); DNS Tremblay [87] (blue dashed line); Exp. Lourenco and Shih [60] (pink diamonds); Exp. Ong and Wallace [73] (blue triangles); Num. Breuer [14] (red dots) and Num. Flouos Smagorinsky model (red +).

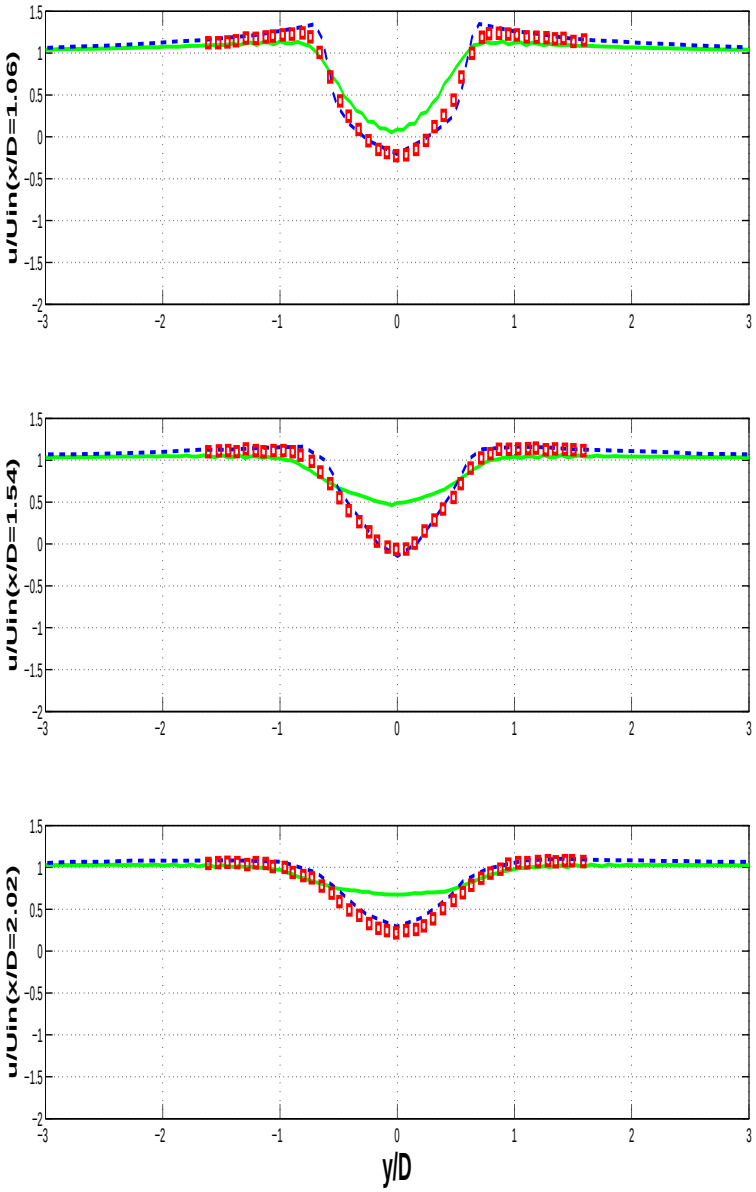

Figure 4.20: Vertical profiles of the mean streamwise velocity at x/D=1.06, 1.54 and 2.02. Present LBM with Ehrenfests' steps (green solid line); DNS Tremblay [87] (blue dashed line) and Exp. Lourenco and Shih [60] (red squares).

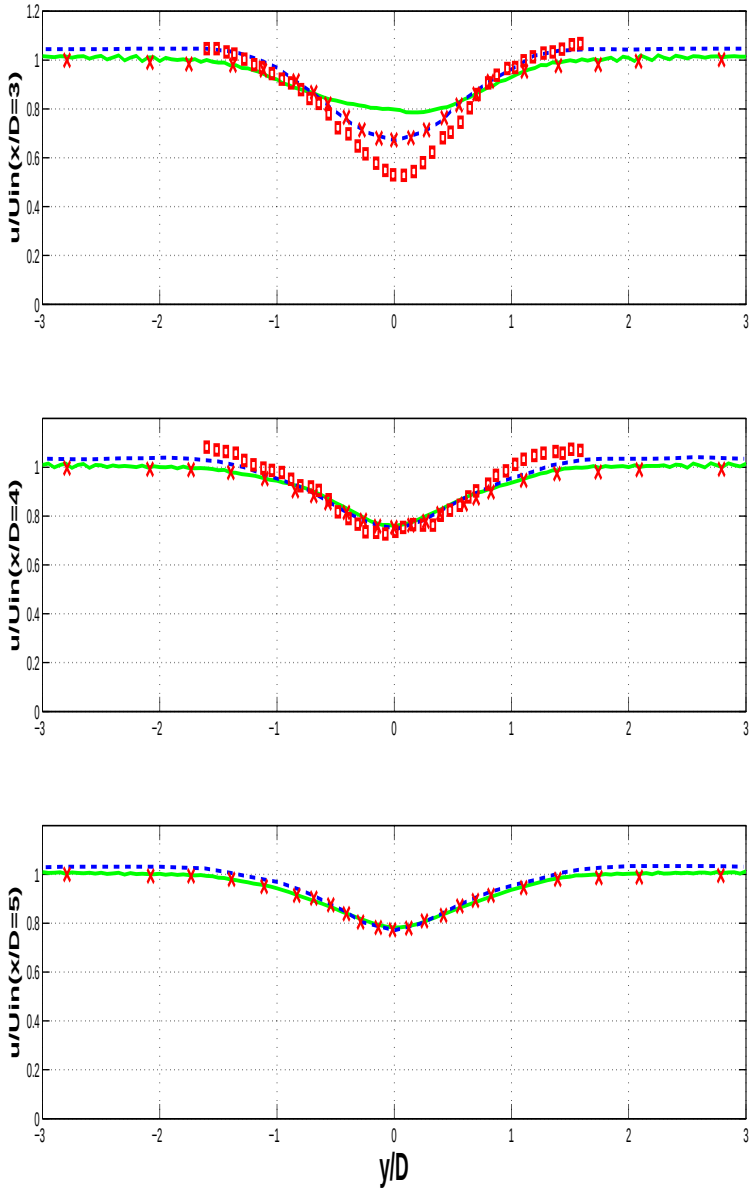

Figure 4.21: Vertical profiles of the mean streamwise velocity at x/D=3, 4 and 5. Present LBM with Ehrenfests' steps (green solid line); DNS Tremblay [87] (blue dashed line); Exp. Ong and Wallace [73] (red crosses) and Exp. Lourenco and Shih [60] (red squares).

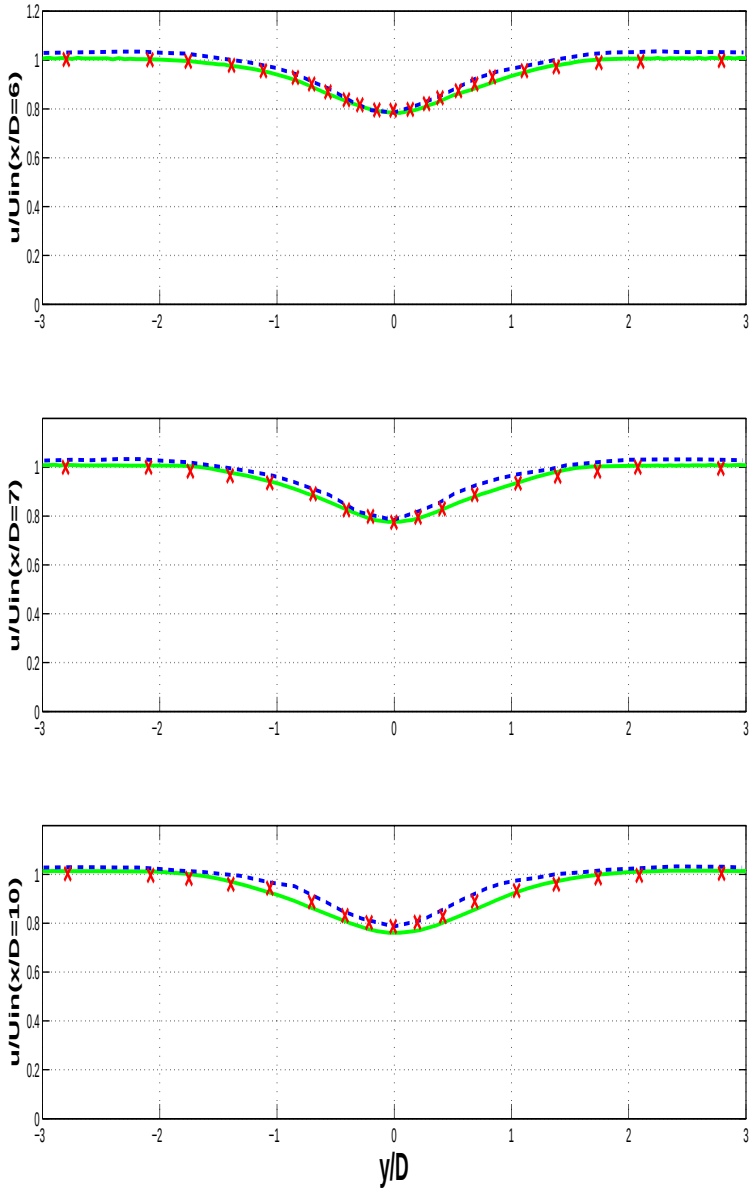

Figure 4.22: Vertical profiles of the mean streamwise velocity at x/D=6, 7 and 10. Present LBM with Ehrenfests' steps (green solid line); DNS Tremblay [87] (blue dashed line); Exp. Ong and Wallace [73] (red crosses).

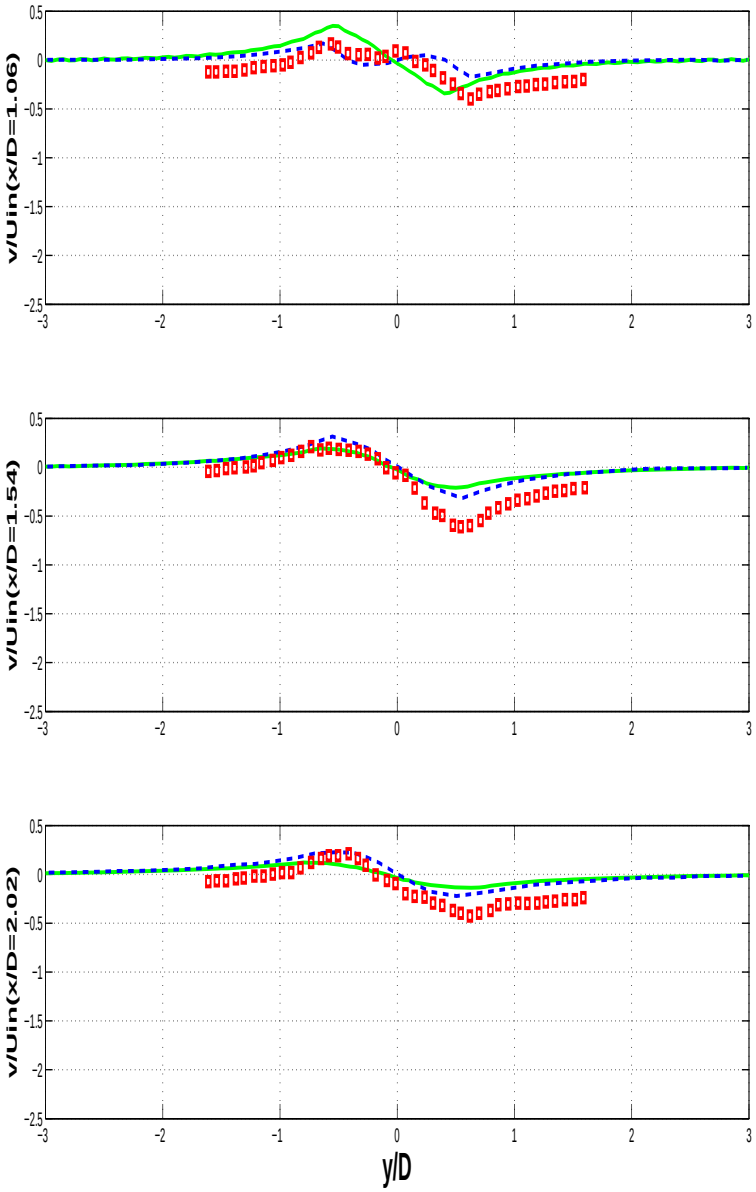

Figure 4.23: Vertical profiles of the mean vertical velocity at x/D=1.06, 1.54 and 2.02. Present LBM with Ehrenfests' steps (green solid line); DNS Tremblay [87] (blue dashed line); and Exp. Lourenco and Shih [60] (red squares).

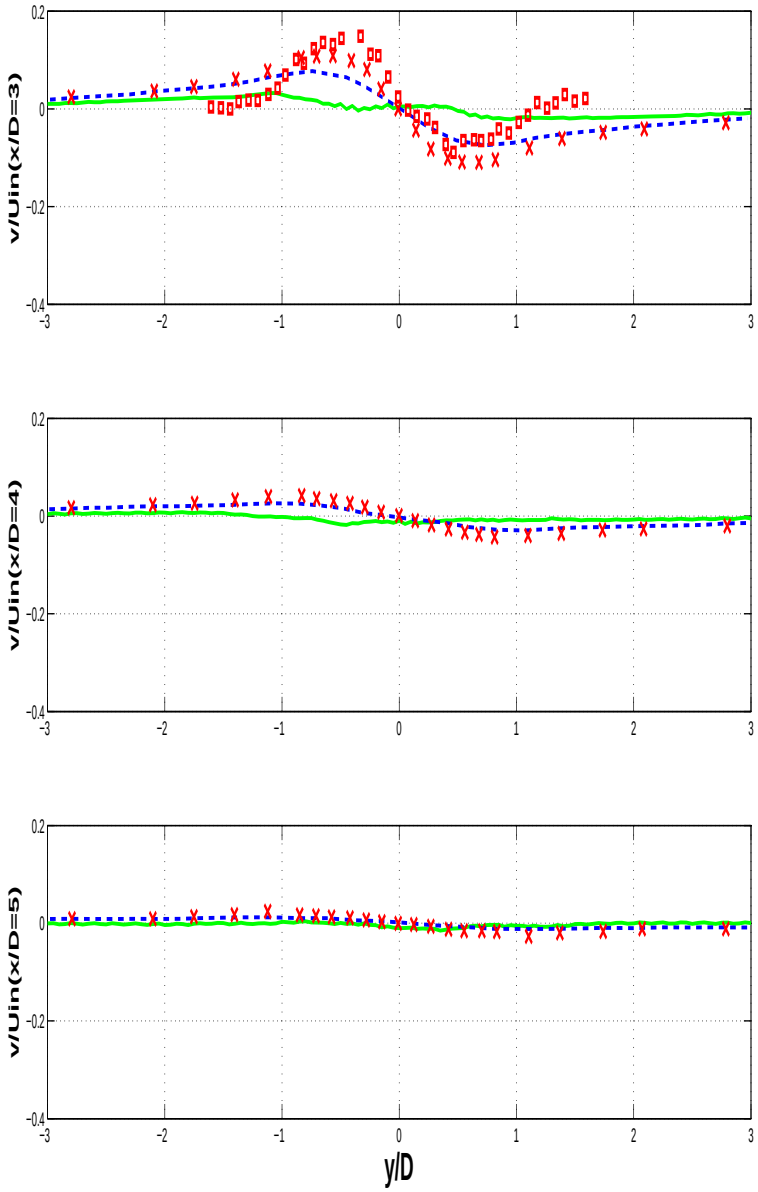

Figure 4.24: Vertical profiles of the mean vertical velocity at x/D=3, 4 and 5. Present LBM with Ehrenfests' steps (green solid line); DNS Tremblay [87] (blue dashed line); Exp. Ong and Wallace [73] (red crosses) and Exp. Lourenco and Shih [60] (red squares).

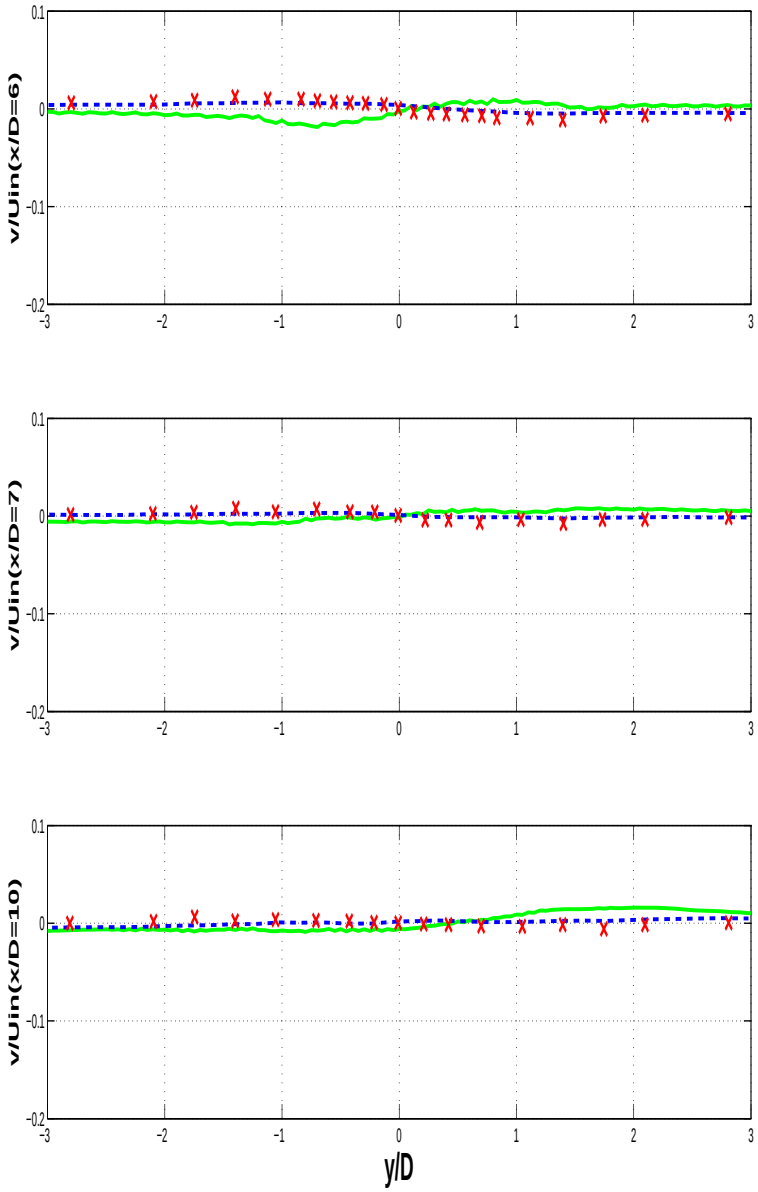

Figure 4.25: Vertical profiles of the mean vertical velocity at x/D=6, 7 and 10. Present LBM with Ehrenfests' steps (green solid line); DNS Tremblay [87] (blue dashed line); Exp. Ong and Wallace [73] (red crosses).

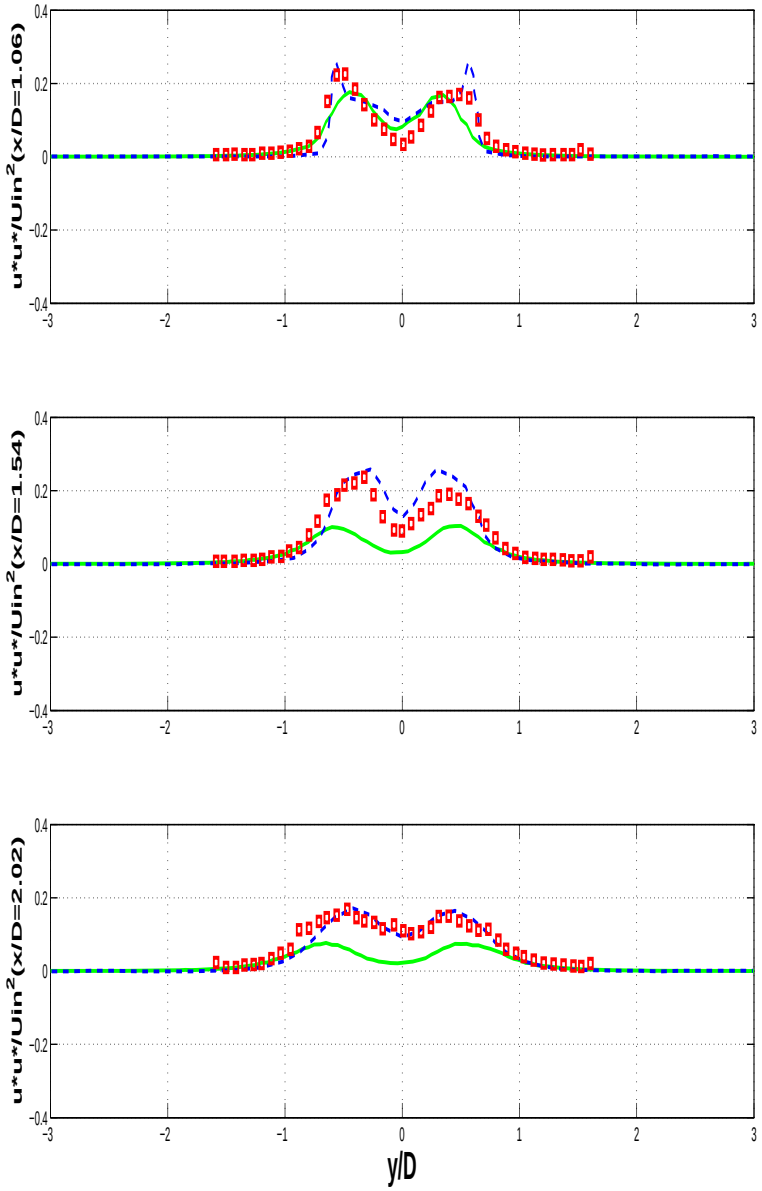

Figure 4.26: Vertical profiles of the variance of the streamwise velocity at x/D=1.06, 1.54 and 2.02. Present LBM with Ehrenfests' steps (green solid line); DNS Tremblay [87] (blue dashed line); Exp. Lourenco and Shih [60] (red squares).

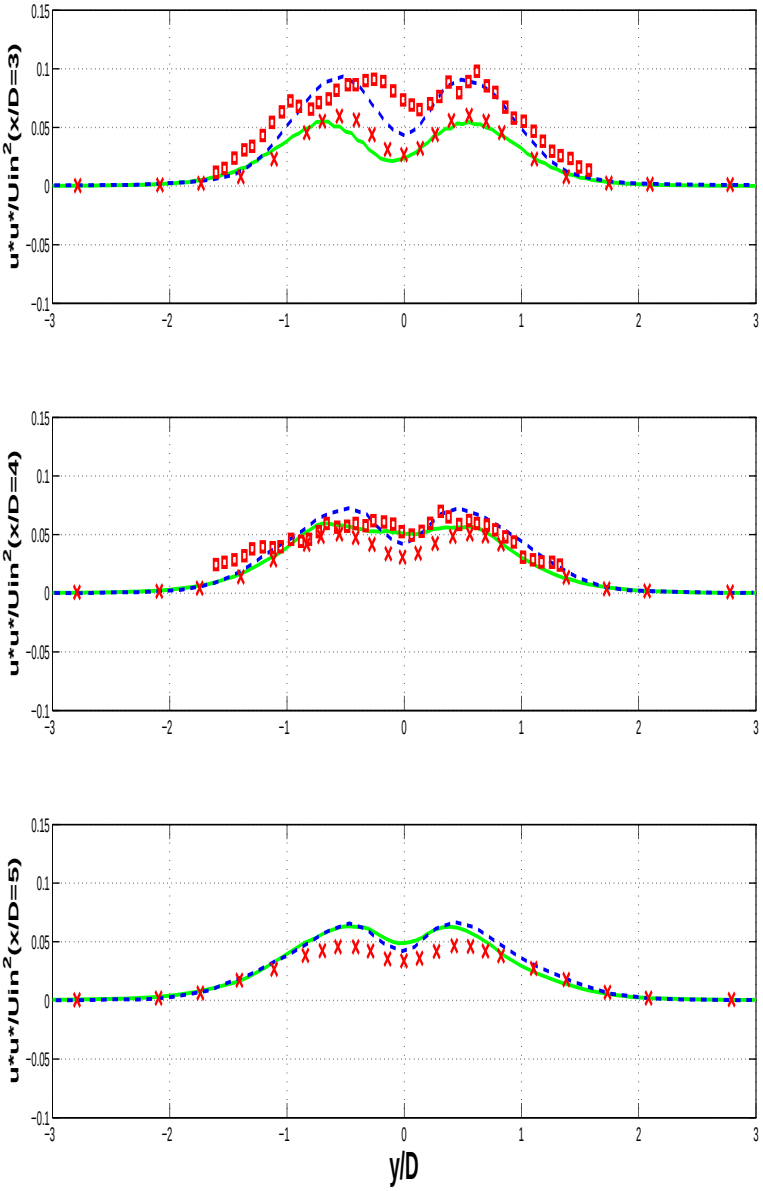

Figure 4.27: Vertical profiles of the variance of the streamwise velocity at x/D=3, 4 and 5. Present LBM with Ehrenfests' steps (green solid line); DNS Tremblay [87] (blue dashed line); Exp. Ong and Wallace [73] (red crosses) and Lourenco and Shih [60] (red squares).

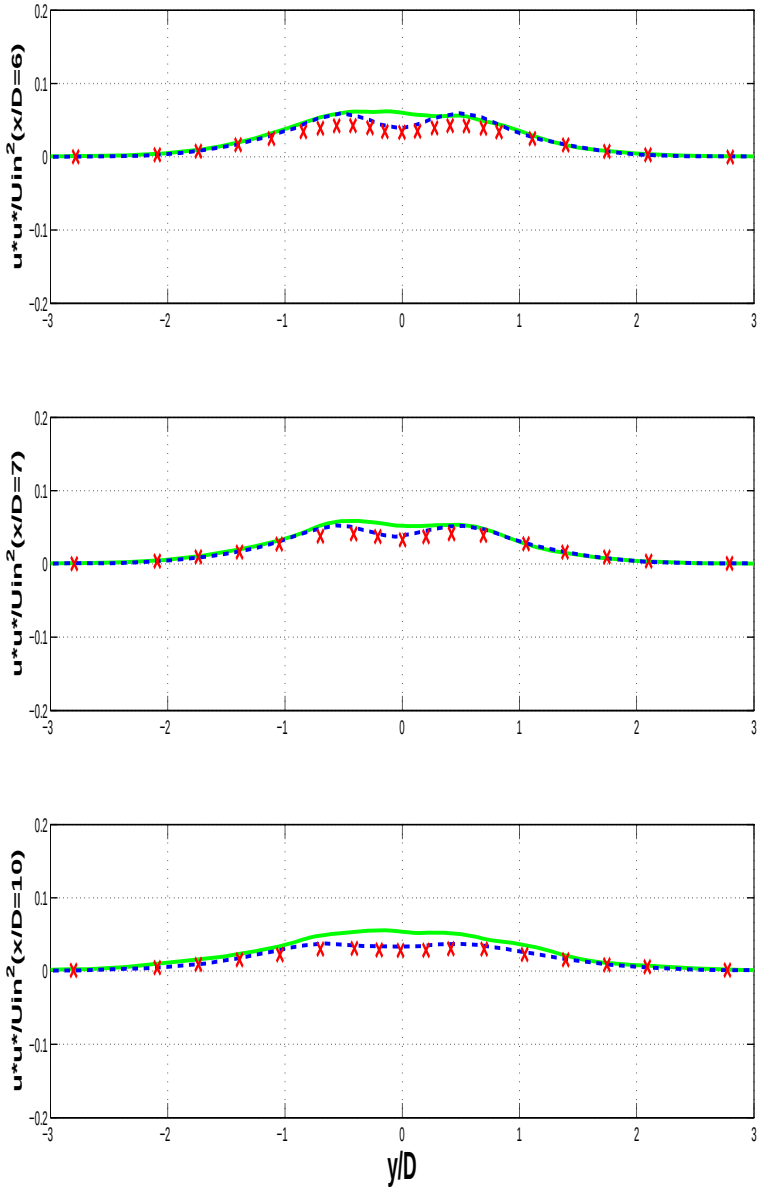

Figure 4.28: Vertical profiles of the variance of the streamwise velocity at x/D=6, 7 and 10. Present LBM with Ehrenfests' steps (green solid line); DNS Tremblay [87] (blue dashed line); Exp. Ong and Wallace [73] (red crosses).

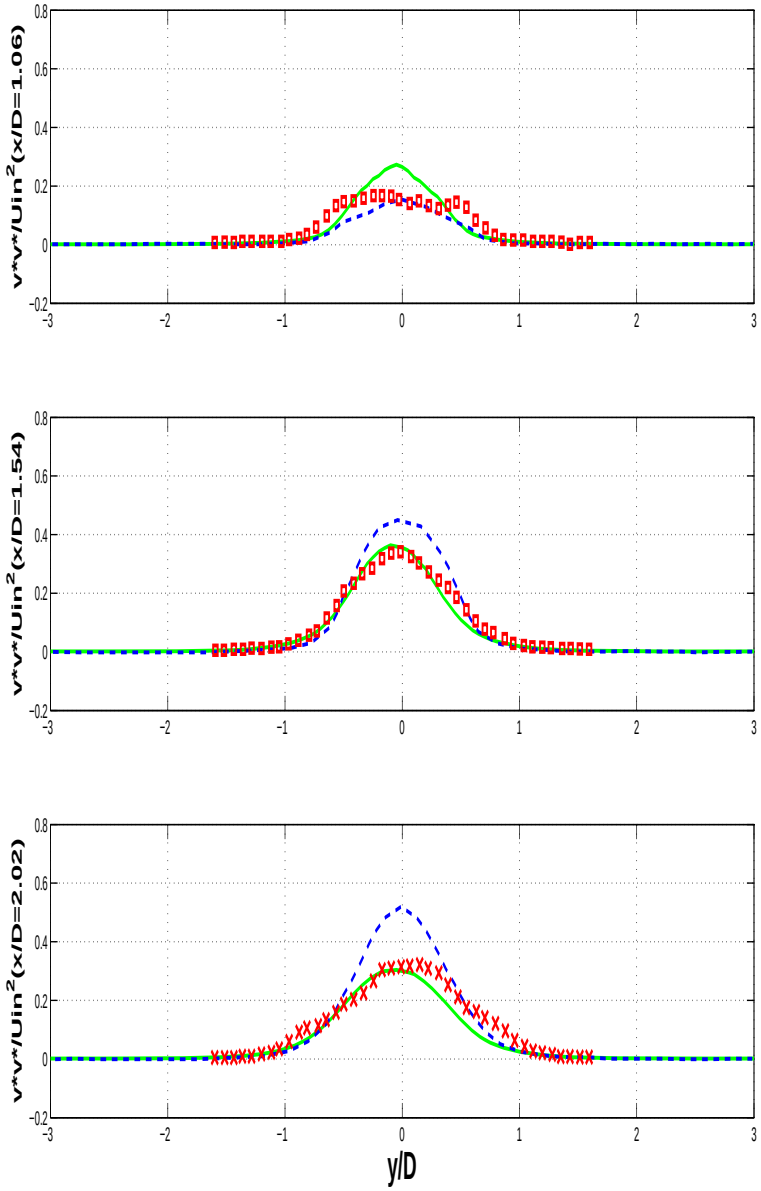

Figure 4.29: Vertical profiles of the variance of the vertical velocity at x/D=1.06, 1.54 and 2.02. Present LBM with Ehrenfests' steps (green solid line); DNS Tremblay [87] (blue dashed line); Exp. Ong and Wallace [73] (red crosses) and Lourenco and Shih [60] (red squares).

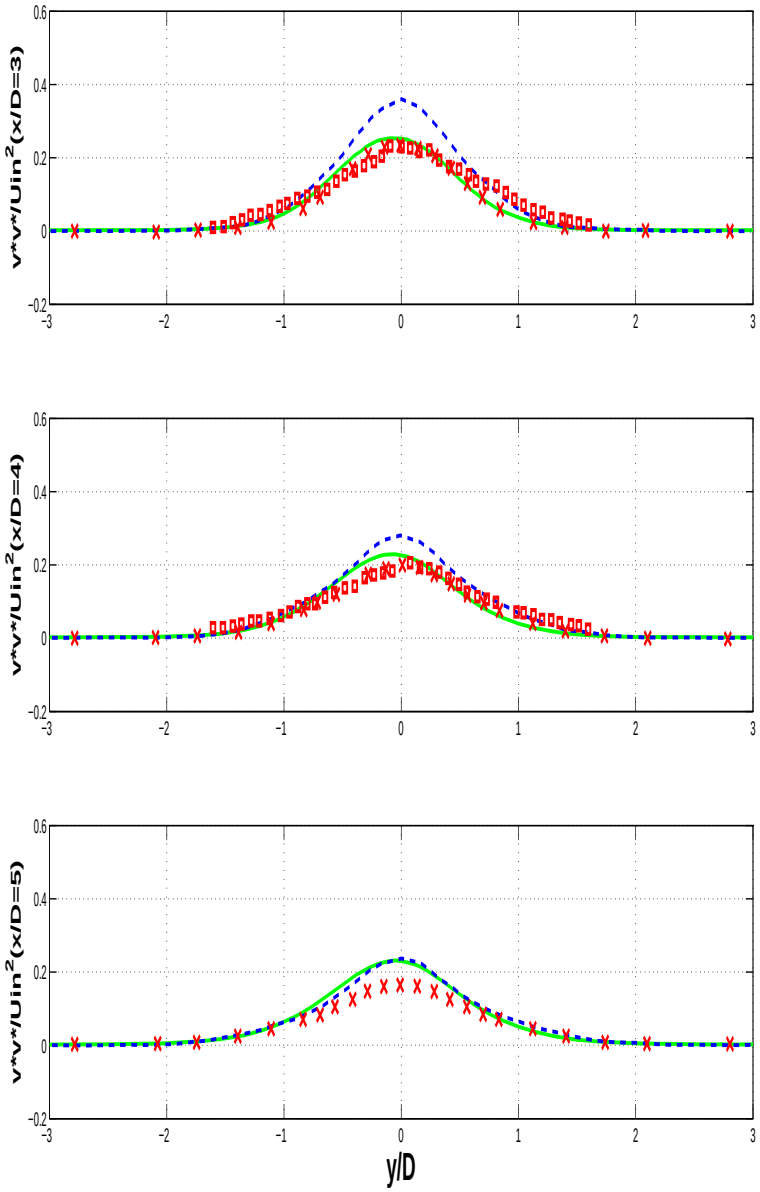

Figure 4.30: Vertical profiles of the variance of the vertical velocity at x/D=3, 4 and 5. Present LBM with Ehrenfests' steps (green solid line); DNS Tremblay [87] (blue dashed line); Exp. Ong and Wallace [73] (red crosses) and Lourenco and Shih [60] (red squares).

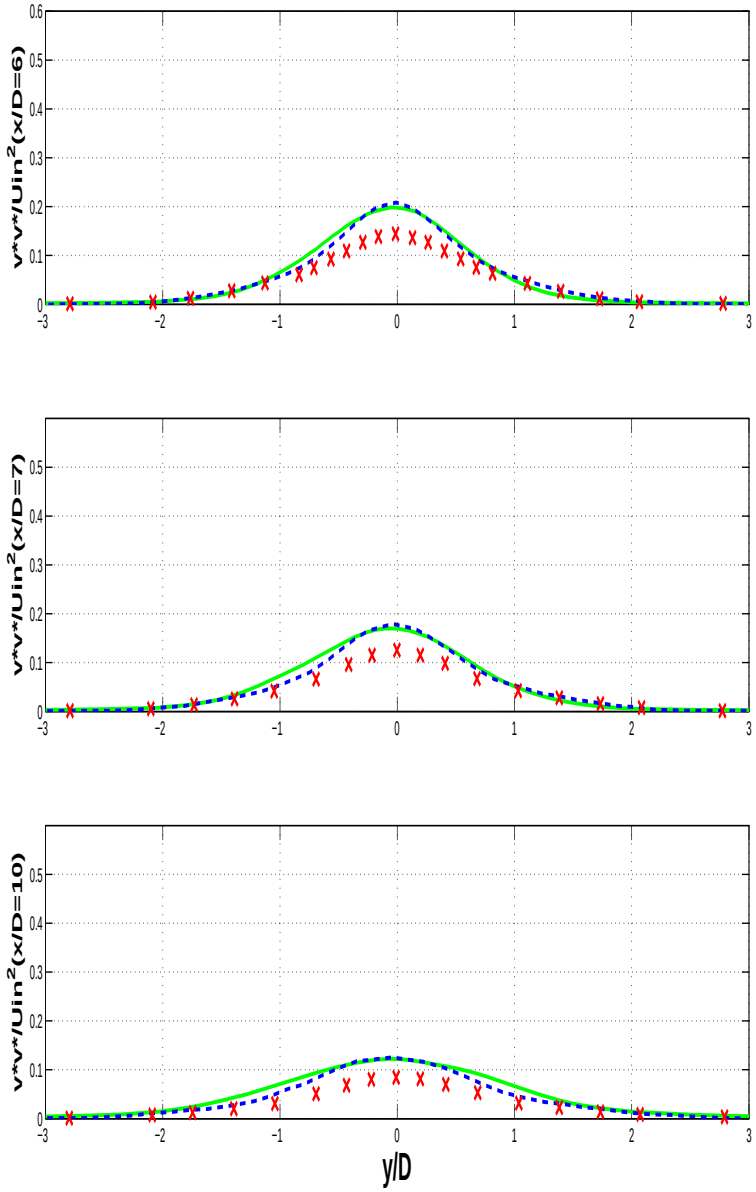

Figure 4.31: Vertical profiles of the variance of the vertical velocity x/D=6, 7 and 10. Present LBM with Ehrenfests' steps (green solid line); DNS Tremblay [87] (blue dashed line); Exp. Ong and Wallace [73] (red crosses).

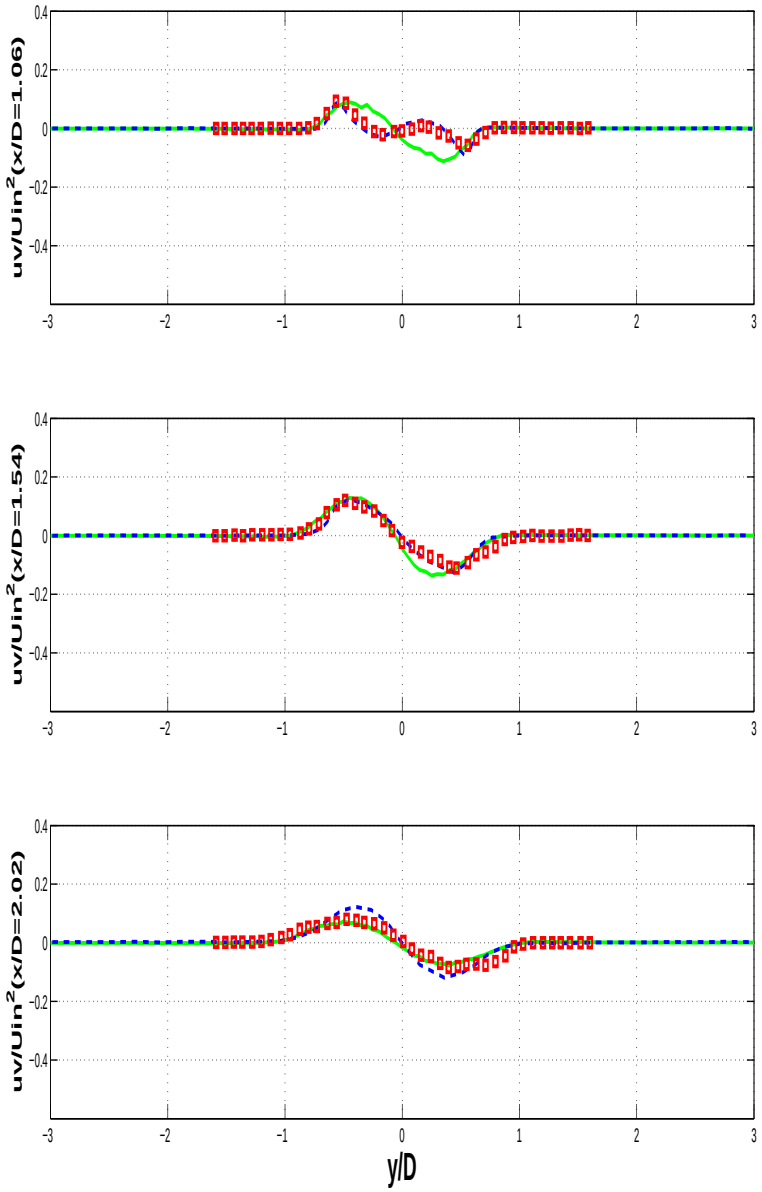

Figure 4.32: Vertical profiles of the Reynolds shear stress at x/D=1.06, 1.54 and 2.02. Present LBM with Ehrenfests' steps (green solid line); DNS Tremblay [87] (blue dashed line); and Exp. Lourenco and Shih [60] (red squares).

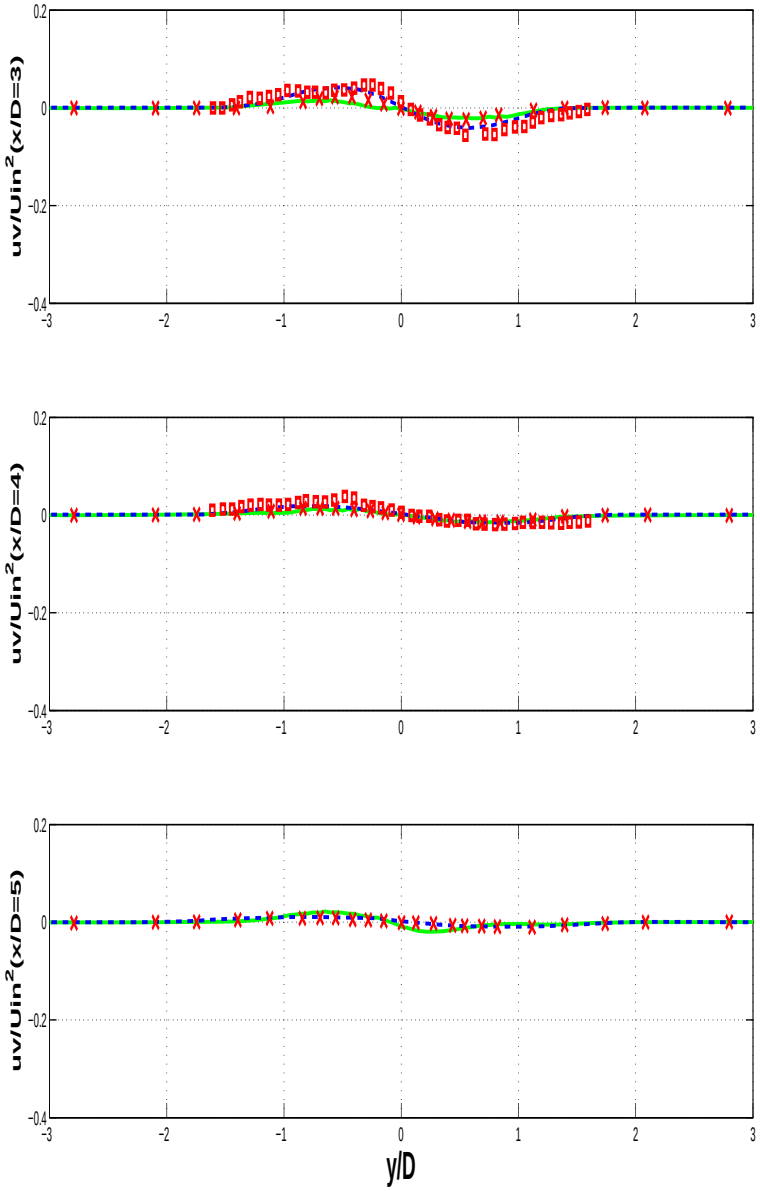

Figure 4.33: Vertical profiles of the Reynolds shear stress at x/D=3, 4 and 5. Present LBM with Ehrenfests' steps (green solid line); DNS Tremblay [87] (blue dashed line); Exp. Ong and Wallace [73] (red crosses) and Exp. Lourenco and Shih [60] (red squares).

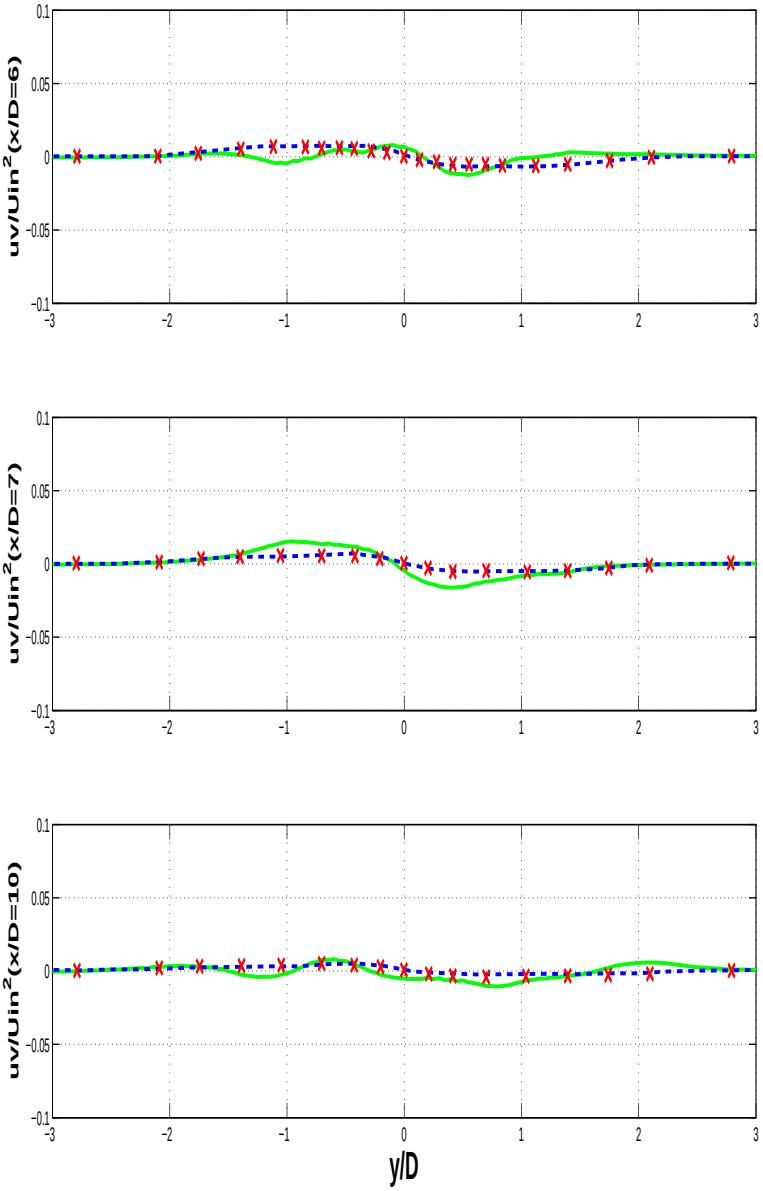

Figure 4.34: Vertical profiles of the Reynolds shear stress at x/D=6, 7 and 10. Present LBM with Ehrenfests' steps (green solid line); DNS Tremblay [87] (blue dashed line); Exp. Ong and Wallace [73] (red crosses).

Chapter 5

Flow Around Elliptic Cylinder and Airfoil

In this chapter we present two more examples for the validity of our model. Flows around elliptical cylinders and a NASA0015 airfoil are simulated for the Reynolds numbers ranging from 500 to 2000.

5.1 Flow around elliptical cylinder

Flow around elliptical cylinders is another prototype flow over a range of bluff bodies since the geometry of this flow allows one to study the effect of both thickness ratio and angle of attack on the flow field. The study of this flow can provide valuable insight into the phenomenon of unsteady flow separation and the structure of bluff body wakes.

The simulation around elliptical cylinders of aspect ratios $AR = 1/2$ and $AR = 2$ has been performed using the LBM with Ehrenfests for Reynolds numbers of 525 and $1,000$. The Reynolds number is defined by $Re = U_\infty D/\nu$ where U_∞ is the inlet

velocity and D is the vertical length of the cylinder. That is for the cylinder of aspect ratio 1/2, D is the minor axis and for the cylinder of aspect ratio 2, D is the length of major axis. Computational set up for the flow around elliptical cylinder is same as for the flow around circular cylinder. The stream functions and vorticity contours of these simulations are shown in Figures (5.1) to (5.8).

The results are compared with direct numerical simulation (DNS) data of Mittal and Balachandar [70] and Ingber [41]. Mittal and Balachandar used direct numerical simulation (DNS) and found that for the Reynolds number $Re = 1,000$, the two dimensional (DNS) predict the Strouhal number $St = 0.20$. The current simulation predicted the Strouhal number $St = 0.1952$ for Reynolds number $Re = 1,000$. For $Re = 525$, two dimensional simulations of Mittal [70] predicted the Strouhal number at $St = 0.21$ and for three dimensional simulations it is $St = 0.24$. Our two dimensional predicted value of Strouhal number is exactly same as that of three dimensional simulations of Mittal, that is, 0.24.

For $Re = 525$, the drag coefficient predicted by Mittal [70] is $C_D = 0.78$. We have found it as 0.79 for the same Reynolds number. For $Re = 1,000$ two dimensional simulations of Mittal reported this value as $C_D = 0.61$. Our value is $C_D = 0.4678$.

5.2 Flow around NASA0015 foil

Third example for the validation of our model,we have selected flow around a symmetric NASA0015 airfoil at zero degree angle of attack. For this flow, the computational domain of size 601×78 lattice nodes is selected. The chord length of airfoil is set at length of 20 lattice nodes. The other computational details are same as those for the flow around circular cylinder.

The simulations are performed for a series of Reynolds number $Re = 500, 1000, 1500,$ 2000. The vorticity contours and stream function snapshots for $Re = 2000$ are shown in Figures (5.9) and (5.10). Simulations are carried out for 500 iterations. Results are compared with PowerFlow simulations for the LBM of Lockard [59] and multi-block LBM scheme of Yu [94, 95]. Both simulations are for the flow around NASA0012 airfoil. So the drag coefficient of their simulations is slightly less than our simulation of NASA0015 airfoil.

For $Re = 500$, Yu [94] found drag coefficient $C_D = 0.1762$, while Lockard [59] reported it as $C_D = 0.17618$ using $CFL3D$ solver and found $C_D = 0.171721$ using PowerFlow simulation. We have found drag coefficient as $C_D = 0.1809$ for Reynolds number $Re = 500$. For Reynolds number $Re = 2000$, the value of drag coefficient is $C_D = 0.2552$.

Considering a small and underresolved computational domain, the present simulation results are in good agreement with other numerical schemes like commercial software PowerFlow.

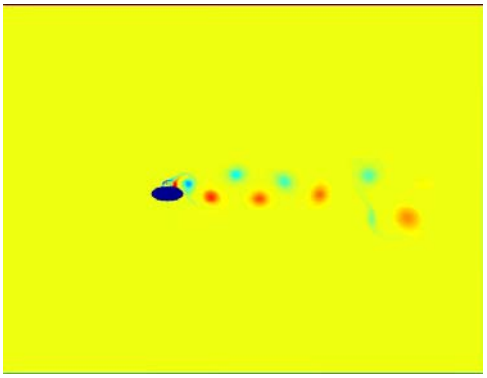

Figure 5.1: A snapshot of vorticity field in elliptic cylinder wake at $Re = 525$ and AR=1/2 and $400th$ time step.

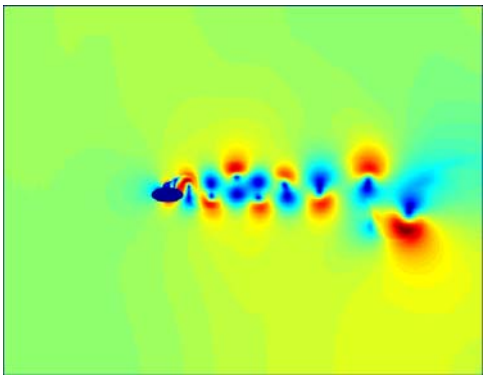

Figure 5.2: A snapshot of stream function in elliptic cylinder wake at $Re = 525$ and AR=1/2 and $400th$ time step.

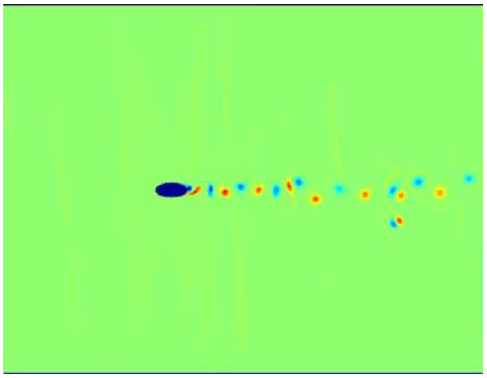

Figure 5.3: A snapshot of vorticity field in elliptic cylinder wake at $Re = 1000$ and AR=1/2 and $400th$ time step.

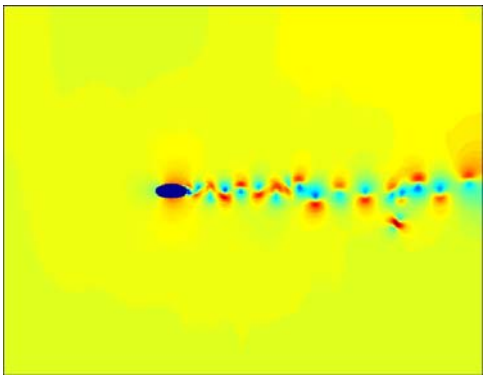

Figure 5.4: A snapshot of stream function in elliptic cylinder wake at $Re = 1000$ and AR=1/2 and $400th$ time step.

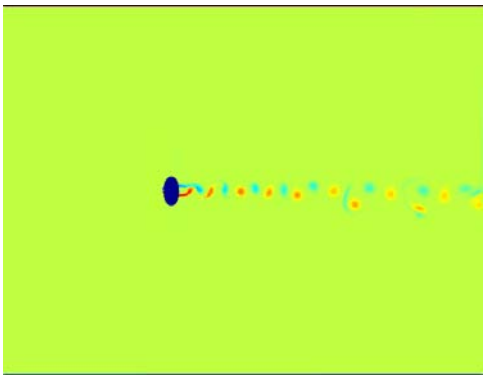

Figure 5.5: A snapshot of vorticity field in elliptic cylinder wake at $Re = 525$ and AR=2 and $400th$ time step.

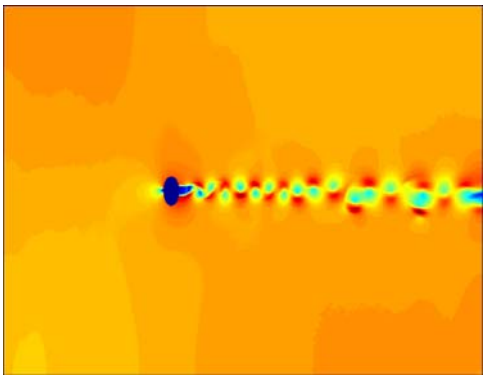

Figure 5.6: A snapshot of stream function in elliptic cylinder wake at $Re = 525$ and AR=2 and $400th$ time step.

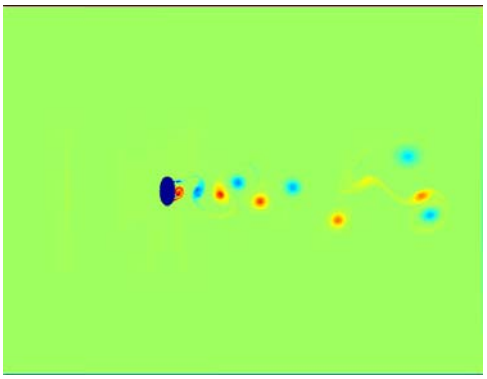

Figure 5.7: A snapshot of vorticity field in elliptic cylinder wake at $Re = 1000$ and AR=2 and $400th$ time step.

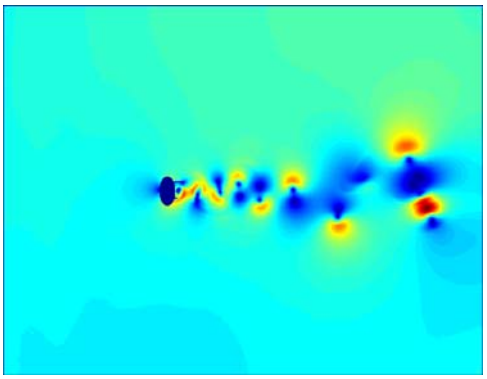

Figure 5.8: A snapshot of stream function in elliptic cylinder wake at $Re = 1000$ and AR=2 and $400th$ time step.

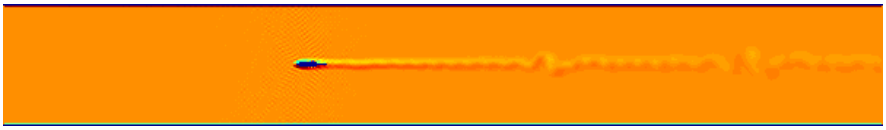

Figure 5.9: A snapshot of vorticity field in NASA0015 airfoil wake at $Re = 2000$ and $400th$ time step.

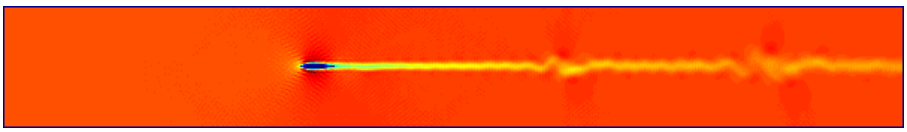

Figure 5.10: A snapshot of stream function in NASA0015 airfoil wake at $Re = 2000$ and $400th$ time step.

Chapter 6

Conclusion and Future Work

The work carried out in this thesis has proved the LBM with Ehrenfets' steps as a reliable turbulence model for the two dimensional simulation of flow around curved bluff bodies. The author has learned proper modelling skills for the simulation of flow around curved bluff bodies. A good practice on working with different boundary conditions in two dimensions has provided a confidence for future simulations in three dimension. In this chapter some findings and achievements on the study of the flow around curved bluff bodies, with some suggestions and recommendations on the future work upon the completion of the thesis are presented.

6.1 Conclusion

The aims and objectives set for the present work are achieved in this thesis. All simulations carried out using the LBM with Ehrenfests' steps has provided the necessary skills and knowledge for the investigation of flows around curved bluff bodies.

Despite the fact that an underresolved simulation i.e., the number of grid points used are of $O(10^5)$ and without any explicit sub-grid scale model, we have shown

that the LBM with Ehrenfests' steps can stabilize the fluid simulation past a circular cylinder for very high Reynolds number up to $Re = 20,000$. This method can quantitatively capture the Strouhal-Reynolds number relationship for this high Reynolds number. At $Re = 20,000$, the value of kinematic viscosity attained is $\nu = 5 \times 10^{-5}$. Above this Reynolds number, the errors from the boundary corrupted the simulation. Ehrenfests' steps introduce additional dissipation locally, on the base of pointwise analysis of nonequilibrium entropy. Due to this pointwise nature, this scheme does not introduce any nonisotropic effects. In order to preserve the second-order accuracy of the LBM, it is recommended that Ehrefests' steps should be performed on a small number of lattice sites with highest $\Delta S > \delta$. This number should be around $O(Nh/L)$, where L is the characteristic length of the flow (like diameter in case of flow around circular cylinder), N is the total number of sites in the domain and h is the lattice step size. If there are only k sites with $\Delta S > \delta$ are needed then this require a computational cost of $O(kN)$. We have observed in our numerical experiments that even a small share of these steps have improved the stability.

The results for the simulation of the flow around a circular cylinder using the LBM with Ehrenfests' regularization has been found satisfactory. This model predicted the vortex shedding phenomenon around a circular cylinder successfully. The Strouhal-Reynolds number relationship (see Section(4.3.1)) captured by our model has been found very close to the experimental results. Although the estimate of Strouhal number is slightly overestimated, yet it provides an asymptotic value of Strouhal number for large Reynolds numbers. In Section (4.3.2), we have computed the drag coefficient for low to high Reynolds numbers and the results compared with the experimental curve for the drag coefficient [80] show very good agreement. This is remarkable achievement considering that our two dimensional model is predicting

three dimensional turbulent flow parameters in good agreement.

To further investigate the turbulent phenomena in cylinder wakes, a comparative study with the experimental work at Reynolds number of $3,900$ shows good agreement. The vertical profiles of the streamwise and spanwise velocity components in the wake regions of the flow have been well predicted for the flow around a circular cylinder. The results for the turbulent flow statistics such as Reynolds normal and shear stresses are found close to the experimental findings of Lourenco and Shih [60] and Ong and Wallace [73] and three dimensional numerical findings of Tremblay [87]. Again considering two dimensional modelling, this is remarkable.

In Chapter 5, the validation of the model for the turbulent flows around airfoils and elliptic cylinders is observed. For elliptic cylinders of different aspect ratios, the prediction flow parameters such as Strouhal number and drag and lift coefficient found in good agreement with other numerical results. For NASA0015 airfoil, the drag and lift coefficients for Reynolds number of $5,00$ are found well in agreement in comparison with the numerical findings using PowerFlow [59].

6.2 Future work

In this section some recommendations for further research 0n the work performed in this thesis are described.

Although the LBM with Ehrenfets' steps have provided good results for the stable simulations of flows around bluff bodies, yet further detailed study using three-dimensional models are needed to check the accuracy of the method for $Re \approx O(10000)$. As we know that, the flow around circular cylinder is two-dimensional only when $Re < 200$. Beyond this Reynolds number, but less than $Re = 3 \times 10^5$ the wake

of the cylinder becomes fully turbulent.

This thesis covers the two-dimensional simulation of flows around bluff bodies for Reynolds numbers up to $20,000$. Three dimensional effects start occurring after $Re > 200$. To capture real physical phenomena and go beyond Reynolds number of $20,000$, three-dimensional efficiency of the modell is required.

Bibliography

[1] D.J. Acheson: *Elementary Fluid Dynamics*. Oxford University Press, 1990.

[2] S. Ansumali, I.V. Karlin: Stabilization of the lattice Boltzmann method by the H theorem: A numerical test, Physical Review E **62(6)**, 2000, 7999–8003.

[3] S. Ansumali, I.V. Karlin: Single relaxation time model for entropic lattice Boltzmann methods, Physical Review E **65**, 2002, 056312.

[4] S. Ansumali, I.V. Karlin: Entropy function approach to the lattice Boltzmann methods, J. Stat. Phys. **107**, 2002, 291–308.

[5] S. Ansumali, I.V. Karlin, H.C. Öttinger: Minimal entropic kinetic models for simulating hydrodynamics, Europhys. Lett. **63**, 2003, 798–804.

[6] S. Ansumali, S.S. Chikatamarla, C.E. Frouzakis, K. Boulouchos: Entropic lattice Boltzmann simulation of flow past square cylinder, International Journal of Modern Physics C **15**, 2004, 435–455.

[7] D. Barkley, R.D. Henderson: Three-dimensional Floquet stability analysis of the wake of a circular cylinder, J. Fluid Mech. **322**, 1996, 215–241.

[8] P. Beaudan and P. Moin: Numerical experiments on the flow past a circular cylinder at sub-critical Reynolds number. Report No. TF-62 Thermosciences Division, Department of Mechanical Engineering, Stanford University, 1994.

[9] R. Benzi, S. Succi: Two-dimensional turbulence with the lattice Boltzmann equation, J. Phys. A **23**, 1990, L1–L5.

[10] R. Benzi, S. Succi, M. Vergassola: The lattice Boltzmann equation: theory and applications, Phys. Rep. **222(3)**, 1992, 145–197.

[11] P.L. Bhatnagar, E.P. Gross, M. Krook: A model for collision processes in gases. I: small amplitude processes in charged and neutral one-component system, Phys. Rev. **94(3)**, 1954, 511–525.

[12] M.S. Bloor: The transition to turbulence in the wake of a circular cylinder, Journal of Fluid Mechanics **19**, 1964, 290–304.

[13] B.M. Boghosian, J. Yepez, P.V. Coveney, A. Wagner: Entropic lattice Boltzmann Methods, Proc. R. Soc. London, Ser. A **457**, 2001, 717.

[14] M. Breuer: Large eddy simulation of the sub-critical flow past a circular cylinder: numerical and modeling aspects, International Journal for Numerical Methods in Fluids **28,(9)**, 1998, 1281–1302.

[15] M. Braza, P. Chassaing, H.H. Minh: Numerical study and physical analysis of the pressure and velocity fields in the near wake of a circular cylinder, J. Fluid Mech. **165**, 1986, 70–130.

[16] M. Braza, P. Chassaing, H.H. Minh: Prediction of large scales transition features in the wake of a circular cylinder, Phys. Fluids **A2**, 1990, 1461–1471.

[17] R. Brownlee, A.N. Gorban, J. Levesely: Stabilization of the lattice-Boltzmann method using the Ehrenfests' coarse-graining, Phs. Rev. E **74**, 2006, 037703.

[18] R. Brownlee, A.N. Gorban, J. Levesely: Stability and stabilization of the lattice Boltzmann method, Phys. Rev. E **75**, 2007, 036711.

[19] R. Brownlee, A.N. Gorban, J. Levesely: Stable simulation of fluid flow with high-Reynolds number using Ehrenfests' steps, Numerical Algorithms. **45**, 2007, 389–408.

[20] R. Brownlee, A.N. Gorban, J. Levesely: Nonequilibrium entropy limiters in lattice Boltzmann method, Physica A **387(2-3)**, 2008, 385–406.

[21] S.S. Chikatamarla, I.V. Karlin: Entropy and Galilean Invariance of Lattice Boltzmann Theories, Phys. Rev. Lett. **97**, 190601, 2006, 1–4.

[22] H. Chen, S. Chen, W.H. Matthaeus: Recovery of the Navier-Stokes equations using a lattice-gas Boltzmann method, Phys. Rev. A **45(8)**, 1992, R5339–R5342.

[23] S. Chen, G.D. Doolen: Lattice Boltzmann method for fluid flows, Annu. Rev. Fluid Mech. **30**, 1998, 329–364.

[24] M.-H. Chou and W. Huang: Numerical study of high-Reynolds-number flow past a bluff object, International Journal for Numerical Methods in Fluids **23**, 1996, 711–732.

[25] D. d'Humières, P. Lallemand, U. Frisch: Lattice gas model for 3D hydrodynamics, Europhys. Lett. **2(4)**, 1986, 291–297.

[26] D. d'Humières: Generalized lattice Boltzmann equations, in: B.D. Shizgal, D.P. Weaver (Eds.), Rarefied Gas Dynamics: Theory and Simulations. Prog. Astonaut Aeronaut **159**, 1992, 450–458.

[27] P. Ehrenfest, T. Ehrenfest: *The conceptual foundations of the statistical approach in mechanics*. Dover Publications Inc., New York, 1990.

[28] O. Filippova, D. Hänel: Grid Refinement for lattice-BGK models, Journal of Computational Physics **147**, 1998, 219–228.

[29] M.W. Frank: *Fluid Mechanics*, Third Edition, McGraw-Hill,Inc., 1994.

[30] J. Franke and W. Frank:Large eddy simulation of the flow past a circular cylinder at ReD=3900, Journal of Wind Engineering and Industrial Aerodynamics **90**, 2002, 1191–1206.

[31] R. Franke, W. Rodi and B. Schonung: Numerical calculation of laminar vortex-shedding flow past cylinders, Journal of Wind Engineering and Industrial Aerodynamics **35**, 1990, 237–257.

[32] U. Frisch, B. Hasslacher, Y. Pomeau: Lattice gas automata for the Navier-Stokes equations, Phys. Rev. Lett. **56(14)**, 1986, 1505–1508.

[33] I. Ginzbourg, P.M. Alder: Boundary flow condition analysis for the three-dimensional lattice Boltzmann model, J. Phys. II France **4**, 1994, 191–214.

[34] A.N. Gorban: Basic types of coarse-graining. In: A.N. Gorban, N. Kazantzis, I.G. Kevrekidis, H.-C. Öttinger, C. Theodoropoulos: (eds.) Model Reduction and Coarse-graining Approaches for Multiscale Phenomena, Springer, Berlin (cond-mat/0602024), 2006, 117–176.

[35] R.P. Hansen and L.N. Long: Large eddy simulation of a circular cylinder on unstructured grid, AIAA-2002-0982, 1998.

[36] J. Hardy, O. d'Pazzis, Y. Pomeau: Molecular dynamics of a classical lattice gas: transport properties and time correlation functions, Phys. Rev. A **13(5)**, 1976, 1949–1961.

[37] X. He, L.S. Luo, M. Dembo: Some progress in lattice Boltzmann method, Part 1. Non-uniform mesh grids, Journal of Computational Physics **129**, 1996, 357–363.

[38] X. He, Q. Zou, L.-S. Luo, M. Dembo: Analytic solutions and analysis on non-slip boundary condition for the lattice Boltzmann BGK model, J. Stat. Phys. **87**, 1997, 115–136.

[39] X. He, G. Doolen: Lattice Boltzmann method on a curvilinear coordinate system:vortex shedding behind a circular cylinder, Phys. Rev. E **56**, 1997, 434–440.

[40] X. He, G. Doolen: Lattice Boltzmann method on a curvilinear coordinate system:flow around a circular cylinder, Journal of Computational Physics **134**, 1997, 306–315.

[41] M.S. Ingber: A vorticity method for determining drag on bluff bodies, International J. of Dynamics of Fluids **2(1)**, 2006, 1–11.

[42] X. He, L.-S. Luo: Theory of the lattice Boltzmann method: From the Boltzmann equation to lattice Boltzmann equation, Phys. Rev. E **56(6)**, 1997, 6811–6817.

[43] R.D. Henderson: Details of the drag curve near the onset of vortex shedding, Phys. Fluids **7**, 1995, 2102–2104.

[44] F.J. Higuera, J. Jiménez: Boltzmann approach to lattice gas simulations, Europhys. Lett. **9(7)**, 1989, 663–668.

[45] F.J. Higuera, S. Succi: Simulating the flow around a circular cylinder with a lattice Boltzmann method, Europhys. Lett. **8(6)**, 1989, 517–521.

[46] F.J. Higuera, S. Succi, R. Benzi: Lattice gas dynamics with enhanced collisions, Europhys. Lett. **9(4)**, 1989, 345–349.

[47] I.V. Karlin, A.N. Gorban, S. Succi, V. Boffi: Maximum entropy principle for lattice kinetic equations, Phys. Rev. Lett. **81(1)**, 1998, 6–9.

[48] I.V. Karlin, A. Ferrante, H.C. Ottinger: Perfect entropy functions of the lattice Boltzmann method, Europhysics Letters **47(2)**, 1999, 182–188.

[49] I.V. Karlin, S. Ansumali, C.E. Frouzakis, S.S. Chikatamarla: Elements of the lattice Boltzmann method I: linear advection equation, Communications in Computational Physics **1,(4)**, 2006, 616–655.

[50] I.V. Karlin, S.S. Chikatamarla, S. Ansumali: Elements of the lattice Boltzmann method II: kinetics and hydrodynamics in one dimension, Communications in Computational Physics **2,(2)**, 2007, 196–238.

[51] P.-H. Kao, R.-J. Yang: An investigation into curved and moving boundary treatments in the lattice Boltzmann method, Journal of Computational Physics **227**, 2008, 5671–5690.

[52] T.S. Khan, J. Levesley: Stabilizing lattice Boltzmann simulation of fluid flow past a circular cylinder with Ehrenfests limiter, Approximation Algorithms for Complex Systems **3(2)**, 2011, 227–239.

[53] J.M.V.A Koelman: A simple lattice Boltzmann scheme for Navier-Stokes fluid flow, Europhys. Lett. **15(6)**, 1991, 603–607.

[54] A.G. Kravchenko and P. Moin: Numerical studies of flow around a circular cylinder at ReD=3900, Physics of Fluids **12**, 2000, 403–417.

[55] P. Lallemand, L.-S. Lue: Theory of the lattice Boltzmann method: dispersion, dissipation, isotropy, Galilean invariance and stability, Physical Review E **61(6)**, 2000, 6546–6562.

[56] Y. Li, R. Shock, R. Zhang, H. Chen: Numerical study of flow past a circular cylinder by the lattice Boltzmann method, J. Fluid Mech. **519**, 2004, 273–300.

[57] Y. Li, R. Zhang, R. Shock, and H. Chen: Prediction of vortex shedding from a circular cylinder using a volumetric Lattice-Boltzmann boundary approach, Eur. Phys. J. Special Topics **171**, 2009, 91–97.

[58] J.H. Lienhard: Synopsis of lift, drag, and vortex frequency for rigid circular cylinder, College of Engg. Research Div. Bulletin 300, Technical. Extension Service, Washington State University, 1966.

[59] D.P. Lockard, L-.S. Luo, B.A. Singer: Evaluation of Powerflow for aerodynamic applications. Preprint, 2000.

[60] L. Lourenco, C. Shih: Characteristics of the plane turbulent near wake of a circular cylinder, a particle image velocimetry study (Data published in Beaudan P. (1998)), 1993.

[61] L.-S. Lou: Analytic solutions of linearized lattice Boltzmann equation for simple flows, J. Stat. Phys. **88**, 1997, 913–926.

[62] H. Lubcke, St. Schmidt, T. Rung, F. Thiele: Comparison of LES and RANS in bluff body flows, Journal of Wind Engineering and Industrial Aerodynamics **89**, 2001, 1471–1485.

[63] X. Ma, G.-S. Karamanos, G.E. Karniadakis: Dynamics and low-dimensionality of a turbulent near wake, J. Fluid Mech. **410**, 2000, 29–65.

[64] M.E. McCracken, J. Abraham: Multiple-relaxation-time lattice-Boltzmann model for multiphase flow, Physical Review E **71**, (036701), 2005.

[65] G. McNamara, G. Zanetti: Use of the lattice Boltzmann equation to simulate lattice-gas automata, Phys. Rev. Lett. **61(20)**, 1988, 2332–2335.

[66] R. Mei, L.S. Luo, W. Shyy: An accurate curved boundary treatment in the lattice Boltzmann method, Journal of Computational Physics **155**, 1999, 307–330.

[67] R. Mei, W. Shyy, D. You, L.S. Luo: Lattice Boltzmann method for 3-D flows with curved boundary, Journal of Computational Physics **161**, 2000, 680–699.

[68] R. Mei, D. Yu, W. Shyy: Force evaluation in the lattice Boltzmann method involving curved geometries, Phys. Rev. E. **65**, 2002, 041203.

[69] R. Mittal, P. Moin: Suitibility of upwind-biased finite-difference schemes for large-eddy simulation of turbulent flow, AIAA J. **35(8)**, 1997, 1415–1417.

[70] R. Mittal, S. Balachandar: Direct numerical simulation of flow past elliptic cylinders, J. Comput. Phys. **124**, 1996, 351–367.

[71] C. Norberg: Effects of Reynolds number and a low-intensity free-stream turbulence intensity on the flow around a circular cylinder, Publication No. 87/2

Dept. Applied Thermodynamics and Fluid Mechanics, Chalmers University of Technology, 1987.

[72] C. Norberg: An experimental investigation of the flow around a circular cylinder: influence of aspect ratio, Journal of Fluid Mech. **258**, 1994, 287–316.

[73] L. Ong, J. Wallace: The velocity field of the turbulent very near wake of a circular cylinder: Experiments in Fluids **20**, 1996, 441–453.

[74] D.J. Packwood, J. Levesley, A.N. Gorban: Time Step Expansions and the Invariant Manifold Approach to Lattice Boltzmann Models, Lecture Notes in Computational Science and Engineering **75**, 2011, 169–205.

[75] O. Posdziech, R. Grundmann: Numerical simulation of the flow around an infinitely long circular cylinder in the transition regime, Theoretical and Computational Fluid Dynamics **15**, 2001, 121–141.

[76] Y.H. Qian, D. d'Humières, P. Lallemand: Lattice BGK models for Navier-Stokes, Europhys. Lett. **17(6)**, 1992, 479–484.

[77] A. Roshko: On the developement of turbulent wakes from vortex streets. Rep. 1191, NACA, 1954.

[78] B.N. Rajani, H.G. Lanka, S. Majumdar: Laminar flow past a circular cylinder at Reynolds number varying from 50 to 5000, NAL PD CF 0501, 2005.

[79] B.N. Rajani, A. Kandasamy, S. Majumdar: Numerical simulation of laminar flow past a circular cylinder, Applied Mathematical Modelling **33**, 2009, 1228–1247.

[80] W. Sitch: Effective shapes and turbulent wake, http://fur-o-dynamic.org/theory/.

[81] J.D. Sterling, S. Chen: Stability analysis of the lattice Boltzmann methods, Journal of Computational Physics **123**, 1996, 196–206.

[82] S. Succi, R. Benzi, F.J. Higuera: The lattice Boltzmann equation: a new tool for computational fluid dynamics, Physica D **47**, 1991, 219–230.

[83] S. Succi: *The Lattice Boltzmann Equation for Fluid Dynamics and Beyond.* Oxford University Press, New York, 2001.

[84] S. Succi, I.V. Karlin, H. Chen: Colluquium: Role of the H theorem in lattice Boltzmann hydrodynamic simulations, Reviews of Modern Physics **74**, 2002, 1203–1220.

[85] C.S. Sunder, V. Babu: Entropic lattice Boltzmann method, Non-uniform grids, ICCS, LNCS 3516, 2005, 72–79.

[86] F. Tosi, S. Ubertini, S. Succi, H. Chen, I.V. Karlin: Numerical stability of entropic versus positivity-enforcing lattice Boltzmann schemes, Mathematics and Computers in Simulation **72**, 2006, 227–231.

[87] F. Tremblay, M. Manhart, R. Friedrich: LES of flow around a circular cylinder at a subcritical Reynolds number with cartesian grids, Fluid Mechanics and Its Applications **65,(3)**, 2004, 133–150.

[88] D. Tritton: Experiments on the flow past a circular cylinder at low Reynolds numbers, Journal of Fluid Mechanics **6**, 1959, 547–567.

[89] C.-Y. Wen, C.-Y. Lin: Two-dimensional vortex shedding of a circular cylinder, Phys. Fluids **13,(3)**, 2001, 557–560.

[90] C.-Y. Wen, C.-L. Yeh, M.J. Wang, C.-Y. Lin: Two-dimensional vortex shedding of a circular cylinder, Phys. Fluids **16,(10)**, 2004, 3828–3831.

[91] C.H.K. Williamson: Vortex dynamics in the cylinder wake, Annual Rev. Fluid Mech. **28**, 1996, 477–539.

[92] D.A. Wolf-Gladrow: *Lattice-Gas Cellular Automata and Lattice Boltzmann Models: An Introduction*, Lecture notes in mathematics **1725**, Springer-Verlag, Berlin Heidelberg, 2000.

[93] R.A. Worthing, J. Mozer, G. Seeley: Stability of lattice Boltzmann methods in hydrodynamics regimes, Physical Review E **56(2)**, 1997, 2243–2253.

[94] D. You, R. Mei, W. Shyy: A multi-block lattice Boltzmann method for viscous fluid flows, Int. J. Numer. Meth. Fluids **39**, 2002,

[95] D. You, R. Mei, L.S. Luo, W. Shyy: Viscous flow computations with the method of lattice Boltzmann equation, Progress in Aerospace Science **39**, 2003, 329–367. 99–120.

[96] D. You, R. Mei, W. Shyy: A unified boundary treatment in lattice Boltzmann method, AIAA 2003-0953, New York, 2003.

[97] M.M. Zdravkovich: *Flow Around Circular Cylinders (Volume I: Fundamentals)*. Oxford University Press, New York, 1997.

[98] D.P. Ziegler: Boundary conditions for lattice Boltzmann simulations, J. Stat. Phys. **71**, 1993, 1171–1177.